Выделение вулканических и интрузивных тел по сейсмическим данным

А.М. Никишин

Карта вулканов мира за последние 10 000 лет.

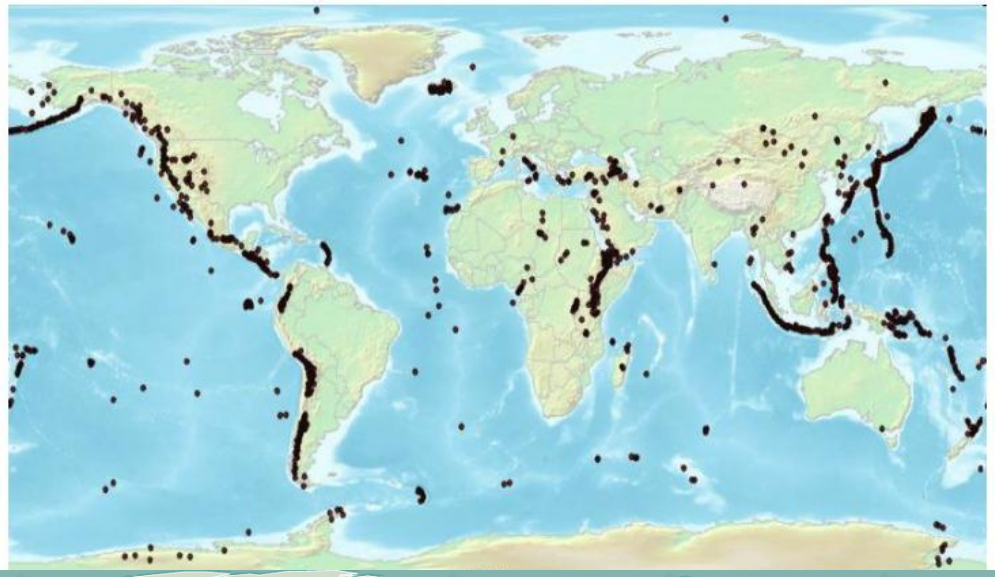

Фото некоторых вулканов
(из интернета)

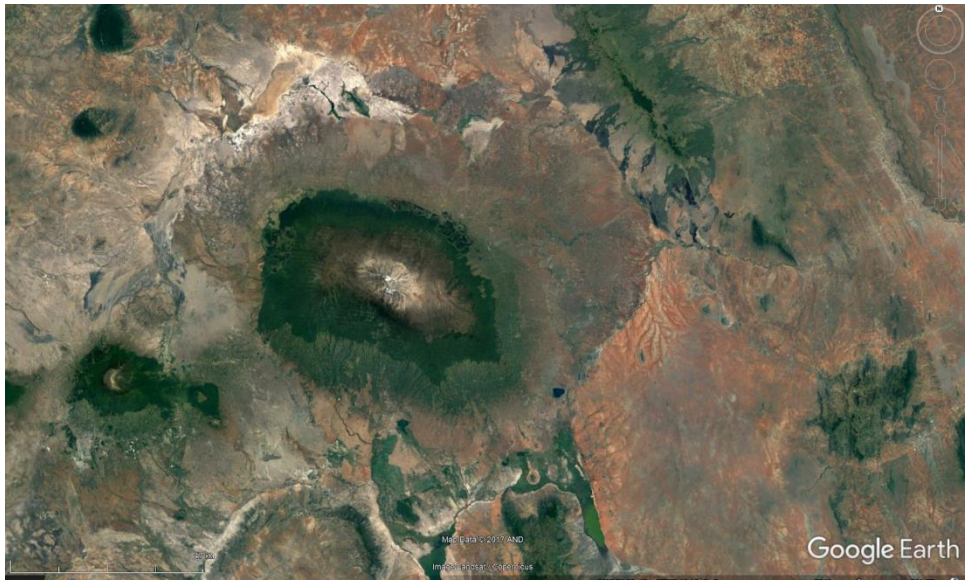

Килиманджаро

Арарат

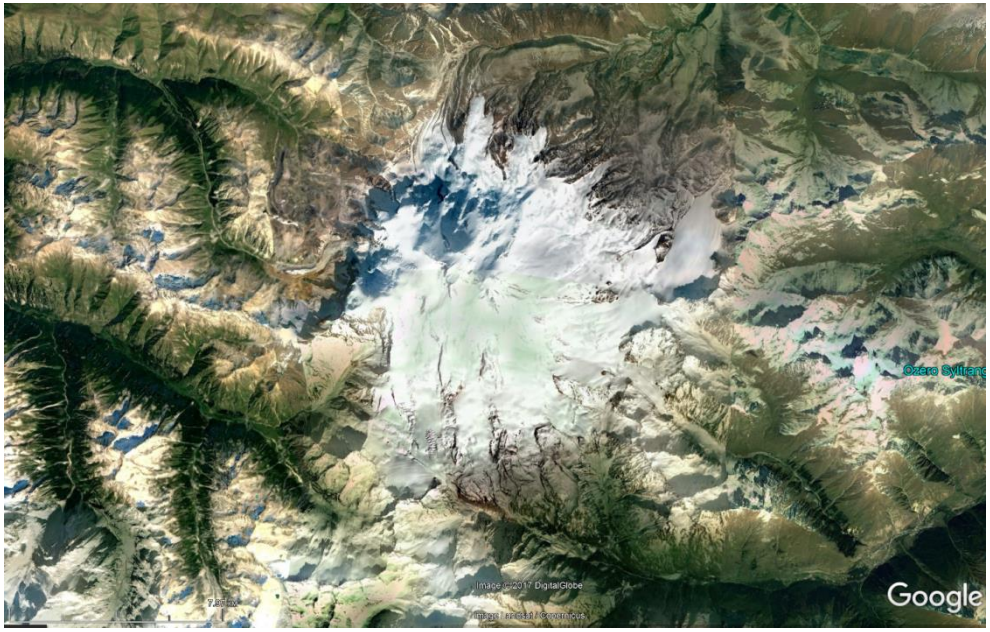

Эльбрус

Везувий

Известные вулканы

Основные типы вулканических пород

Лава – расплав горной породы, излившийся на поверхность

Магма – расплав горной породы

Вулканический шлак – сильно пенистые лавы и их фрагменты перемещенные по воздуху

Вулканические бомбы, лапилли (жидкие капли), вулканический песок (грубый пепел), вулканическая пыль (пепел) (*то что летело по воздуху*) –
после литификации становятся туфами.

Вулканокластические породы – продукты размыва вулканических сооружений (например, туфопесчаники, туфоалевролиты и др.)

Вулкан Вулькано в Тирренском море (слово вулкан от названия этого острова)

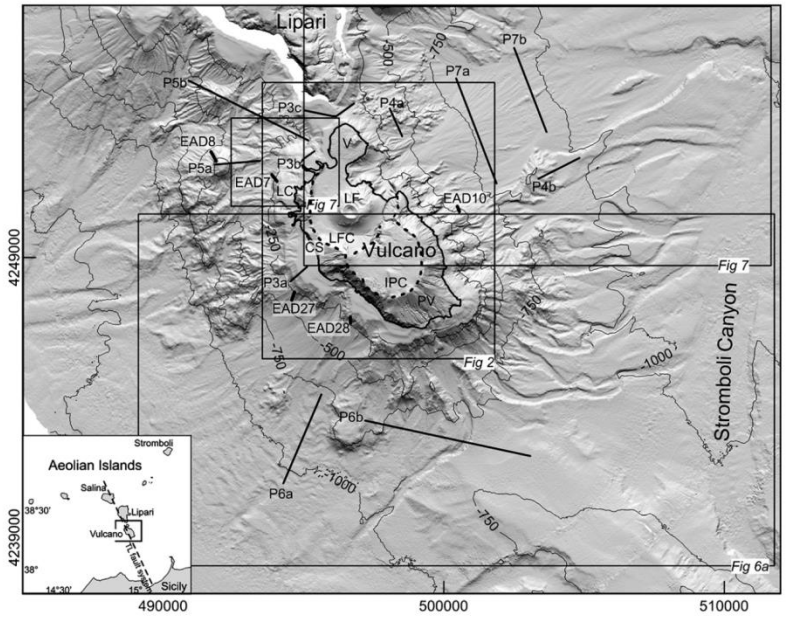

Fig 1. Shaded relief image of Vulcano volcano (grid size of 20 m), with the location of seismic profiles (P) and dredges (EAD, see also Table 1); the dashed lines on the island represent the limits of Il Piano and La Fossa calderas (IPC and LFC, respectively). V: Vulcanello; LC: Lentia Complex; LF: La Fossa Cone; CS: Capo Secco; PV: Primordial Vulcano. In the lower inset, location of the study area (black box) and of the presumed submarine prosecution of Tindari–Letojanni (TL) fault system (dashed line).

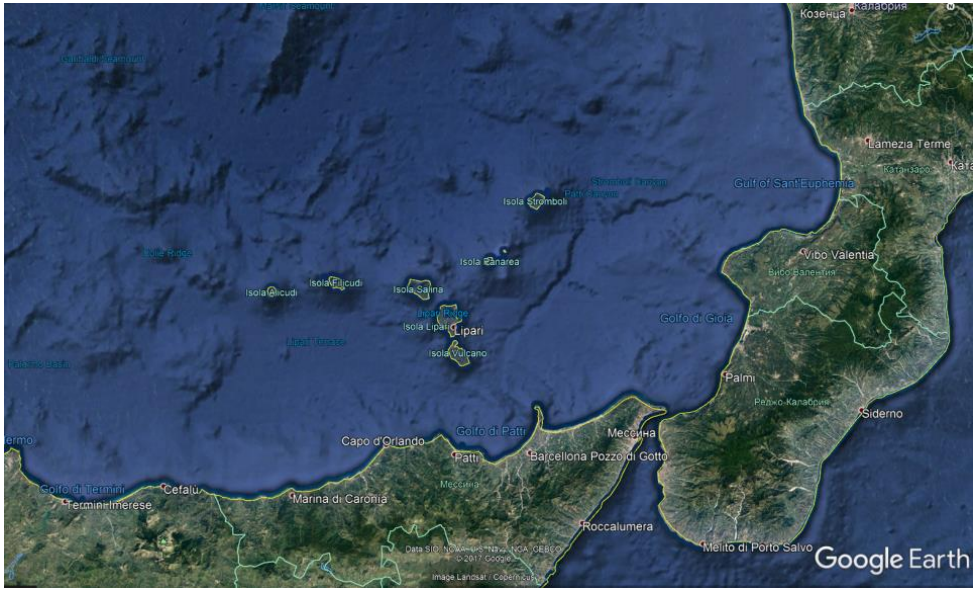

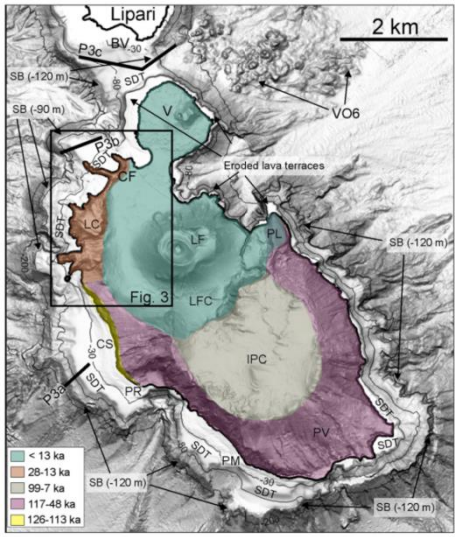

Fig. 2. Shaded relief image of Vulcano Island and surrounding shallow-water sectors; the color areas indicate simplified volcanic units outcropping in the island, according to De Astis et al. (2006a). SB is the bedrock slope break of insular shelves with indication of average depth (see text for detail). SDT: Submerged Depositional Terrace. BV: Bocche di Vulcano; V: Vulcanello; CF: Cala del Formaggio, LC: Lentia Complex; LF: La Fossa Cone; PL: Punta Luccia, LFC: La Fossa caldera; IPC: Il Piano caldera; PR: Punta del Rosario, PM: Punta del Mortaro, PV: Primordial Vulcano; VO: Volcanic outcrop.

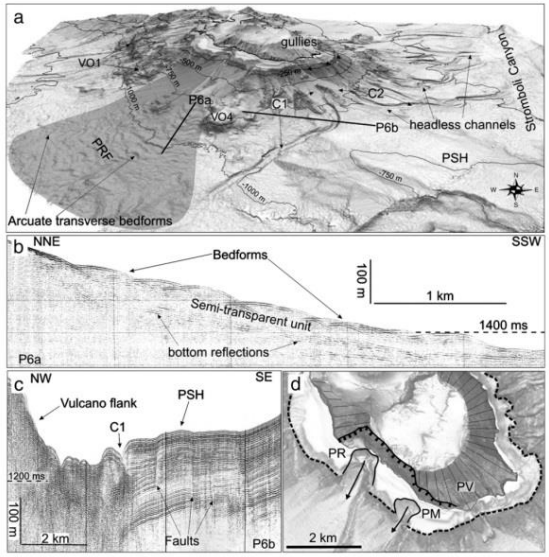

Fig. 6. Shaded relief image of the southern part of Vulcano edifice (a), with the indication of Punta del Rosario fan (PRF, dark-grey area); acronyms as in Figs. 1 and 2. Below (b and c): two Sparker 4.5 kJ profiles (location in Fig. 6a), showing: a semitransparent seismo-acoustic unit with widespread superficial bedforms in correspondence of the PR fan (P6a) and the sharp contact between the volcanic terrains of Vulcano southern flank and the sedimentary units of the Patti Sedimentary High (PSH in P6b), along which the headless channel C1 is cut. In Fig. 6d the dotted line represents the edge of insular shelves at ≈120 mbsl; the scars of Punta del Rosario (PR) and Punta del Mortaro (PM) are also indicated, as well as a wide subaerial erosive scarp in the southwestern flank of Primordial Vulcano.

Гавайская цепь вулканов

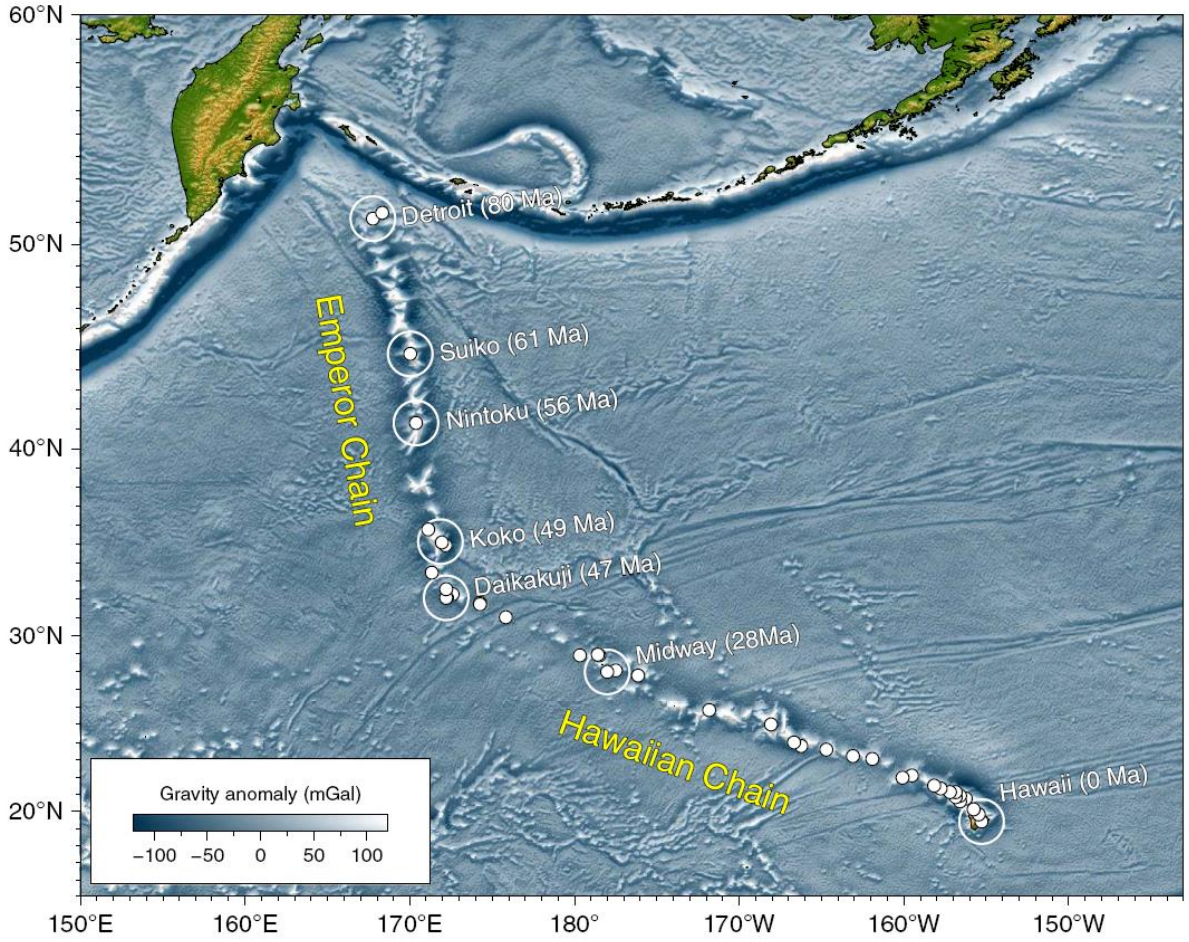

Figure 1 | Hawaiian-Emperor Chain. White dots are the locations of radiometrically dated seamounts, atolls and islands, based on compilations of Doubrovine *et al.*[28] and O'Connor *et al.*[40]. Features encircled with larger white circles are discussed in the text and Fig. 2. Marine gravity anomaly map is from Sandwell and Smith[48].

Вулкан Санторин

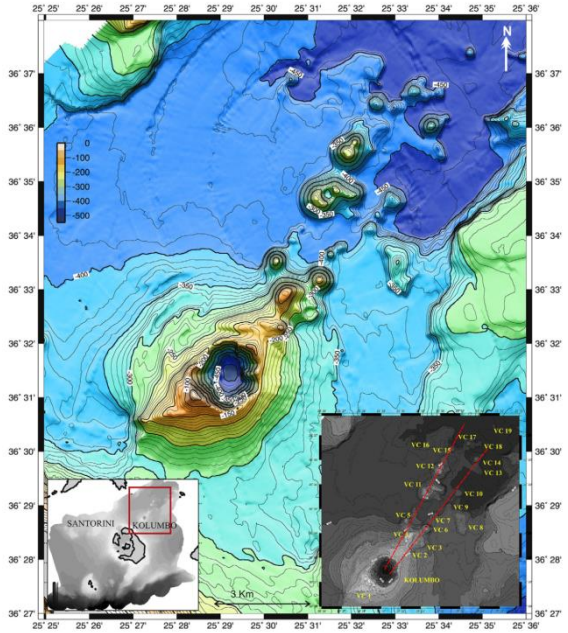

Fig. 6. A. Swath bathymetric map of the submarine Kolumbo volcanic chain using 10 m isobaths. Right inset: Bathymetric map reciting the 19 volcanic domes in two NE–SW trending lines. Left inset: Geographical index map.B. Histogram showing the distribution of the height of volcanic cones along the volcanic chain from Kolumbo to the eastern most volcanic cone No 19.

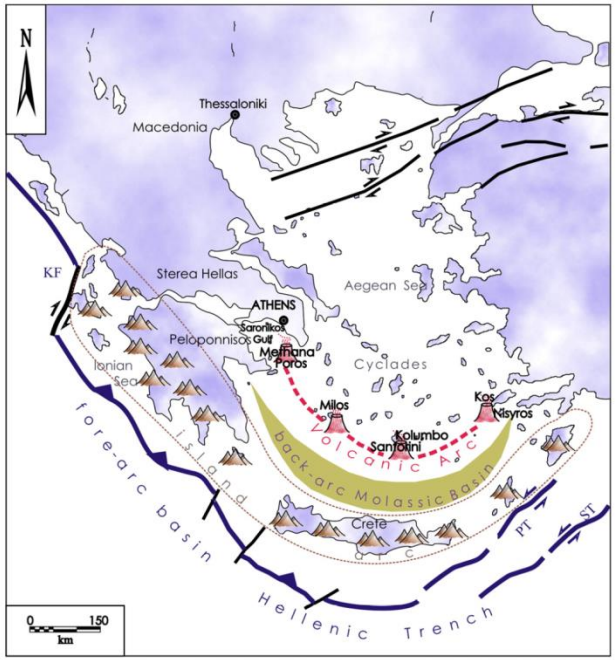

Fig. 1. Location of Santorini within the Hellenic volcanic arc.

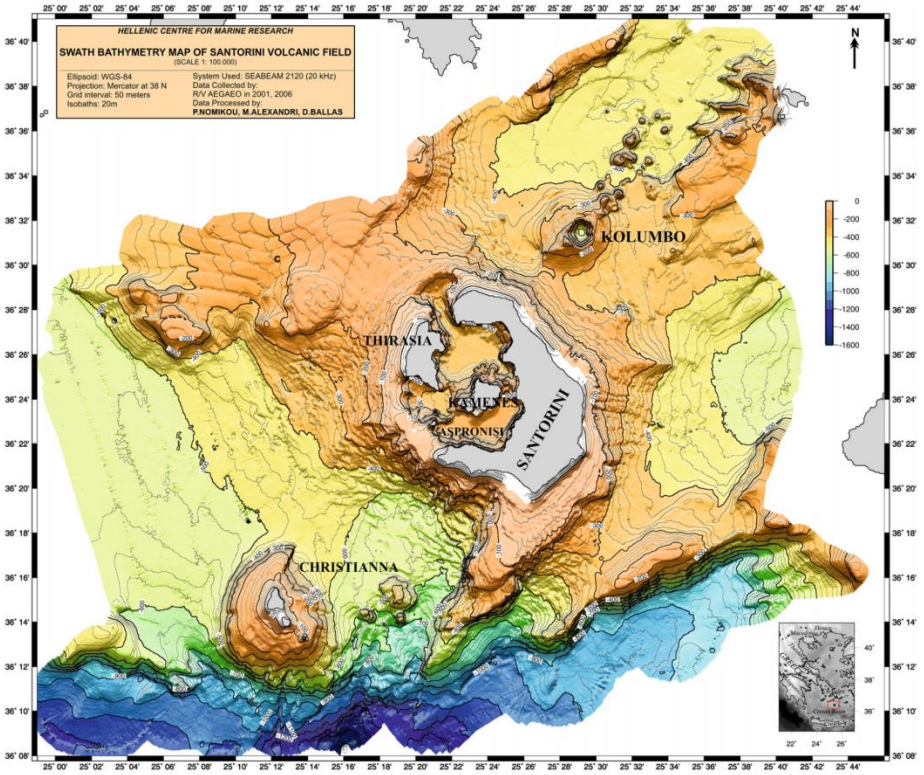

Типы вулканов по строению

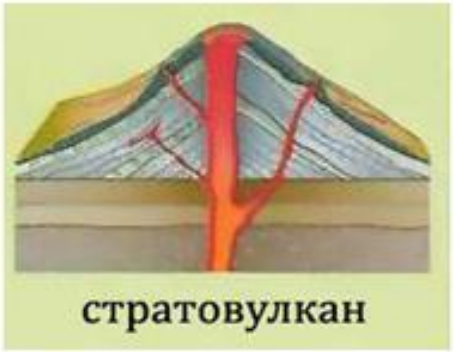

кальдера

шлаковый конус

сложный вулкан

жерловая трещина

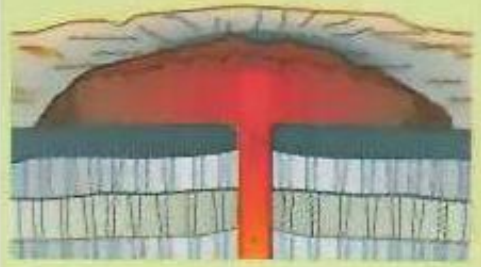

лавовый купол

щитовой вулкан

сомма

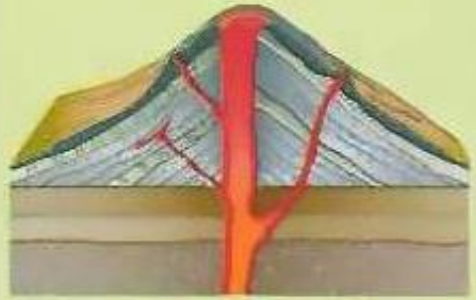

стратовулкан

туфовый конус

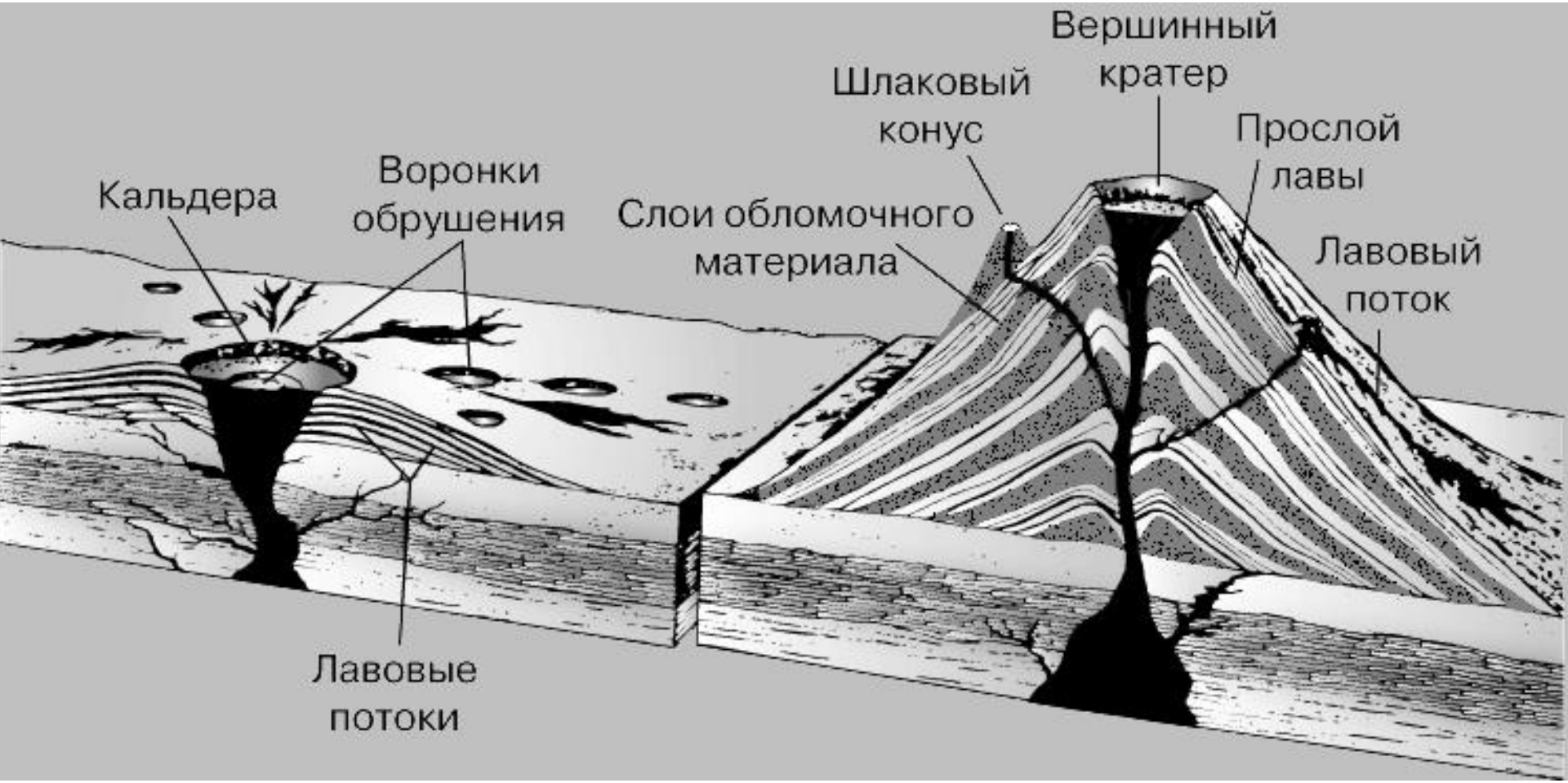

ЩИТОВОЙ ВУЛКАН (слева) с большим кратером (кальдерой), и тонким покровом застывшей лавы на поверхности. Излияния лавы могут происходить из кратера на вершине или через трещины на склонах. Внутри кальдеры, а также на склонах щитового вулкана встречаются воронки обрушения. КОНУС СТРАТОВУЛКАНА (справа) состоит из чередующихся слоев лавы, пепла, шлаков и более крупных обломков. На склоне вулкана показан шлаковый конус.

Типы вулканов

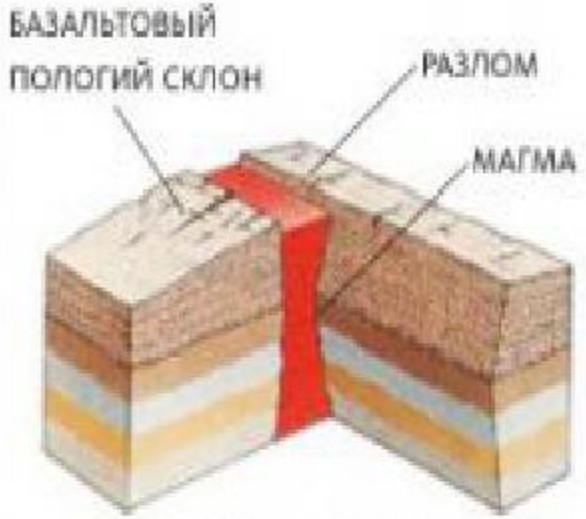

Линейный вулкан

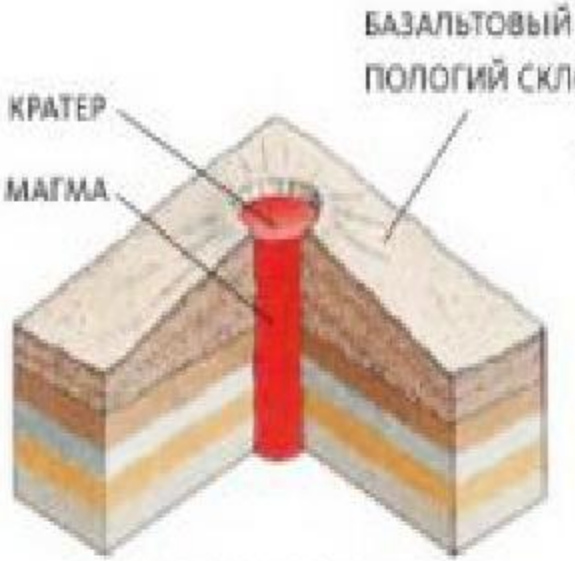

Щитовидный вулкан

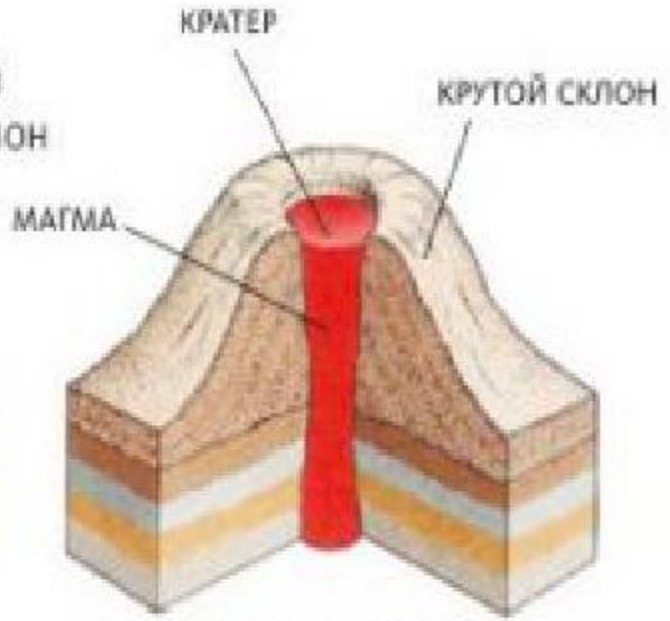

Купольный вулкан

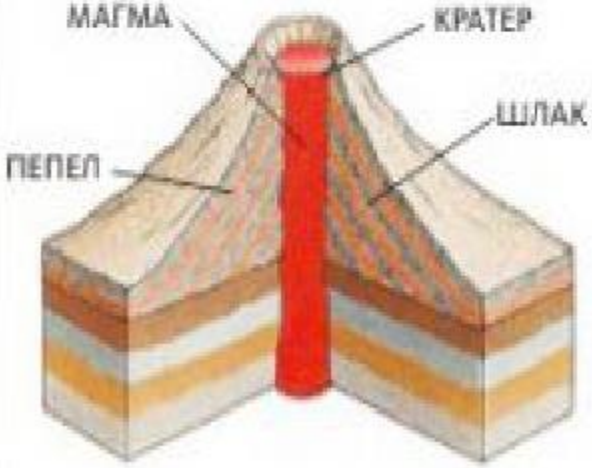

Шлаковый конус

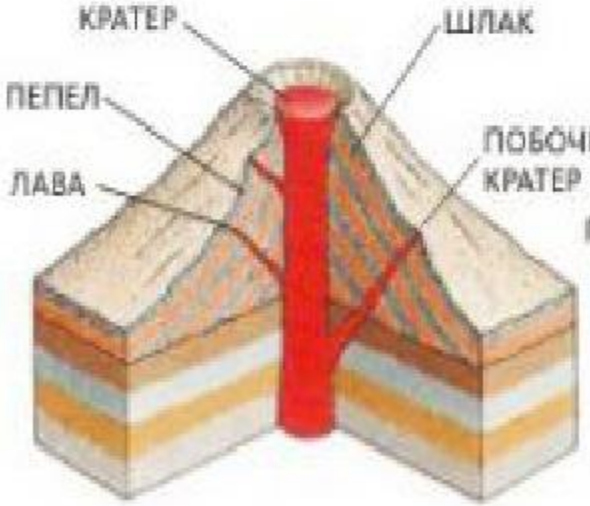

Стратовулкан

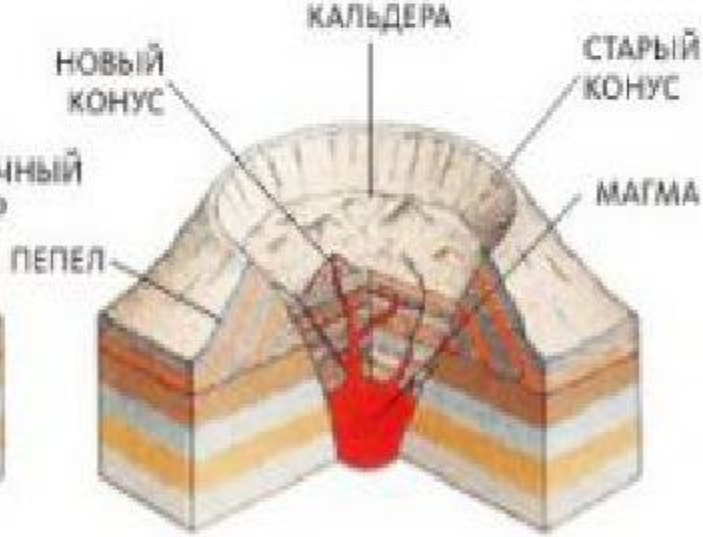

Кальдера

TYPES OF VOLCANO

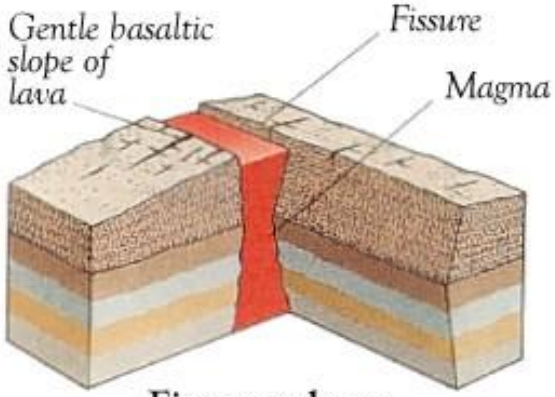

Fissure volcano

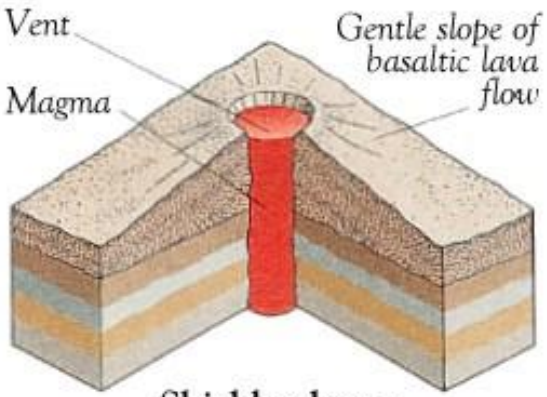

Shield volcano

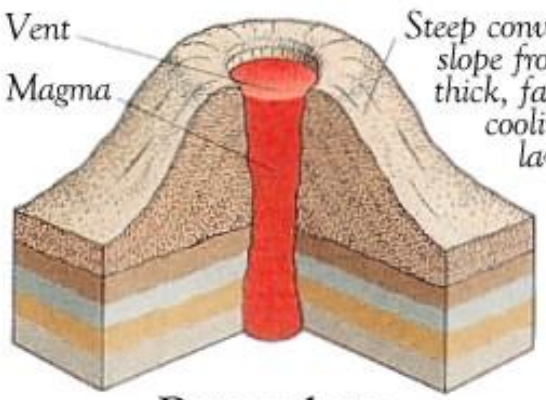

Dome volcano

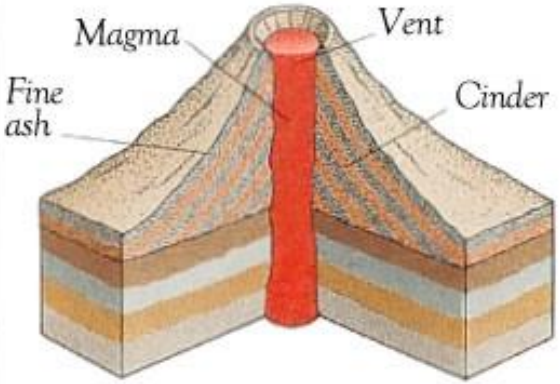

Ash-cinder volcano

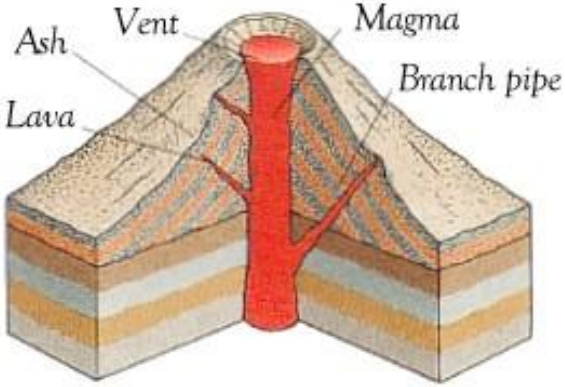

Composite volcano

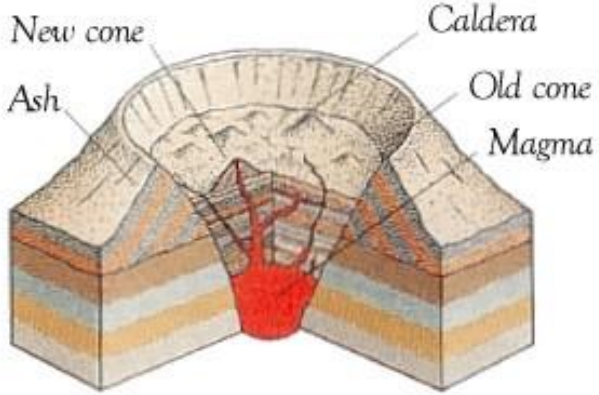

Caldera volcano

VOLCANIC FEATURES

Fissure vent

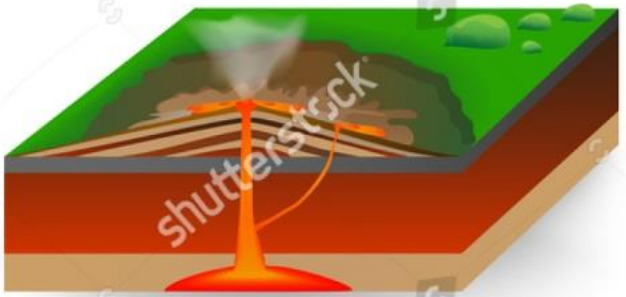

Shield volcano

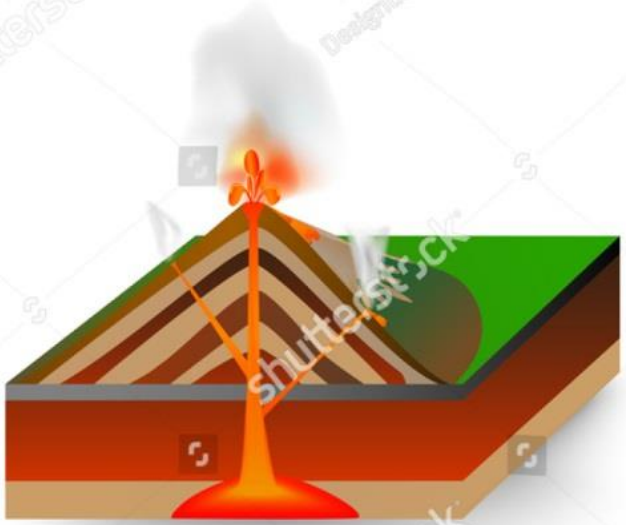

Stratovolcano

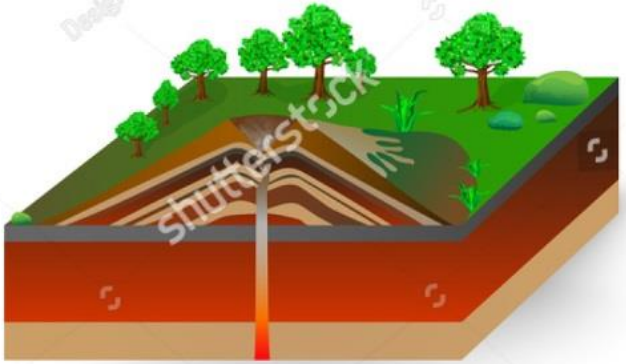

Lava dome

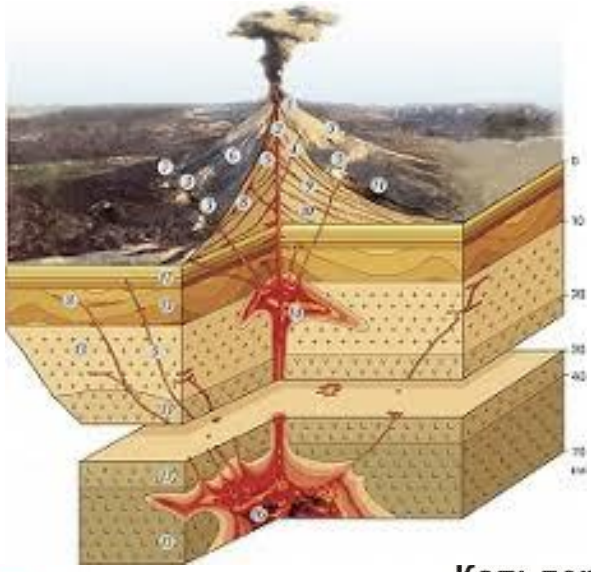

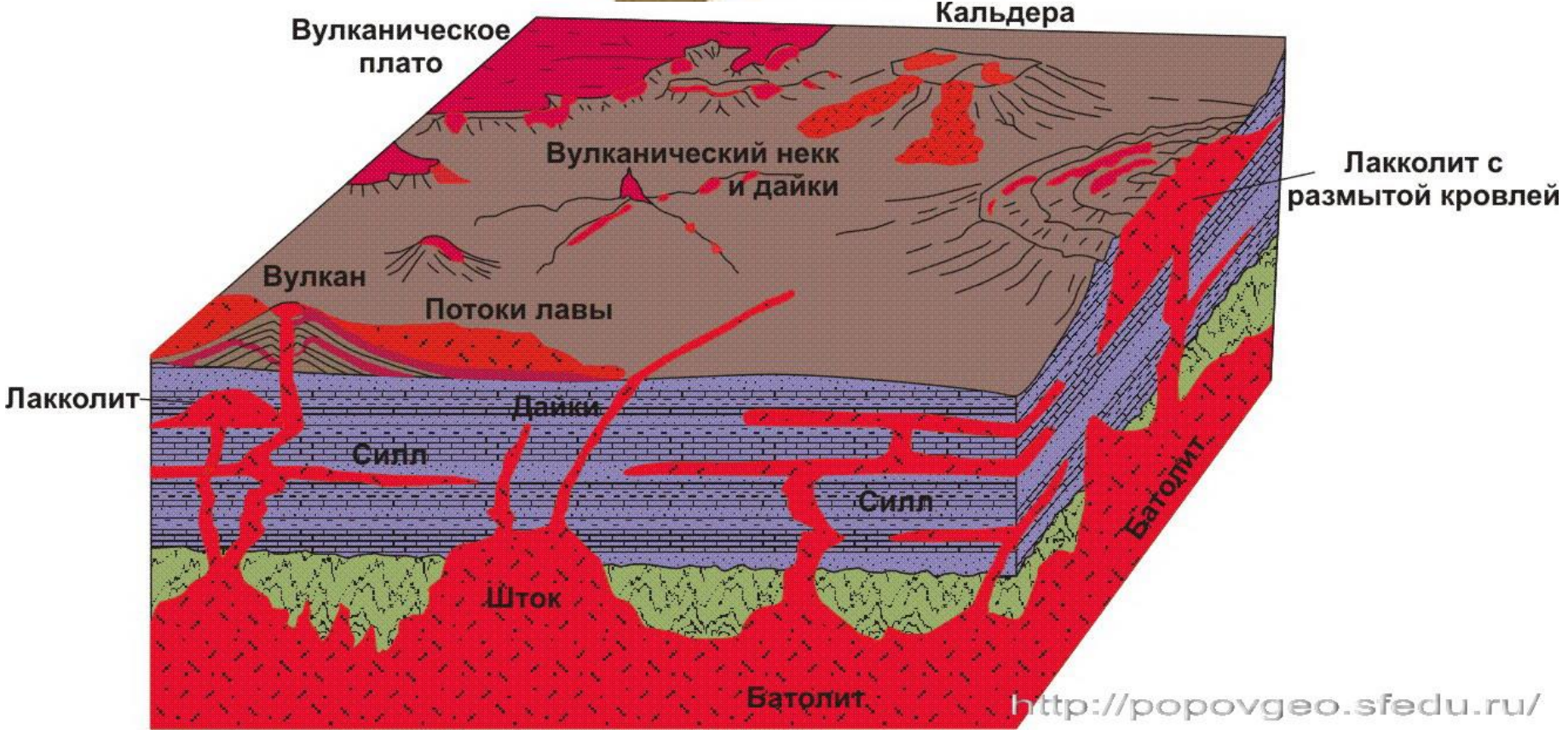

Вулканические континентальные окраины

Вид Seaward Dipping Reflectors (SDR) на сейсмических профилях.

Рефлекторы «образованы» потоками базальтов

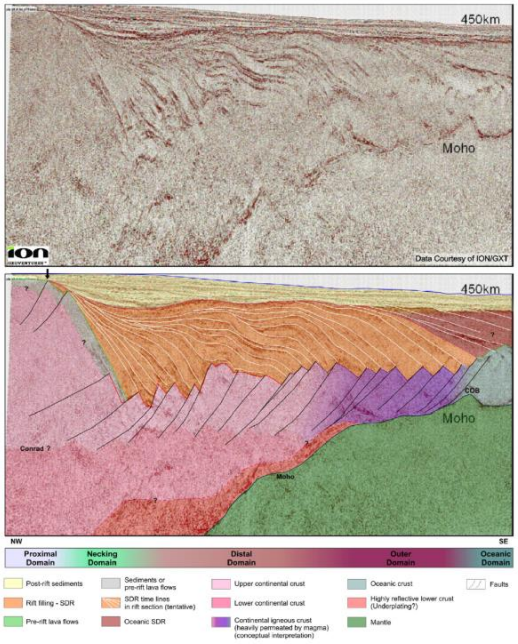

Figure 7. Regional seismic section take from ION-GXT website (http://www.iongeo.com/content/documents/Resource%20Center/Brochures%20and%20Data%20Sheets/Data%20Sheets/Data%20Library/DS_GEO_PelotasSPAN.pdf). Non-interpreted and interpreted versions. The focus is on seaward-dipping reflectors (SDR) and the main structural features related to the rift section. Solid white lines show time lines of deposition, details of interpretation in chapter 3. This section was already used in Blaich et al. (2013) and Zalán (2013), both with different interpretations.

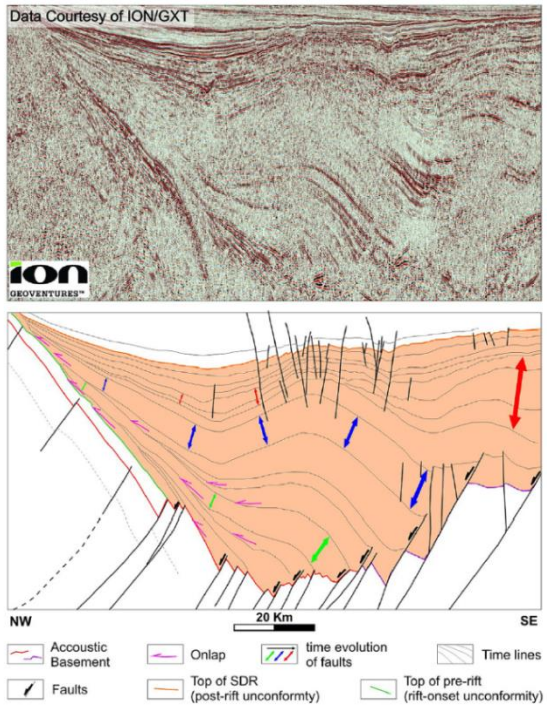

Figure 9. Detailed view of the rift section. Colored double arrows show three examples of strata growth against the rift faults and the propagation of the rift faults to the East, towards the future site of the breakup (footwall collapse propagation). Internal unconformities and onlap terminations indicate one criteria to estimate the chronological evolution of deposition and faulting. Seismic data courtesy of ION-GXT.

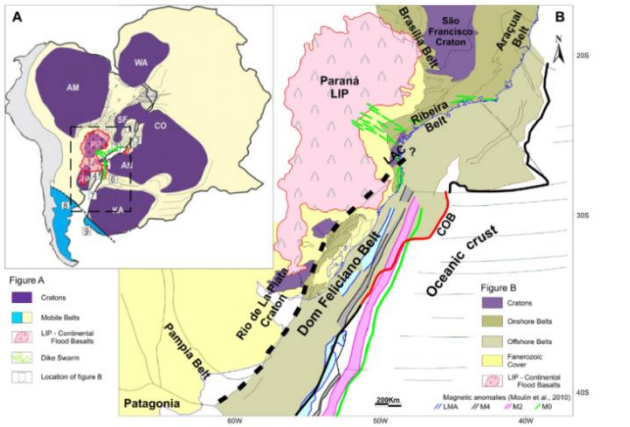

Figure 2. (A) Regional map of Western Gondwana adapted from Heilbron et al. (2008) and Almeida et al. (2013), showing the regional distribution of lavas flows from Paraná–Etendeka LIP and the related dike swarms (green) in relation to a possible structural heritage of the cratons (purple) and mobile belts (yellow). Mobile belts: 1, Araçuaí; 2 Ribeira; 3, West Congo; 4, Dom Feliciano; 5, Kaoko; 6, Damara; 7, Gariep; 8, Sierra de la Ventana; 9, Cape Fold Belt. Major cratons: AM, Amazônia; SF, São Francisco; LA, Luis Alves; RP, Rio de la Plata; WA, West Africa; CO, Congo; PP, Paranapanema; AN, Angola; KA, Kalahari. (B) Detail of the regional geology of the studied area, from Argentine to the southeastern margin of Brazil. The black dashed line shows the contact of the Rio de la Plata Craton with the Dom Feliciano Belt which is probably the basement of the Pelotas Basin. The question mark relates to the uncertainty about the contact between the Dom Feliciano and Ribeira Belts and the Luis Alves Craton (LAC) extending into the Santos Basin. NE-SW trending structural framework of Dom Feliciano Belt is parallel to the trends of the rift faults. COB, Continental Ocean Boundary. The structural framework of Argentina and the COB (black line) are from Fàngaro and Ramos (2012). The structural framework from Uruguay until LAC are from Basei et al. (2010); and the lineaments and contacts from southeastern margin are from Heilbron et al. (2008). The red COB is from this study and the black COB for the southeastern margin is from Zalán et al. (2011). Magnetic anomalies from Moulin et al. (2010). (For interpretation of the references to colour in this figure legend, the reader is referred to the web version of this article.)

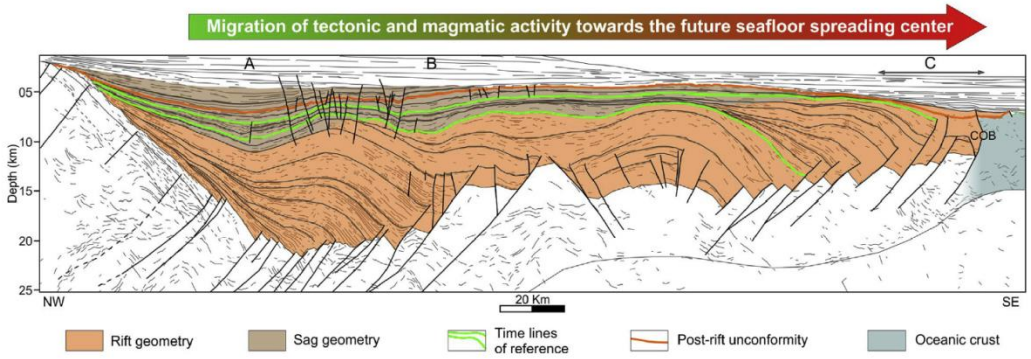

Figure 10. Detailed view of line drawing in Figure 6 showing the relationship in time between sag and rift geometries. Two levels were marked internally in green solid lines, in order to demonstrate the contemporaneity between proximal sag geometry and distal rift. Solid red line is the top of the rift section and of the SDR (post-rift unconformity). Orange mask represents deposition in rift environment and the brown mask represents deposition in a sag geometry, even in distal rift tectonic environment. Notice that the sag geometry in depocenters A and B pervades the top of the rift boundary (solid red line) into the drift sequence. Because of these, the post-rift unconformity is equivalent to the breakup unconformity only in the extreme distal portion of the rift (region C), close to the COB, where no sag geometry is developed. (For interpretation of the references to colour in this figure legend, the reader is referred to the web version of this article.)

Вид Seaward Dipping Reflectors (SDR) на сейсмических профилях.

Рефлекторы «образованы» потоками базальтов

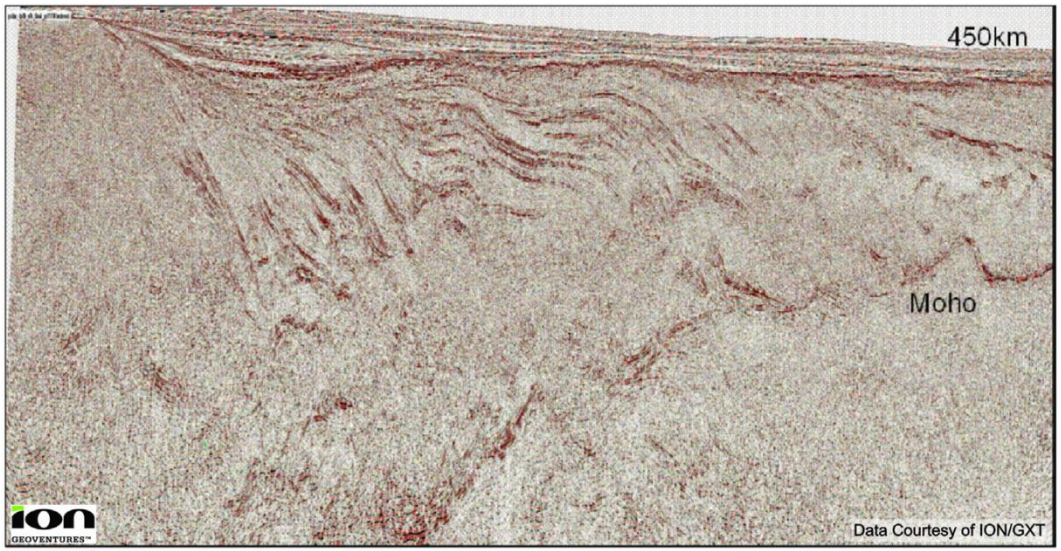

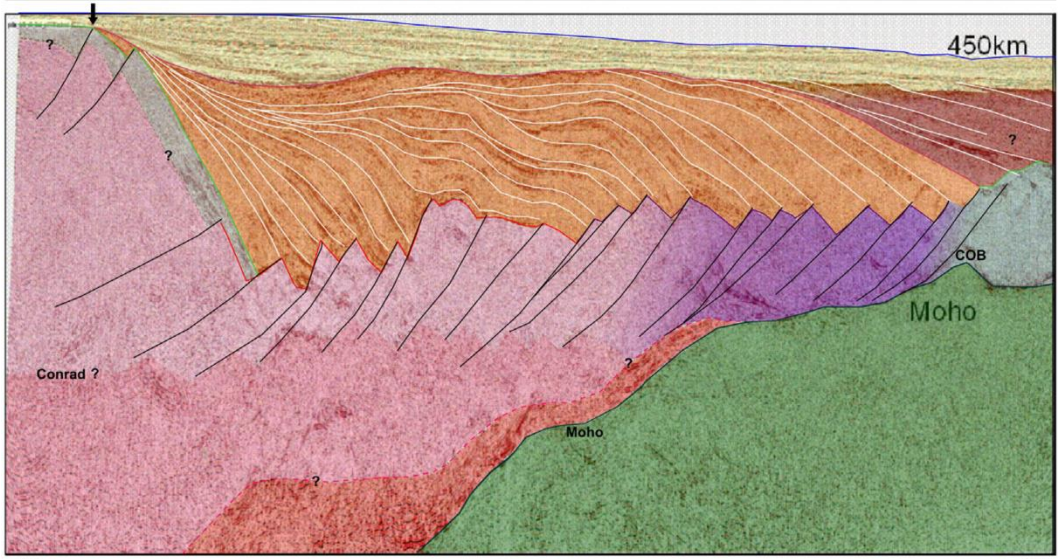

NW SE

Proximal Domain | Necking Domain | Distal Domain | Outer Domain | Oceanic Domain

- Post-rift sediments
- Rift filling - SDR
- Pre-rift lava flows
- Sediments or pre-rift lava flows
- SDR time lines in rift section (tentative)
- Oceanic SDR
- Upper continental crust
- Lower continental crust
- Continental igneous crust (heavily permeated by magma) (conceptual interpretation)
- Oceanic crust
- Highly reflective lower crust (Underplating?)
- Mantle
- Faults

Вид Seaward Dipping Reflectors (SDR) на сейсмических профилях.

Рефлекторы «образованы» потоками базальтов

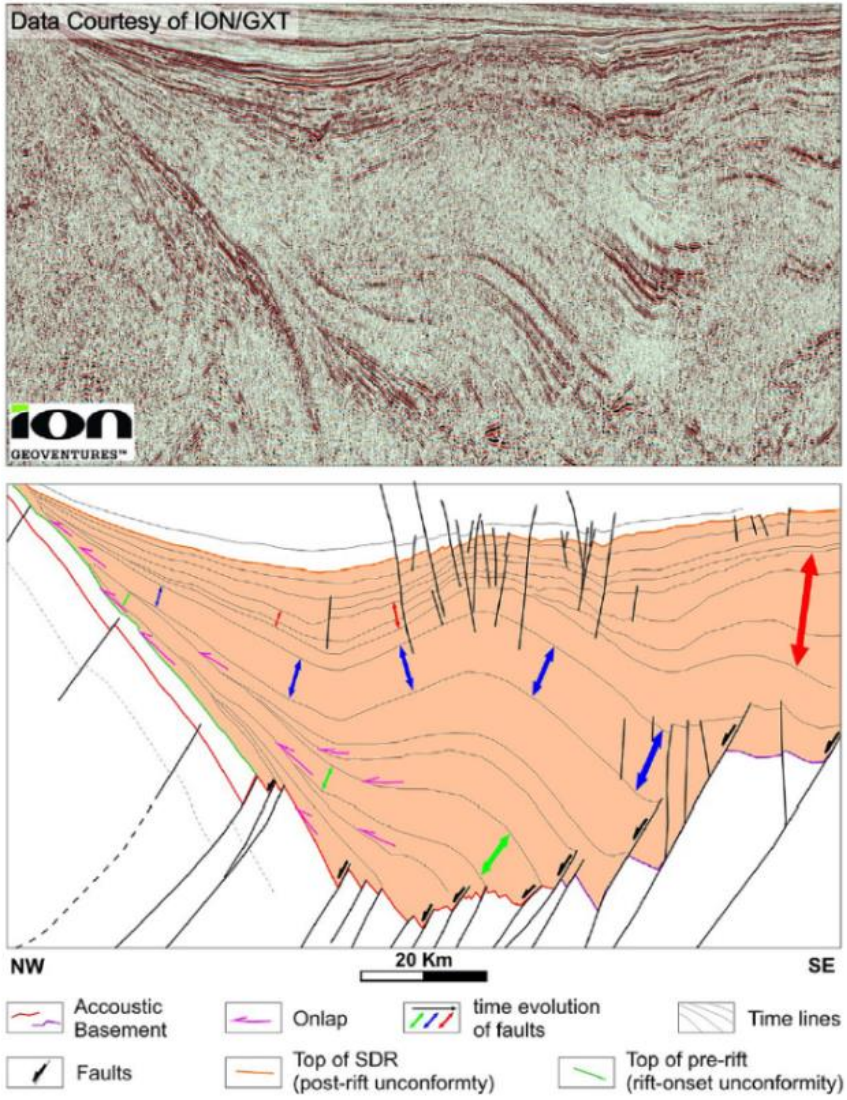

Figure 9. Detailed view of the rift section. Colored double arrows show three examples of strata growth against the rift faults and the propagation of the rift faults to the East, towards the future site of the breakup (footwall collapse propagation). Internal unconformities and onlap terminations indicate one criteria to estimate the chronological evolution of deposition and faulting. Seismic data courtesy of ION-GXT.

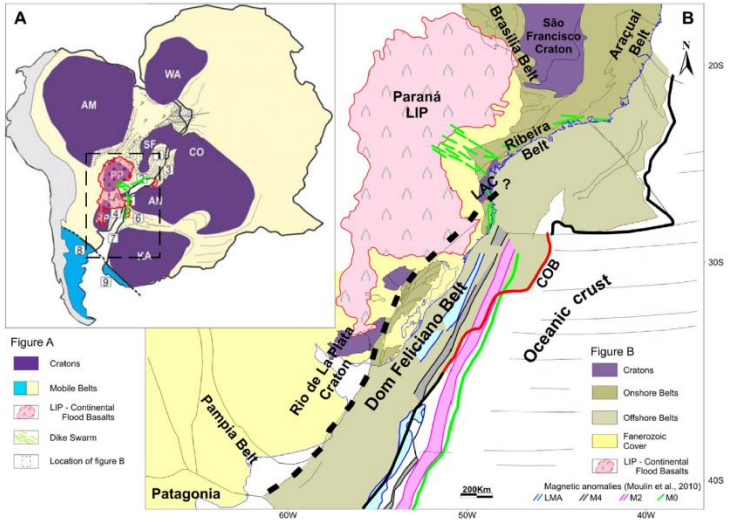

Figure 2. (A) Regional map of Western Gondwana adapted from Heilbron et al. (2008) and Almeida et al. (2013), showing the regional distribution of lavas flows from Paraná–Etendeka LIP and the related dike swarms (green) in relation to a possible structural heritage of the cratons (purple) and mobile belts (yellow). Mobile belts: 1, Araçuaí; 2 Ribeira; 3, West Congo; 4, Dom Feliciano; 5, Kaoko; 6, Damara; 7, Gariep; 8, Sierra de la Ventana; 9, Cape Fold Belt. Major cratons: AM, Amazônia; SF, São Francisco; LA, Luis Alves; RP, Rio de la Plata; WA, West Africa; CO, Congo; PP, Paranapanema; AN, Angola; KA, Kalahari. (B) Detail of the regional geology of the studied area, from Argentine to the southeastern margin of Brazil. The black dashed line shows the contact of the Rio de la Plata Craton with the Dom Feliciano Belt which is probably the basement of the Pelotas Basin. The question mark relates to the uncertainty about the contact between the Dom Feliciano and Ribeira Belts and the Luis Alves Craton (LAC) extending into the Santos Basin. NE-SW trending structural framework of Dom Feliciano Belt is parallel to the trends of the rift faults. COB, Continental Ocean Boundary. The structural framework of Argentina and the COB (black line) are from Pángaro and Ramos (2012); The structural framework from Uruguay until LAC are from Basei et al. (2010); and the lineaments and contacts from southeastern margin are from Heilbron et al. (2008). The red COB is from this study and the black COB for the southeastern margin is from Zalán et al. (2011). Magnetic anomalies from Moulin et al. (2010). (For interpretation of the references to colour in this figure legend, the reader is referred to the web version of this article.)

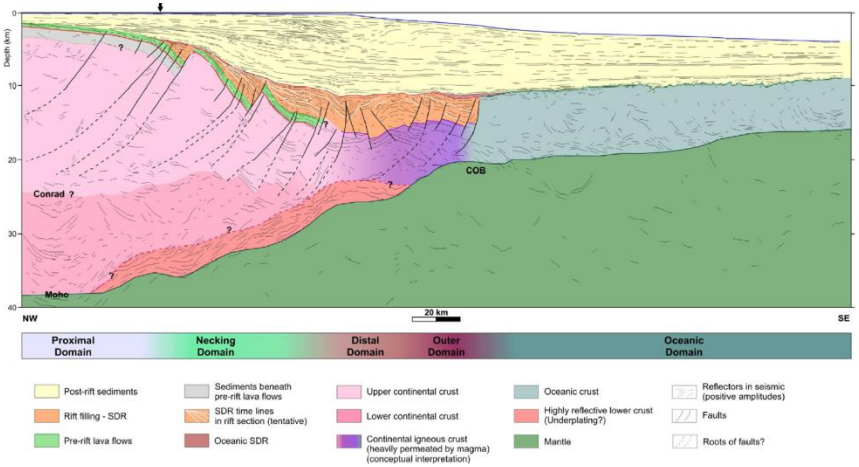

Figure 5. Regional geoseismic dip section of South Pelotas Basin. Line drawing in depth (Line 30 from ION-GXT Pelotas SPAN). The focus is on the seaward-dipping reflectors (SDR) and the main structural features related to the rift section. Solid white lines show time lines of deposition, details of interpretation in chapter 3. Black arrow shows the hingeline. Crustal domains related to deep crustal interpretation and map view of these domains on Figure 8. Solid orange lines on magnetic profile show the position of magnetic anomalies (G, M3, M0) from Rabinowitz and Labrecque (1979); other anomalies (LMA, M4, M2, M0) are from Moulin et al. (2010). These anomalies are in the original position in order to correlate with the magnetic profile and the interpretation of the rift structure and of COB. Western limit of LMA in dashed line refers to original work from Moulin et al. (2010) with no western border of the anomaly in this position. Magnetic profile data from Petrobras regional data bank. (For interpretation of the references to colour in this figure legend, the reader is referred to the web version of this article.)

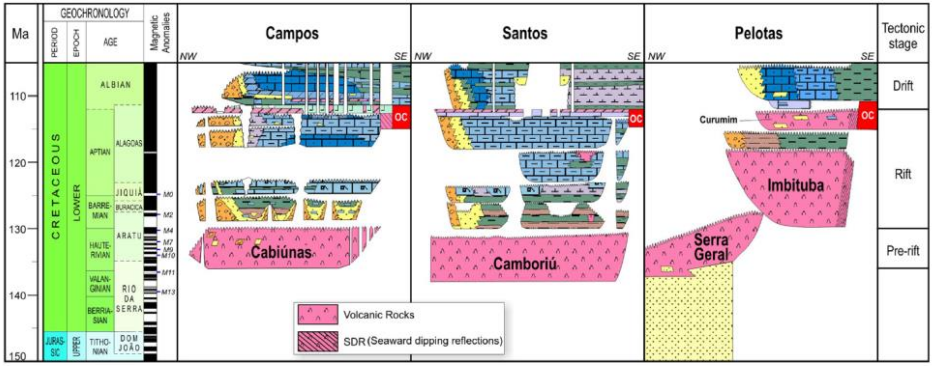

Figure 3. Correlation of stratigraphic charts of Campos, Santos and Pelotas Basin, with focus on the rift- and pre-rift phases as interpreted in this work, showing the correlation of volcanic sequences. Cabiúnas, Camboriú and Serra Geral Formations are equivalent (pre-rift sequences); Imbituba and Curumim Formations are here interpreted as rift-related volcanism deposited as seaward dipping reflectors; OC, Oceanic Crust. Modified from Winter et al. (2007), Moreira et al. (2007) and Bueno et al. (2007). Details of lithological representations on Milani et al. (2007b). Ages of magnetic anomalies recognized in this work are from Moulin et al. (2010) and absolute ages after Gradstein et al. (2004).

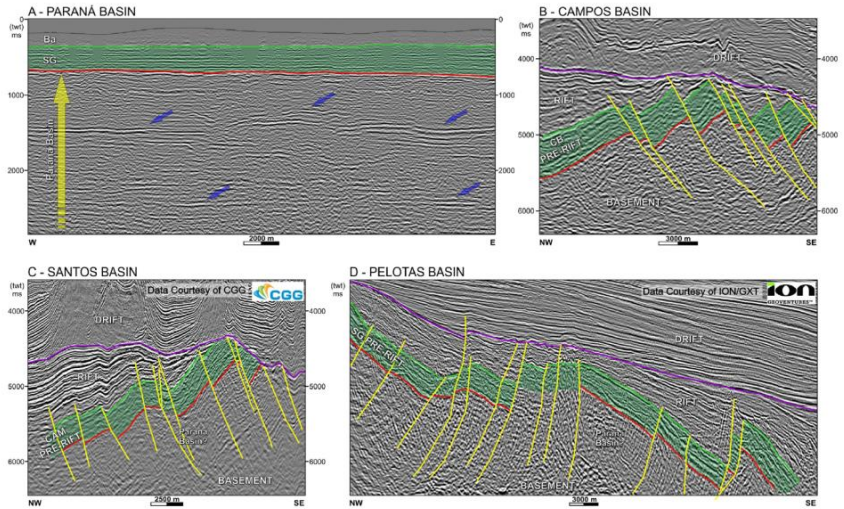

Figure 4. Seismic interpretation and correlation of the volcanic section (in green mask) in the Paraná Basin (A), and as pre-rift sequences on marginal basins: Campos (B); Santos (C) e Pelotas (D). SG, Serra Geral Formation; CB, Cabiúnas Formation; CAM, Camboriú Formation. Solid red lines represent the base of flows and green solid lines the top of flows. Yellow solid lines are faults related to rift-phase and purple solid line is the top of rift section (base of salt in Campos and Santos Basin). The yellow arrow in (A) shows the Paleozoic to Mesozoic sedimentary rocks of the Paraná Basin underneath the Serra Geral Formation and the blue arrows indicate sills intruded in the sedimentary section. Over the Serra Geral, Cretaceous sediments form the Bauru/Caiuá Group (Ba). There are some indications of seismic facies of sediments beneath the pre-rift section in Pelotas and Santos Basins, probably associated to Paleozoic section of the Paraná Basin. Locations of lines are displayed in Figure 1. 3D Seismic data of Santos Basin (C) courtesy of CGG. 2D Seismic data of Pelotas Basin (D) courtesy of ION-GXT. (For interpretation of the references to colour in this figure legend, the reader is referred to the web version of this article.)

Вид Seaward Dipping Reflectors (SDR) на сейсмических профилях

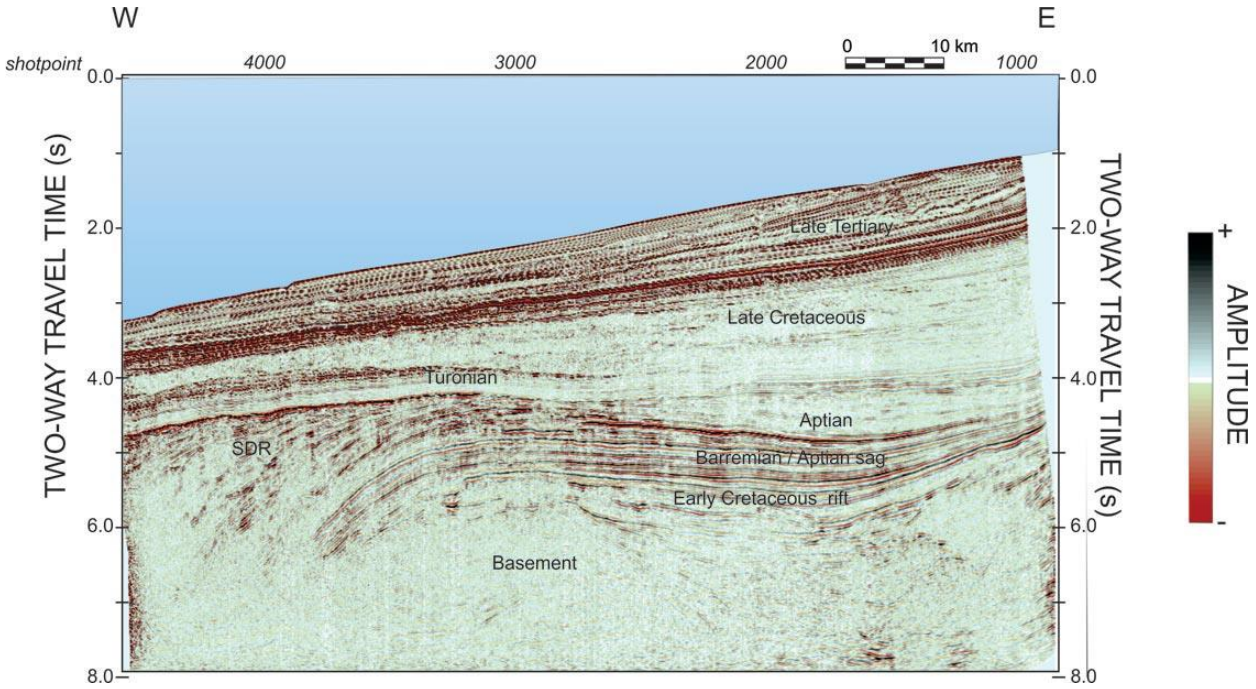

Намибия

GEOExPro

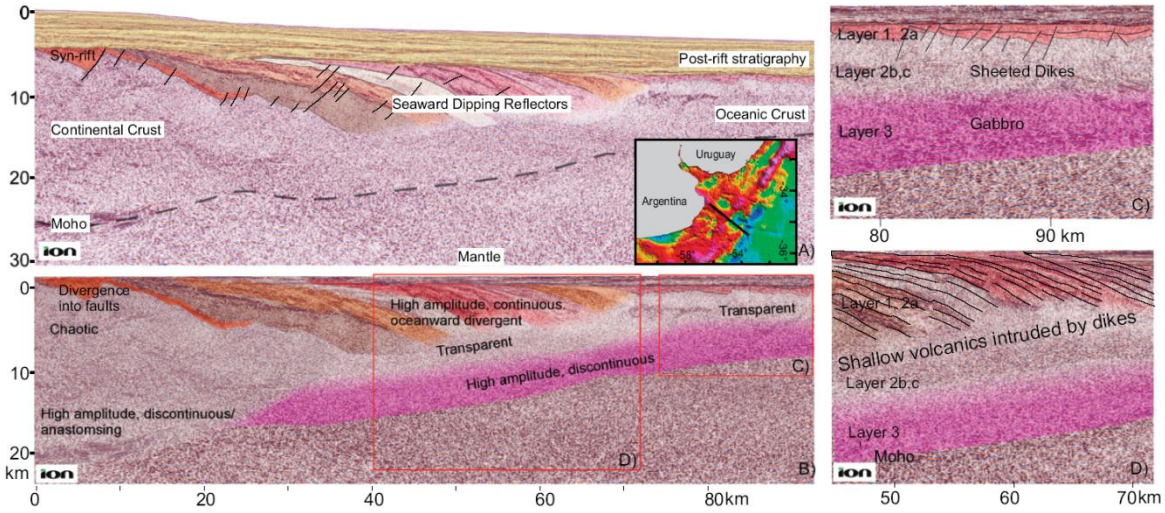

Figure 1. Profile across the Argentinian passive margin. A: Pre-stack depth-migrated seismic reflection profile with seaward-dipping reflectors (SDRs) and Moho interpreted. Inset is a free-air gravity anomaly map (Sandwell et al., 2014). B: Profile in A restored to a horizontal datum representing the margin geometry at the final SDR package. C: Tripartite seismic reflection character of the oceanic D: Tripartite seismic reflection character of the SDR packages.

Paton et al., 2017

GEOLOGY Data Repository item 2017131 | doi:10.1130/G38706.1

Вид Seaward Dipping Reflectors (SDR) на сейсмических профилях

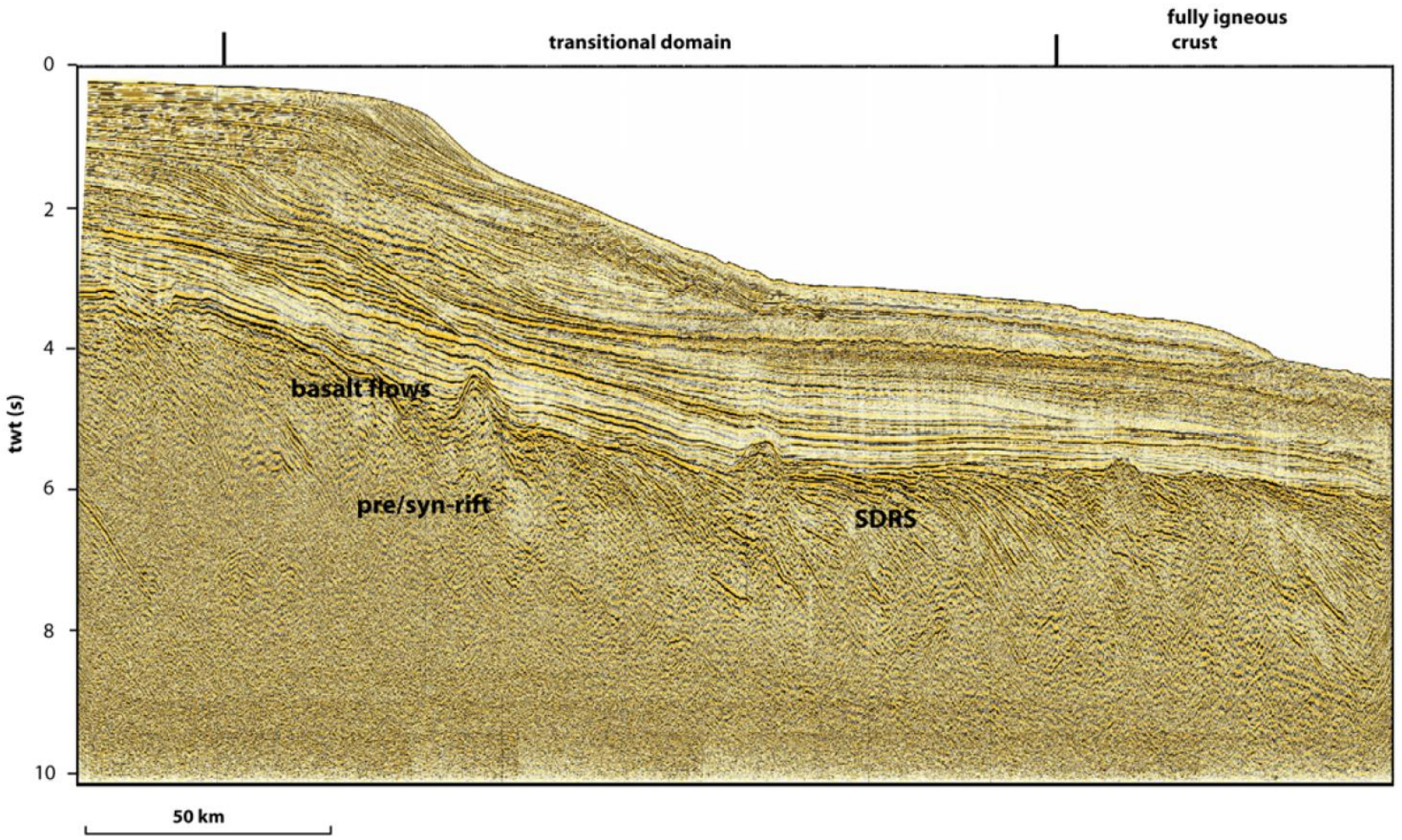

Fig. 4. Seismic example of the transitional domain along the Pelotas Basin (modified from Cainelli & Mohriak 1998). SDRs, seawards-dipping reflections; twt, two-way travel time.

From: Mohriak, W. U., Danforth, A., Post, P. J., Brown, D. E., Tari, G. C., Nemčok, M. & Sinha, S. T. (eds) 2013. *Conjugate Divergent Margins*. Geological Society, London, Special Publications, **369**, 167–183.
First published online March 26, 2013, http://dx.doi.org/10.1144/SP369.22

Вид Seaward Dipping Reflectors (SDR) на сейсмических профилях

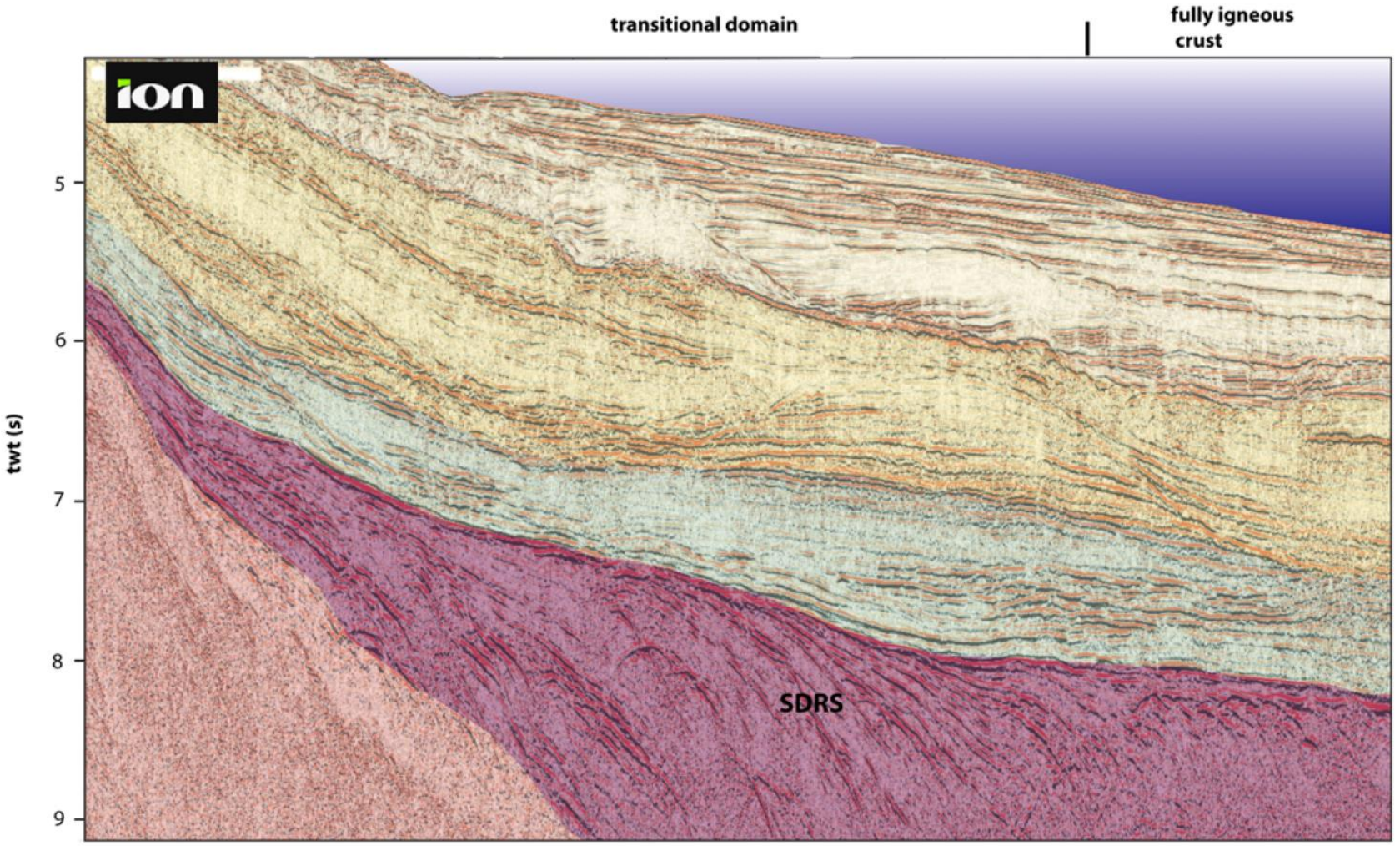

Fig. 9. Seismic example of the transitional domain along the Argentina margin. SDRs, seawards-dipping reflections; twt, two-way travel time.

From: Mohriak, W. U., Danforth, A., Post, P. J., Brown, D. E., Tari, G. C., Nemčok, M. & Sinha, S. T. (eds) 2013. *Conjugate Divergent Margins*. Geological Society, London, Special Publications, **369**, 167–183.
First published online March 26, 2013, http://dx.doi.org/10.1144/SP369.22

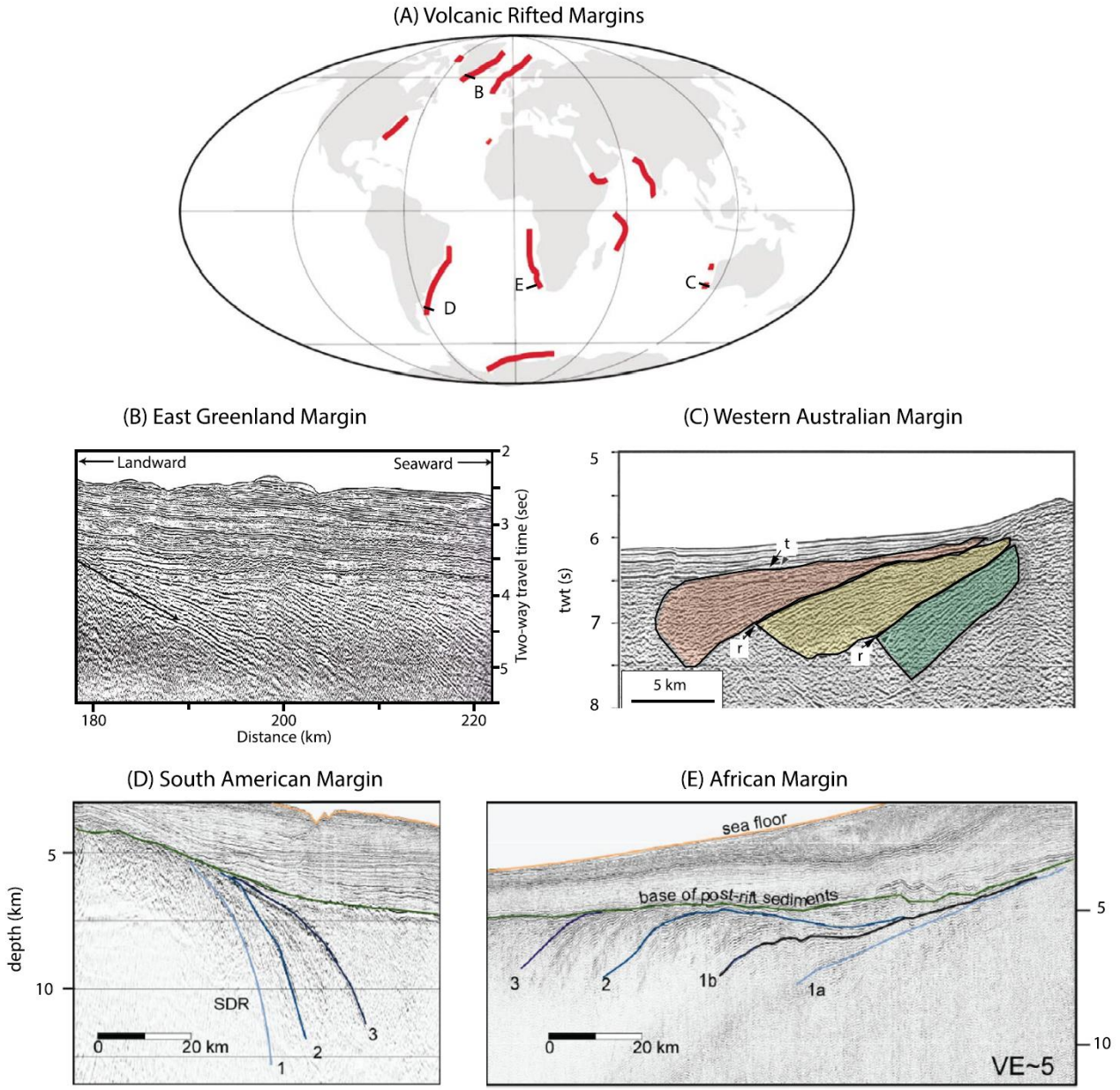

Fig. 1. (A) Location map of well documented volcanic rifted margins (red lines from Geoffroy, 2005) and the locations of the multichannel seismic (MCS) reflection lines shown below the map and in Fig. 6. (B) shows MCS data from the East Greenland Margin (from Hopper et al., 2003). (C) shows MCS data form the Exmouth Plateau of Australia showing the 3 separate overlapping SDRs 'units' indicated with colored shading (from Planke et al., 2000). The top of volcanic sequence is labeled 't', prominent reflectors dividing the sequence into sub-units are labeled 'r'. (D) show MCS lines on the Argentinean side of the South Atlantic and (E) shows similar data from the conjugate margin the South Africa with lines and letters representing interpreted boundaries between flow units (from Becker et al., 2016). (For interpretation of the references to color in this figure legend, the reader is referred to the web version of this article.)

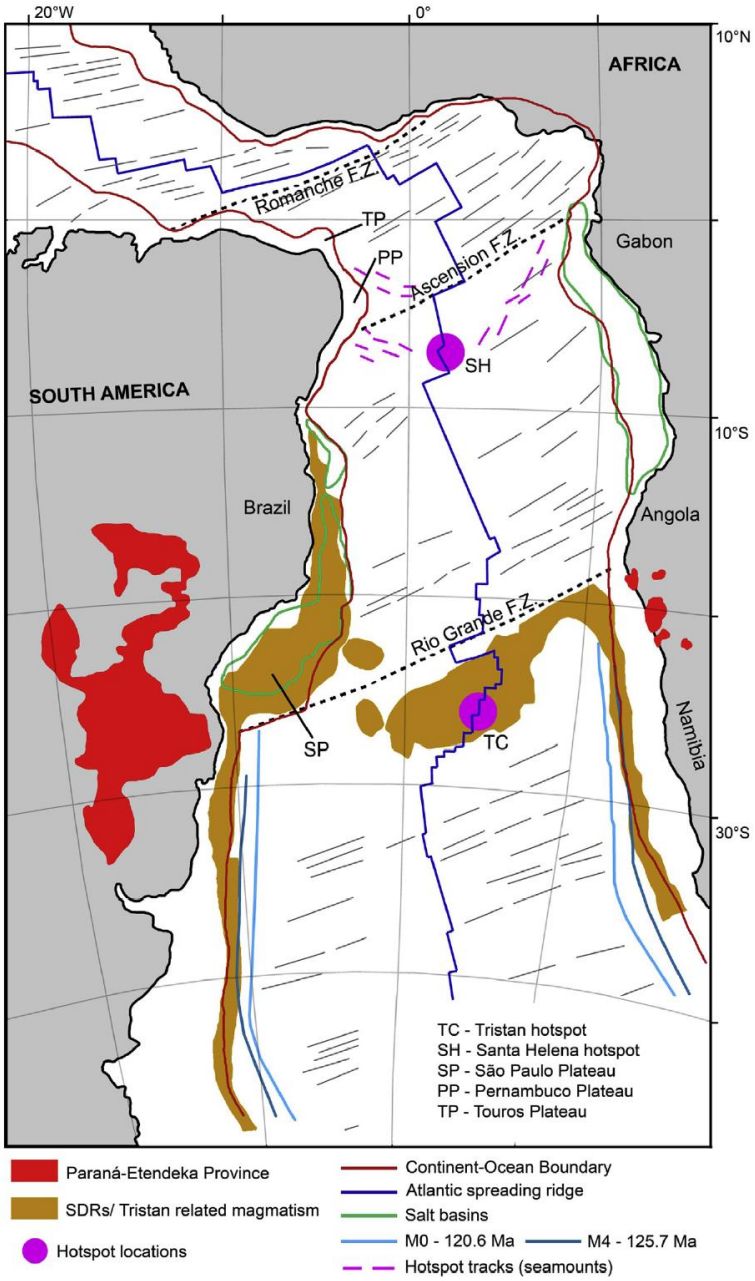

Fig. 3. Palaeogeographic reconstruction of the south Atlantic during the Santonian (83.5 Ma) based on geophysical data, considering a fixed Africa, modified from Torsvik et al. (2009). The authors proposed that at that time the Tristan and Santa Helena hotspots were located close to the spreading ridge. The ages of magnetic anomalies M0 and M4 are based on Müller et al. (1997). The positions ofthe seamounts that are possibly related to the Santa Helena hot spot are based on O'Neil et al. (2005), Adam et al. (2007) and Peyve and Skolotnev (2014).

Классическая модель строения вулканической пассивной окраины

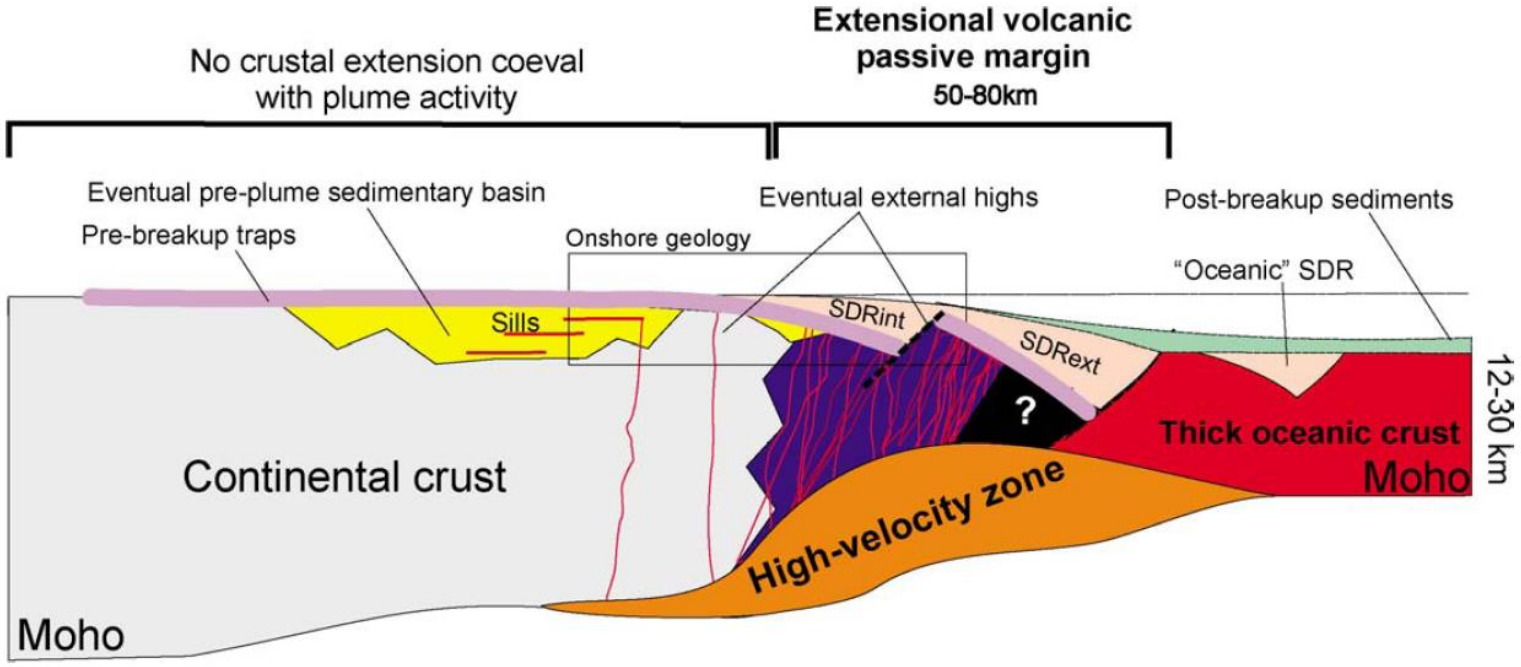

Fig. 1. Across-strike section of a volcanic passive margin. The presence of internal sedimentary basins is not the rule. SDRint and SDRext: respectively, internal and external seaward-dipping lavas and volcanic projections (i.e. 'Seaward-Dipping Reflectors' in offshore studies).

Fig. 1. Coupe schématique transverse d'une marge passive volcanique. L'existence de bassins sédimentaires en position interne n'est pas obligatoire. SDRint et SDRext : prismes de laves inclinées vers l'océan, en position interne ou externe (*Seaward-Dipping Reflectors*).

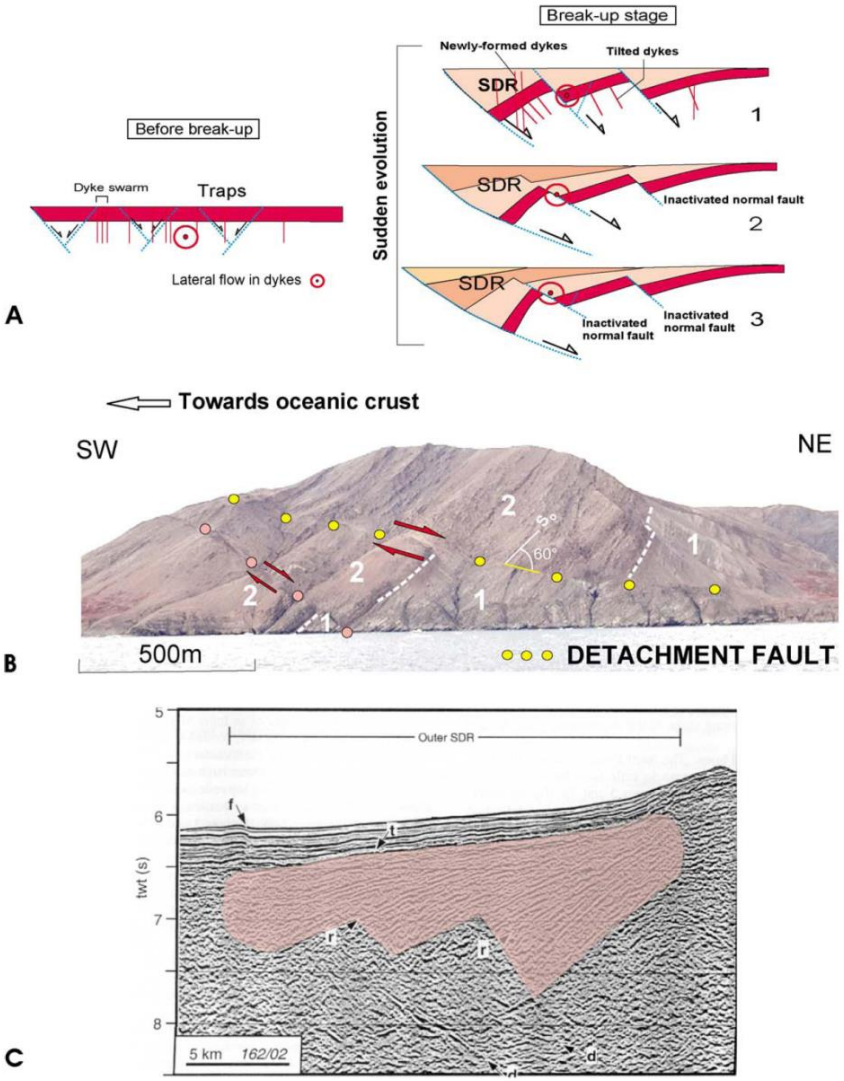

Fig. 6. (**A**) Formation of SDR at VPM [30]: SDR are syn-magmatic roll-over flexures accommodated by continentward-dipping normal faults. (**B**) Example of tilted continentward-dipping normal fault (yellow dots) in the internal SDR of SE-Baffin Bay (Svartenhuk Peninsula, see [31]). Note also the reactivation of a dyke as a secondary normal fault during the seaward-tilt of the lavas and projections (red dots). (**C**) Outer SDR-prism west of Australia [68]. Note the structure analogue to (**A**) and the existence of continentward-dipping faults (**d**) here interpreted as magma-injected normal faults.

Fig. 6. (**A**) Mode de formation des SDR, interprétés comme des anticlinaux en *roll-over* développés au-dessus de failles à pendage vers le continent [30]. (**B**) Exemple de SDR interne, avec faille basculée à pendage vers le continent (points jaunes). Noter la réactivation d'un dyke comme faille secondaire (points rouges) pendant le basculement de la série, constituée de laves et surtout de projections volcaniques. Svartenhuk, marge volcanique du Sud-Est de la baie de Baffin [31]. (**C**) Prisme SDR externe de la marge Ouest-Australienne. Noter la structuration analogue à celle de (**A**) et la présence de failles profondes à pendage vers le continent (**d**), interprétées comme étant injectées de magma [68].

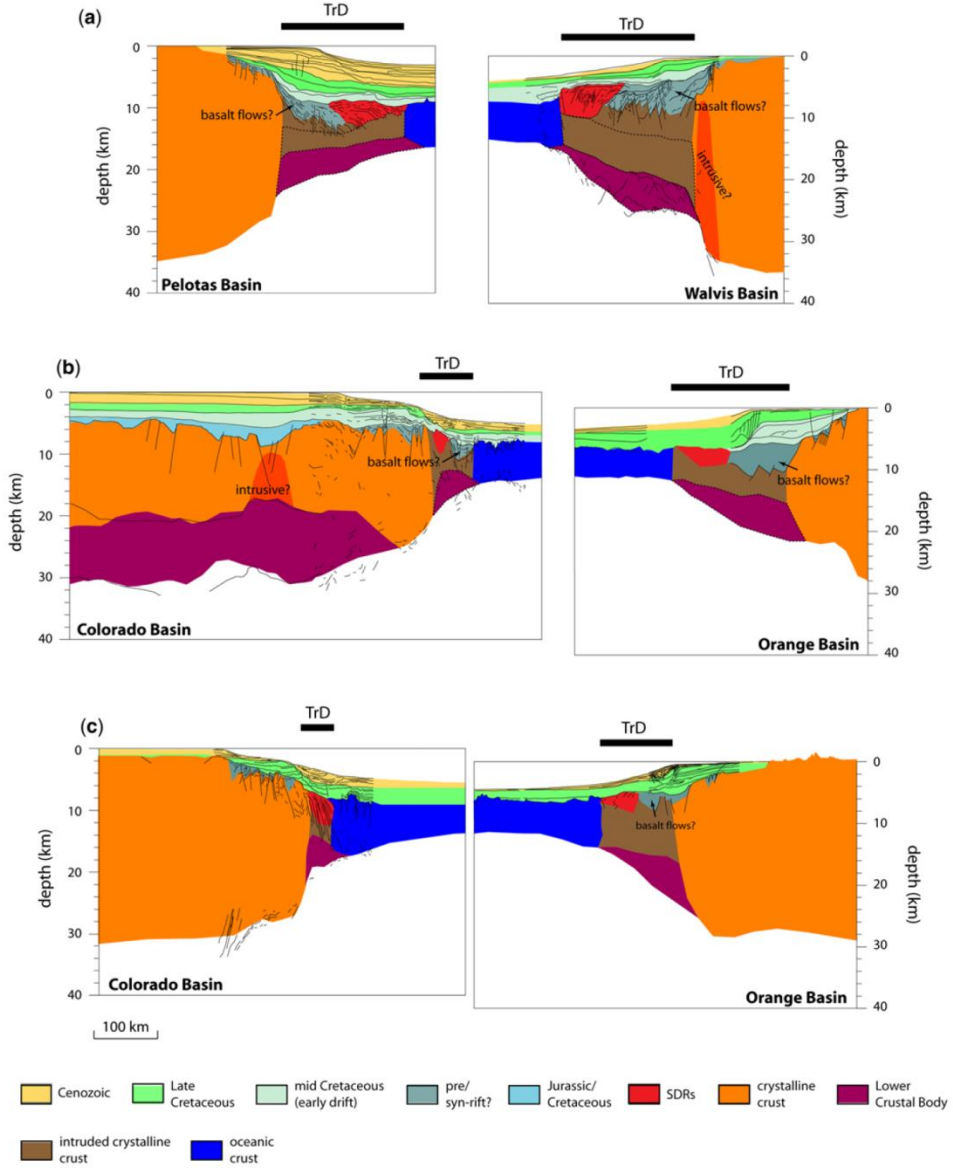

Fig. 3. Conjugate transects along segments of the southern South Atlantic margins, with a transitional domain (TrD) between the continental and oceanic crusts. The location of the profiles are shown in Figure 2. (**a**) Pelotas Basin (Brazil) – Walvis basin (Namibia); (**b**) and (**c**) Colorado Basin (Argentina) – Orange Basin (South Africa).

From: Mohriak, W. U., Danforth, A., Post, P. J., Brown, D. E., Tari, G. C., Nemčok, M. & Sinha, S. T. (eds) 2013. *Conjugate Divergent Margins*. Geological Society, London, Special Publications, **369**, 167–183.
First published online March 26, 2013, http://dx.doi.org/10.1144/SP369.22

Район плато Вёринг – одна из наиболее изученных вулканических окраин

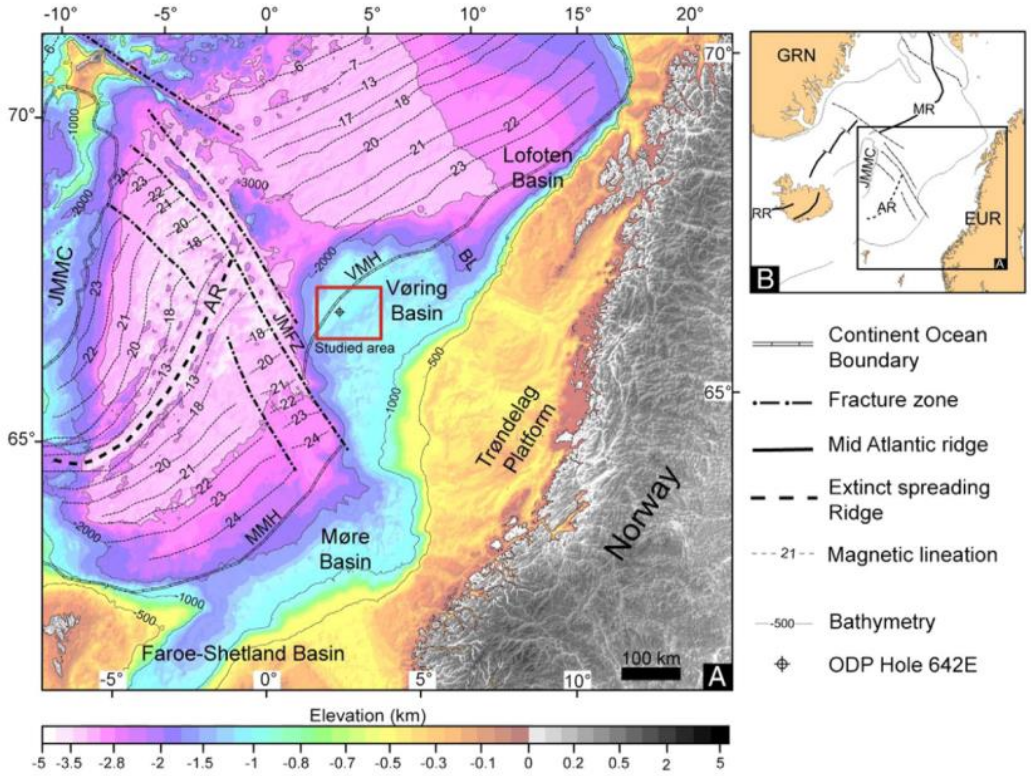

Fig. 1. Regional location map of the Mid-Norwegian margin based on GEBCO bathymetry/topography grid (The GEBCO_08 Grid, version 20100927, http://www.gebco.net). (A) Main physiographic features. AR: Aegir Ridge; BL: Bivrost Lineament; JMFZ: Jan. Mayen Fracture Zone; JMMC: Jan. Mayen Micro-Continent; MMH: Møre Marginal High; VMH: Vøring Marginal High. (B) Location of the regional map in the North Atlantic Area. EUR: Eurasia; GRN: Greenland; MR: Mohn's Ridge; RR: Reykjanes Ridge.

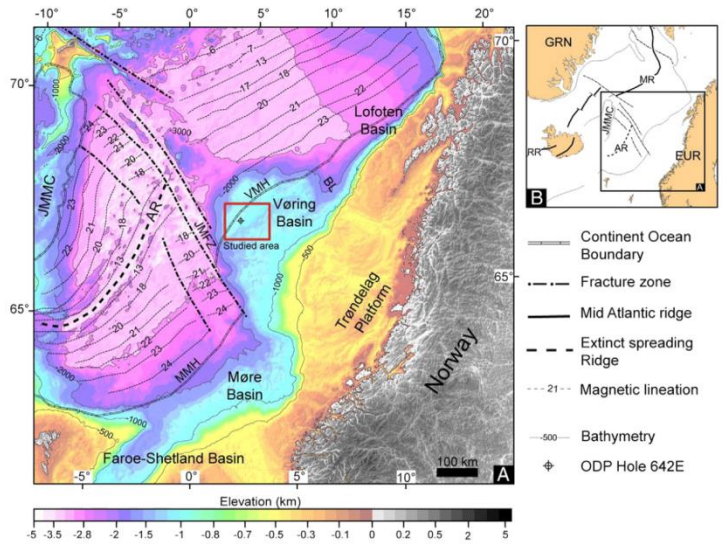

Fig. 1. Regional location map of the Mid-Norwegian margin based on GEBCO bathymetry/topography grid (The GEBCO_08 Grid, version 20100927, http://www.gebco.net). (A) Main physiographic features. AR: Aegir Ridge; BL: Bivrost Lineament; JMFZ: Jan. Mayen Fracture Zone; JMMC: Jan. Mayen Micro-Continent; MMH: Møre Marginal High; VMH: Vøring Marginal High. (B) Location of the regional map in the North Atlantic Area. EUR: Eurasia; GRN: Greenland; MR: Mohn's Ridge; RR: Reykjanes Ridge.

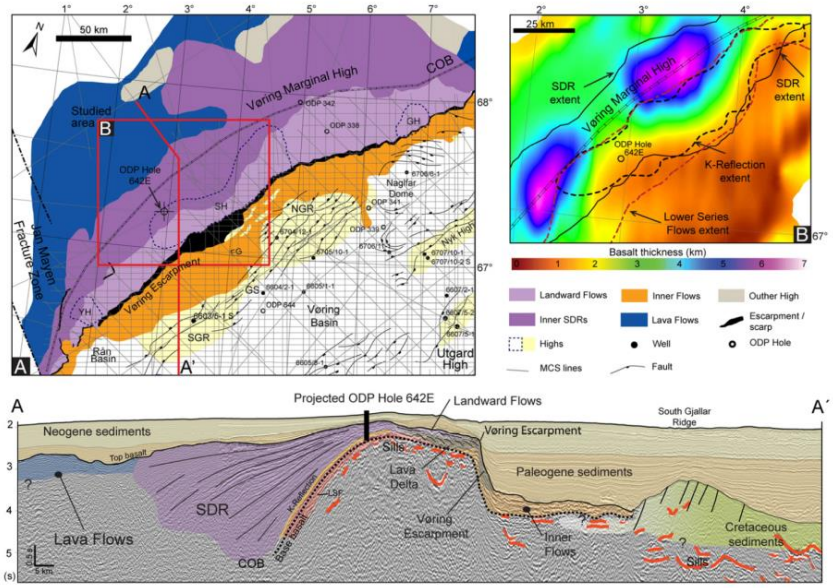

Fig. 3. (A) Distribution of the volcanic facies seismic units in the Vøring Margin. The 2D seismic profiles used in this study are indicated in the map. The profile A–A' shows an example of 2D mapping of the different seismic facies unit (in two way travel-time). (B) Basalt thickness map showing volcanic depocenters. COB: Continent–Ocean Boundary (located at the termination of the K-Reflection); FG: Fenris Graben; SH: Skoll High; GH: Grimm High; GS, Gleipne Saddle; JMFZ: Jan. Mayen Fracture Zone, LSF: Lower Series Flows; NGR: North Gjallar Ridge; SDR: Seaward-Dipping Reflector; SGR: South Gjallar Ridge; YH: Ygg High.

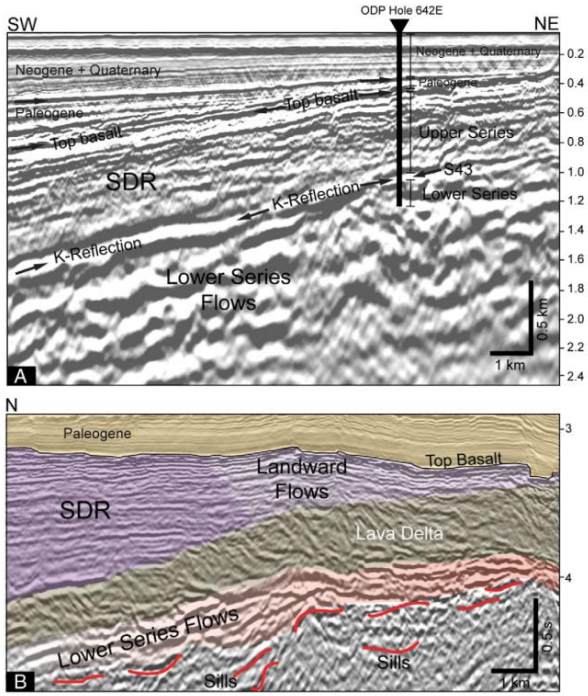

Fig. 4. (A) Depth converted (in km) seismic reflection profile showing the Lower Series Flows below the SDR in the Vøring Margin (the Upper Series in the ODP Hole 642E). The profile is tied to ODP Hole 642E. Locally the Lower Series Flows (the Lower Series in the ODP Hole 642E) top is defined as a strong negative in polarity reflection named the K-Reflection. (B) Seismic reflection profile (in two way travel-time) example showing the Lower Series Flows below the Lava Delta. Below the Lower Series Flows several sill intrusions are identified. See Fig. 6 for seismic profile location.

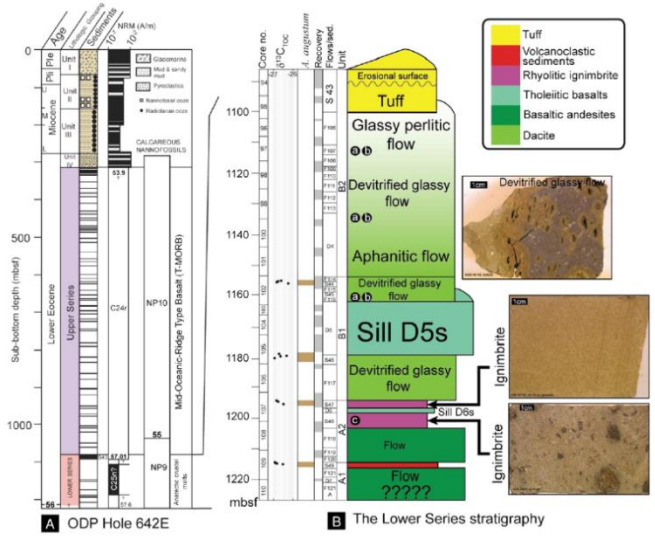

Fig. 2. (A) Log summary of ODP Hole 642E (Eldholm et al., 1987) showing the magneto stratigraphy (Schönharting and Abrahamsen, 1989) and biostratigraphy (Boutter and Mansum, 1989). The sedimentary section above the volcanic succession at ODP Hole 642E was divided into four lithological units (Eldholm et al., 1987). A glacial section (Unit I) lies above thick sequence of Miocene pelagic and hemipelagic sediments (Unit II and III), which are dominated by biogenic silicious muds and ooze. These open-water units are separated from an Eocene in age high energy near-shore unit IV by a 23 Ma hiatus (Goll, 1989). The unit IV consists mainly of volcanoclastic and altered volcanoclastic muds, sandy muds, and sands. Several ash layers were also identified within this unit and were related to the Eocene volcanism (Eldholm et al., 1987). (B) Lower Series log stratigraphy showing the different flows and sedimentary layers. The lithologies as well as some picture of some samples are shown. The location samples used for radiogenic age samples are indicated: (a) Lefticay and Johnson (1989), (b) Taylor and Morton (1989), and (c) Sinton and Duncan (1998). The new units A1, A2, B1, and B2 used in this study are indicated. The Braun boses indicate where *Apectodinium augustum* (*A. augustum*) was found in the Lower Series core stratigraphy. Stable carbon isotope values ($\delta^{13}C_{TOC}$) are indicated.

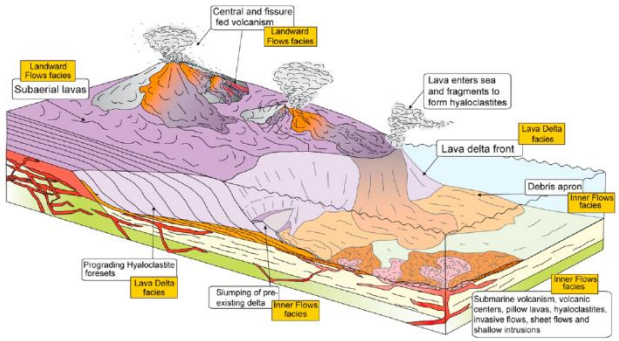

Figure 13. Schematic outline of the volcanic processes and associated deposits found around the escarpment area. T respective seismic volcanic facies (e.g., Inner Flows and Lava Delta) are also labeled. The sequence is characterized by mixture of subaerial and subaqueous eruptions and transitions from subaerial to subaqueous environment. Lava Delta prograde out from the paleoshoreline and deposit reworked volcanic debris/turbidite flows into the basin.

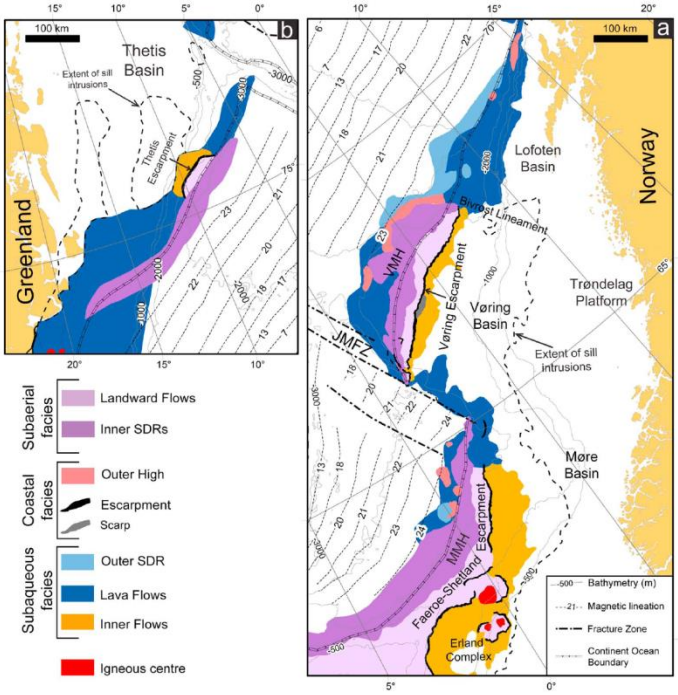

Figure 15. (a) Offshore distribution of the volcanic facies seismic units in the mid-Norwegian Margin updated from *Berndt et al.* [2001b]. The Vøring Escarpment and the Faeroe-Shetland Escarpment are indicated in the map. (b) Offshore distribution of the volcanic facies seismic units in the NE Greenland Margin. The Thetis Escarpment is indicated ion the map. See Figure 1 for location.

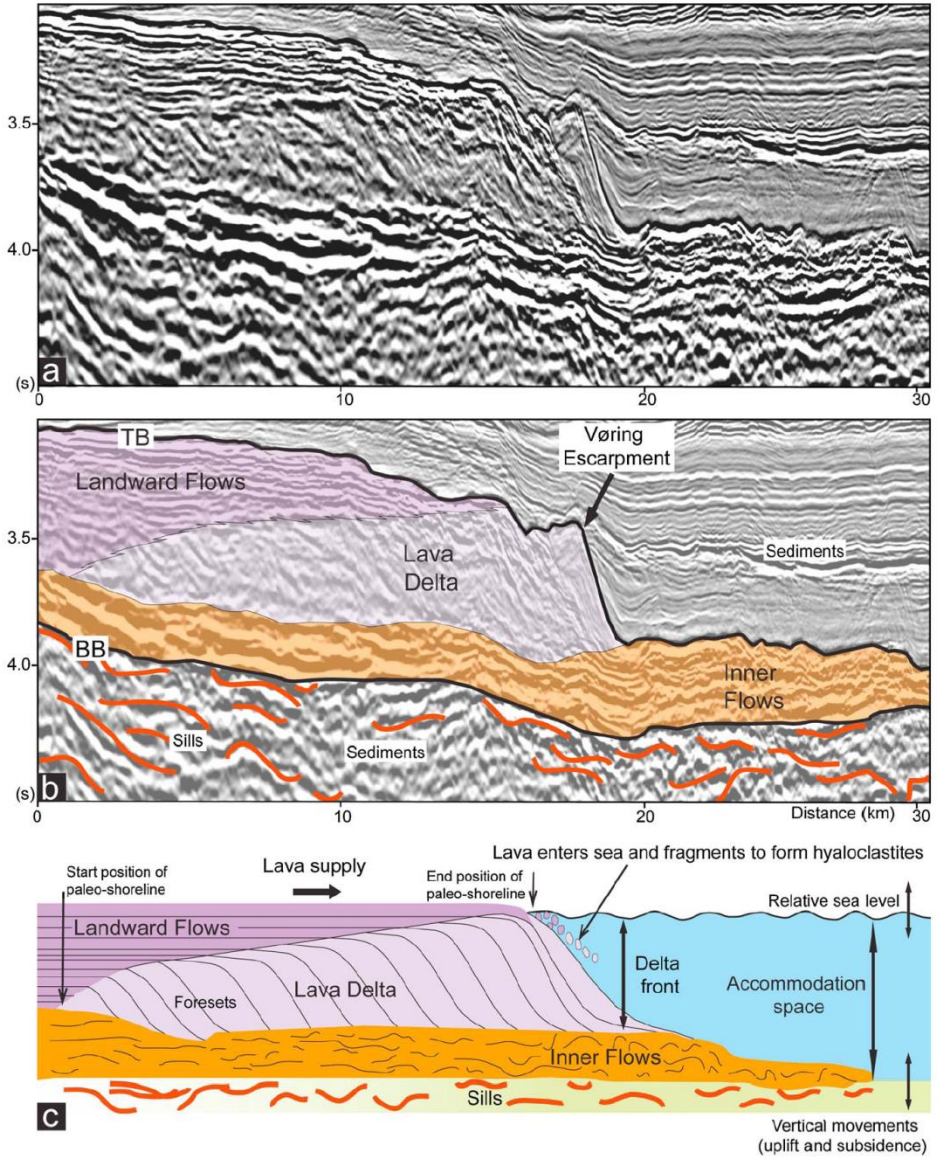

Figure 2. (a) Uninterpreted and (b) interpreted seismic sections highlighting key seismic facies units of the lava delta system. (c) Schematic representation (not to scale) of a developing lava-fed delta. TB: top basalt, BB: base basalt. Data courtesy of TGS.

Geology, published online on 1 October 2015 as doi:10.1130/G37086.1

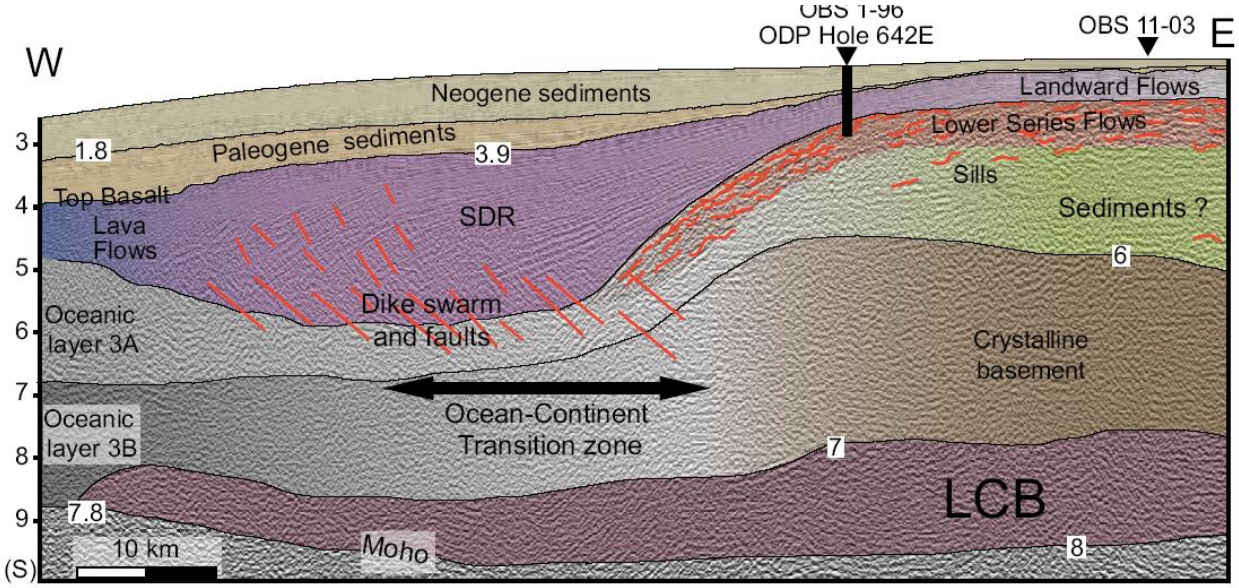

Figure 2. Seismic example of the ocean-continent transition in the Vøring margin (profile location in Fig. 1). The Seaward-Dipping Reflector (SDR) wedge is characterized by a divergent arcuate reflection pattern with increasing dip in the deeper part. The seismic velocity structure is determined using the Ocean Bottom Seismometer (OBS) profiles crossing the line, OBS 11-03 (Breivik et al., 2014) and OBS 1-96 (Mjelde et al., 2003). The profile is tied to Ocean Drilling Program (ODP) Hole 642E. The top of the crystalline basement shows velocity, Vp > 6.0 km/s. The Lower Crustal Body (LCB) near the base of the crust shows a high velocity (Vp > 7.0 km/s). The Moho is associated with a mantle velocity Vp > 8.0 km/s toward the continental crust and a Vp > 7.8 km/s toward the oceanic crust. (See the GSA Da the uninterpreted seismic profile.)

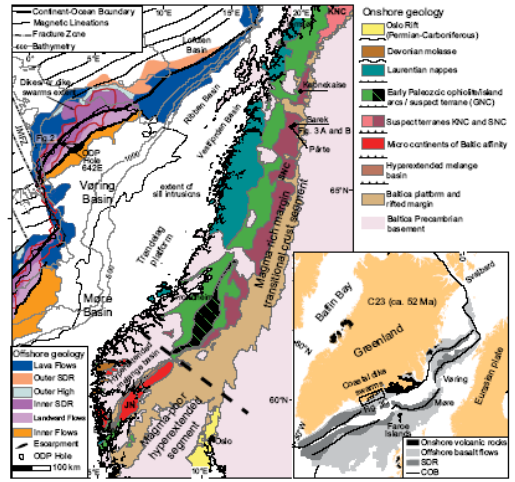

Figure 1. Onshore and offshore geological map and regional reconstruction ca. 52 Ma (inset; based on Gaina et al., 2009). Offshore: distribution of the volcanic seismic facies units in the mid-Norwegian margin. The extents of the dike swarms and sills are indicated. Onshore: simplified geological map of the different nappe complex (NC) defining the Scandinavian Caledonides. Two distinctive segments are identified for the pre-Caledonian margin of Baltica: the southern part is interpreted as hyperextended magma-poor segment (Andersen et al., 2012) and the central part is interpreted as transitional crust of magma-rich margin. JMFZ—Jan Mayan Fracture Zone; GNC—Gula Nappe complex; JN—Jotun Nappe; KNC—Kalak Nappe Complex; SNC—Seve Nappe Complex; SDR—Seaward-Dipping Reflector; ODP—Ocean Drilling Program; COB—continent-ocean boundary.

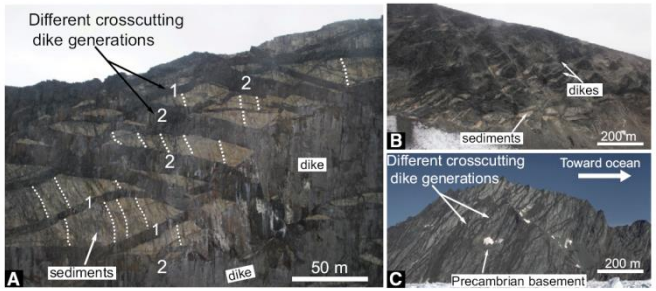

Figure 3. A: Different crosscutting dike generations. The sediments show vertical layering (dashed white lines). The variable angles between dikes and bedding indicate different intrusion stages during tilting of the margin. The lozenge-shaped wall-rock fragments developed their shape during successive generations of dilational dikes (1 and 2). B: Outcrop of Favoritkammen sedimentary group highly intruded by mafic dike swarm with a dike density to 70%–80%. C: East Greenland coastal dike swarms.

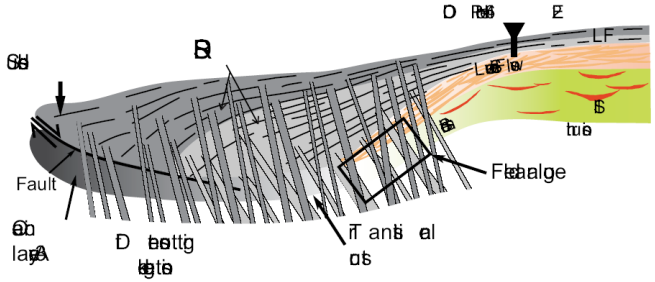

Figure 4. Simplified schematic illustration (not to scale) of different feeder dike generations emplaced during the seaward-dipping reflector (SDR) growth. The first dike generation (light gray) is tilted and crosscut by a newer dike generation (dark gray) showing a vertical to subvertical dip. Part of the transitional crust below the SDR is composed of highly intruded sedimentary basin. The black box shows the position of the field analogue. LF—Landward Flows; ODP—Ocean Drilling Program.

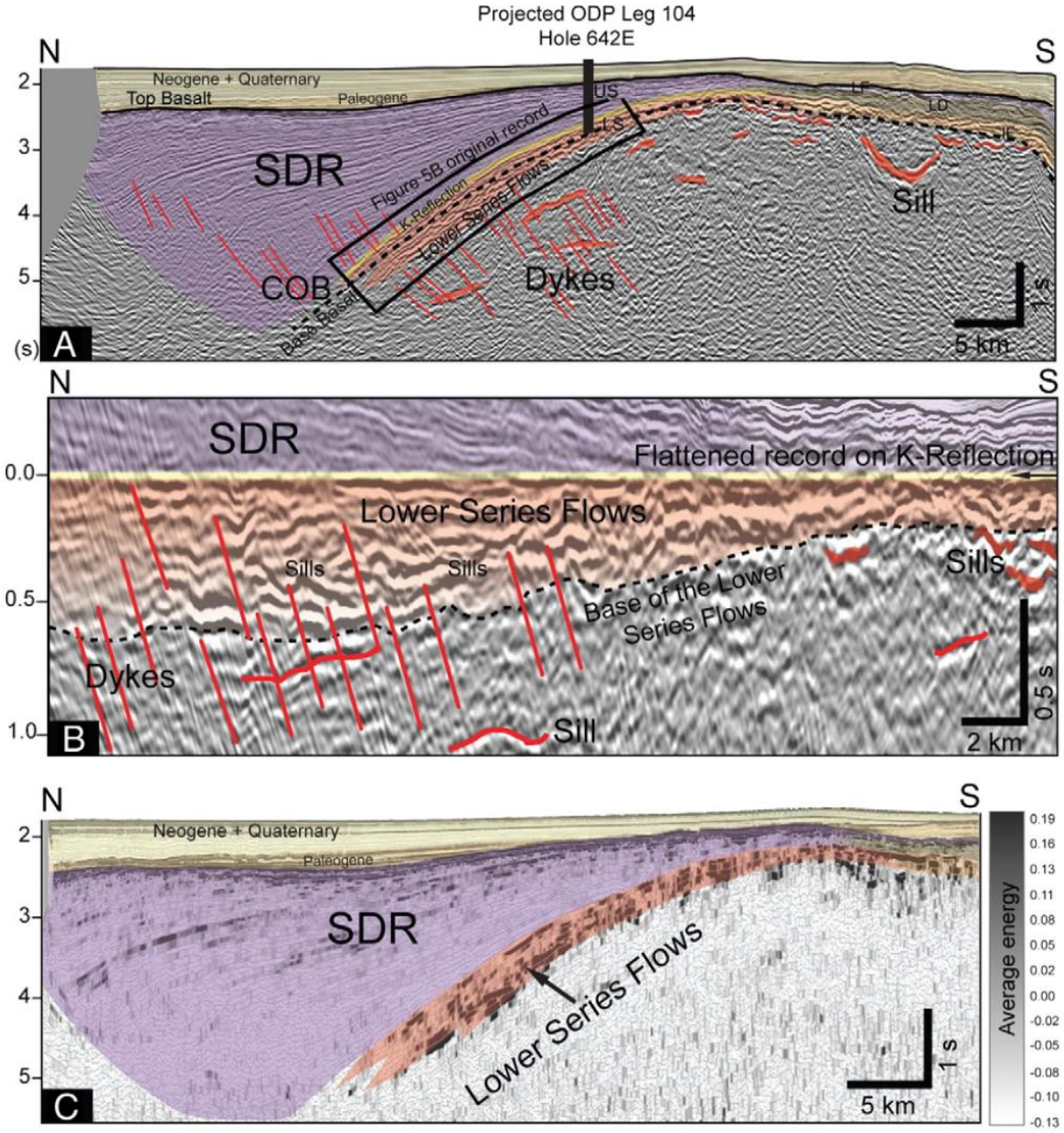

Fig. 5. (A) Seismic reflection profile showing the Lower Series Flows below the SDR in the Vøring Margin (in two way travel-time). (B) Flattened record on the K-Reflection allowing better imaging of the internal reflections structures of the Lower Series Flows. (C) Example of average energy attribute for the Lower Series Flows showing a high reflected energy compared to the Inner SDR and the underlying structures. IF: Inner Flows; LF: Landward Flows; LD: Lava Delta; LS: Lower Series; US: Upper Series. See Fig. 6 for seismic profile location.

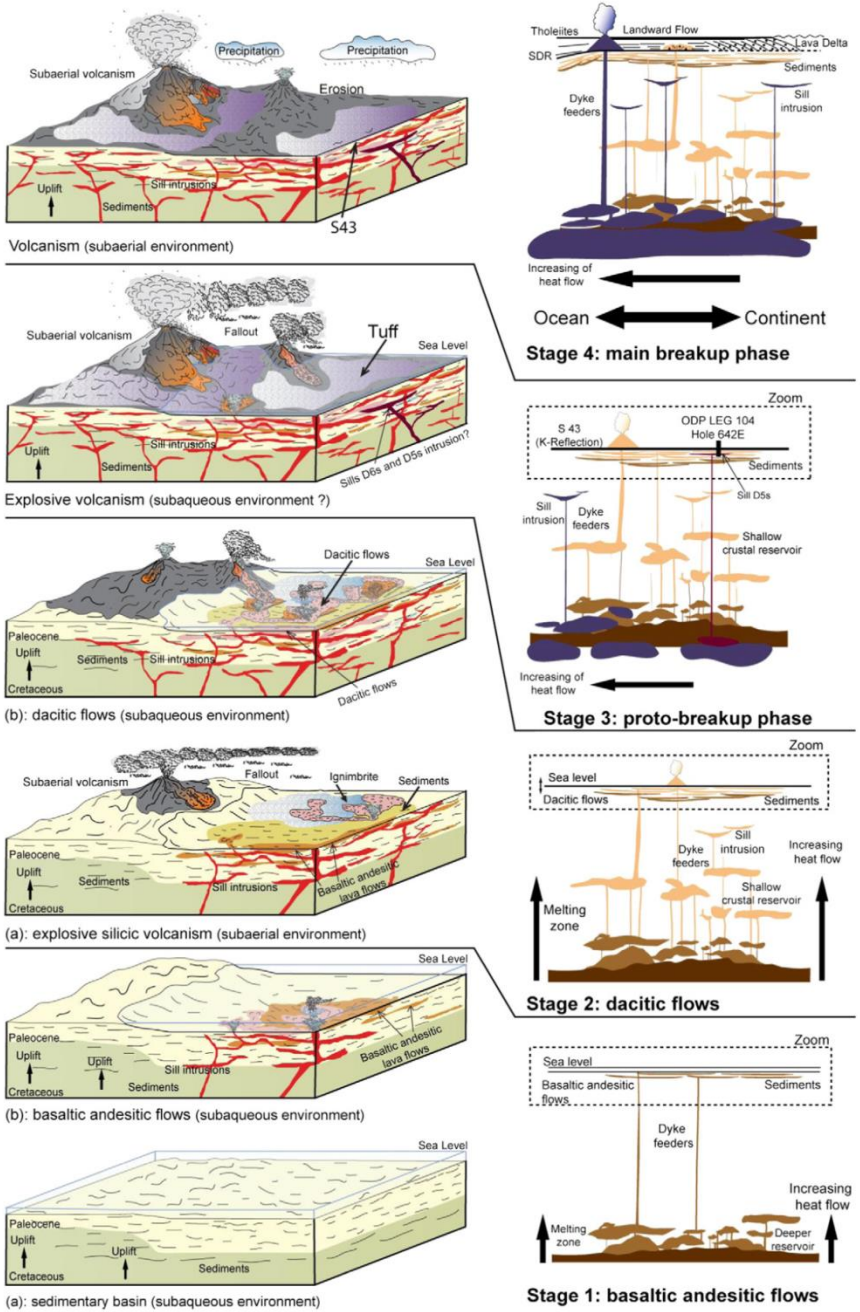
Subaerial volcanism
Precipitation
Precipitation
Erosion
Uplift
Sediments
Sill intrusions
S43
Volcanism (subaerial environment)
Subaerial volcanism
Fallout
Tuff
Sea Level
Uplift
Sediments
Sill intrusions
Sills D6s and D5s intrusion?
Explosive volcanism (subaqueous environment ?)
Dacitic flows
Sea Level
Paleocene
Uplift
Sediments
Sill intrusions
Cretaceous
Dacitic flows
(b): dacitic flows (subaqueous environment)
Subaerial volcanism
Fallout
Ignimbrite
Sediments
Paleocene
Uplift
Sediments
Sill intrusions
Basaltic andesitic lava flows
Cretaceous
(a): explosive silicic volcanism (subaerial environment)
Sea Level
Paleocene
Uplift
Uplift
Sill intrusions
Basaltic andesitic lava flows
Sediments
Cretaceous
(b): basaltic andesitic flows (subaqueous environment)
Sea Level
Paleocene
Uplift
Uplift
Sediments
Cretaceous
(a): sedimentary basin (subaqueous environment)
Tholeiites
Landward Flow
Lava Delta
SDR
Sediments
Dyke feeders
Sill intrusion
Increasing of heat flow
Ocean
Continent
Stage 4: main breakup phase
Zoom
S 43 (K-Reflection)
ODP LEG 104 Hole 642E
Sediments
Sill D5s
Sill intrusion
Dyke feeders
Shallow crustal reservoir
Increasing of heat flow
Stage 3: proto-breakup phase
Zoom
Sea level
Dacitic flows
Sediments
Dyke feeders
Sill intrusion
Increasing heat flow
Shallow crustal reservoir
Melting zone
Stage 2: dacitic flows
Zoom
Sea level
Basaltic andesitic flows
Sediments
Dyke feeders
Increasing heat flow
Melting zone
Deeper reservoir
Stage 1: basaltic andesitic flows

Вулканическая континентальная окраина Уругвая

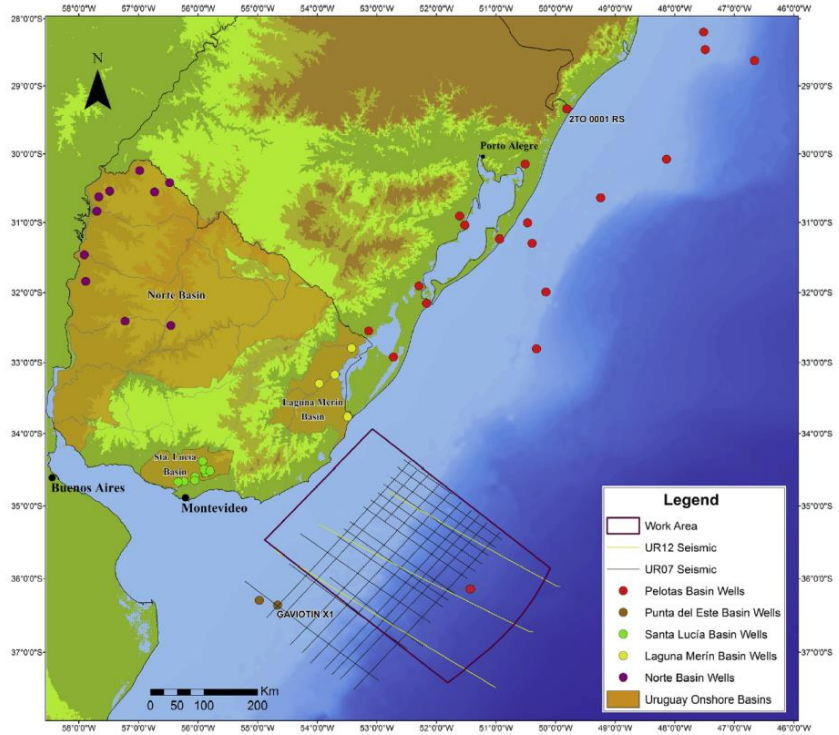

Fig. 1. Location of the study area (purple rectangle) within the Pelotas Basin in offshore Uruguay. Locations of 2D seismic lines used in this study and location of wells drille Pelotas Basin and in other nearby basins are also shown. Raya-1 approximate well location taken from Spectrum (2015). (For interpretation of the references to colour in this fi legend, the reader is referred to the web version of this article.)

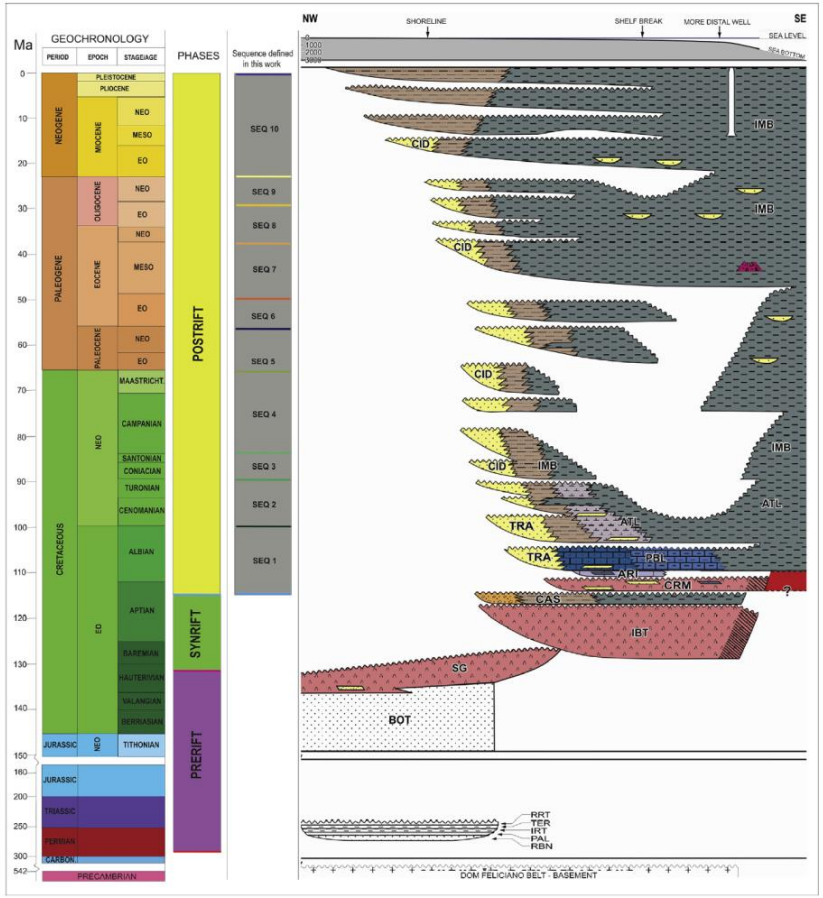

Fig. 28. Correlation between the lithostratigraphy of the Pelotas Basin proposed in Bueno et al. (2007) and the depositional sequences defined in this work. Modified from Bueno et al. (2007).

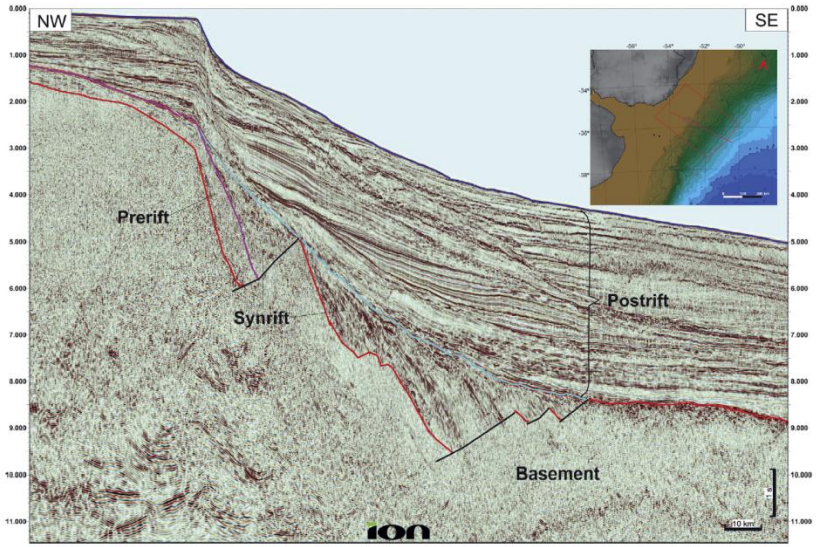

Fig. 2. 2D dip seismic section in time (TWT) of Pelotas Basin with interpreted megasequences. Vertical scale in seconds.

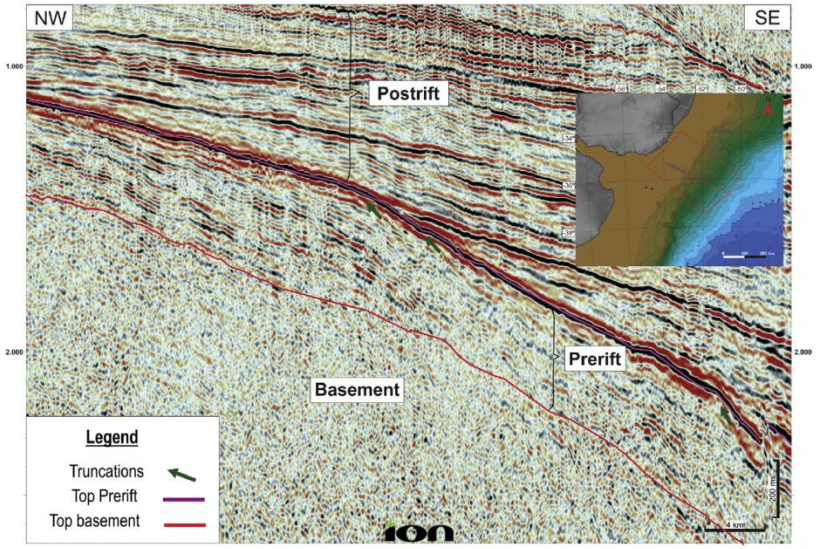

Fig. 3. Seismic character of the Prerift megasequence showing truncation of reflectors at the top of the megasequence. Vertical scale in seconds (TWT).

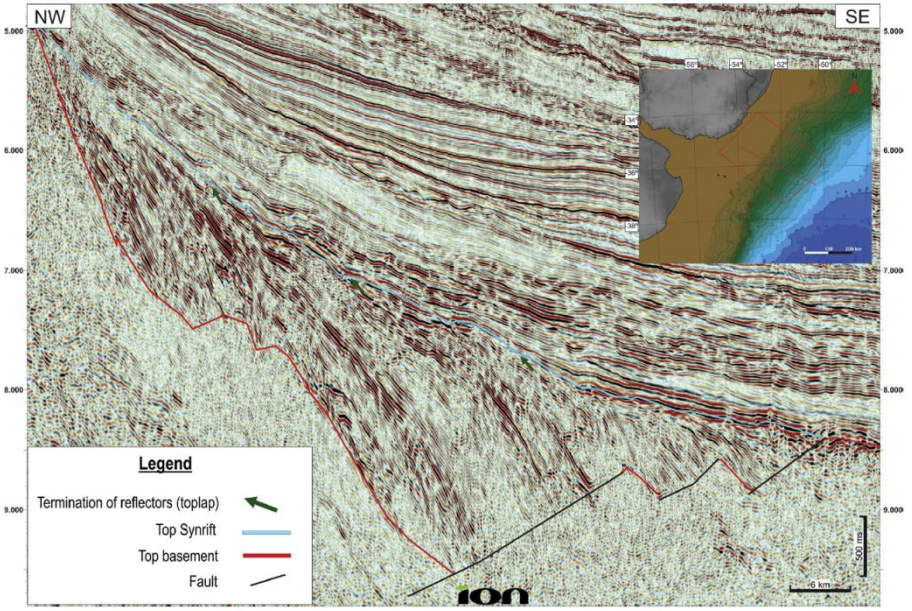

Fig. 7. Seismic character of the synrift associated with the SDRs in dip seismic section. Vertical scale in seconds (TWT).

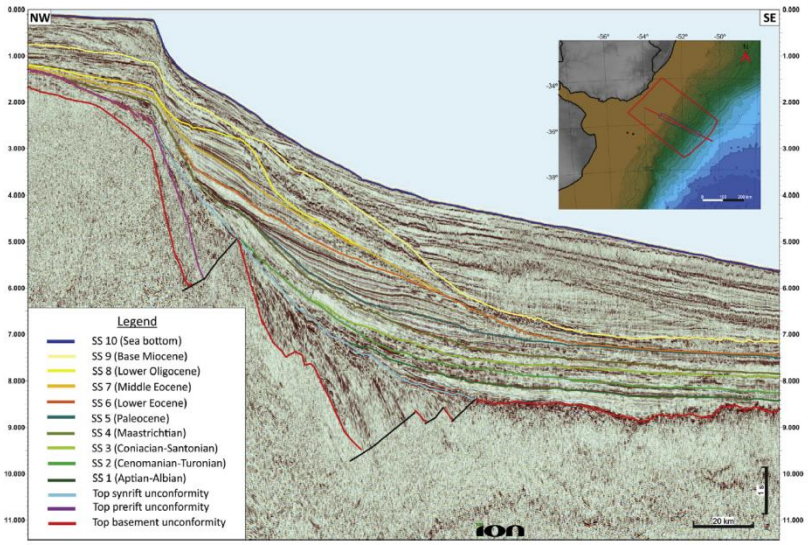

Fig. 9. 2D dip seismic section of the Pelotas Basin showing the interpreted depositional sequences. Vertical scale in seconds (TWT).

Некоторые крупные вулканические постройки

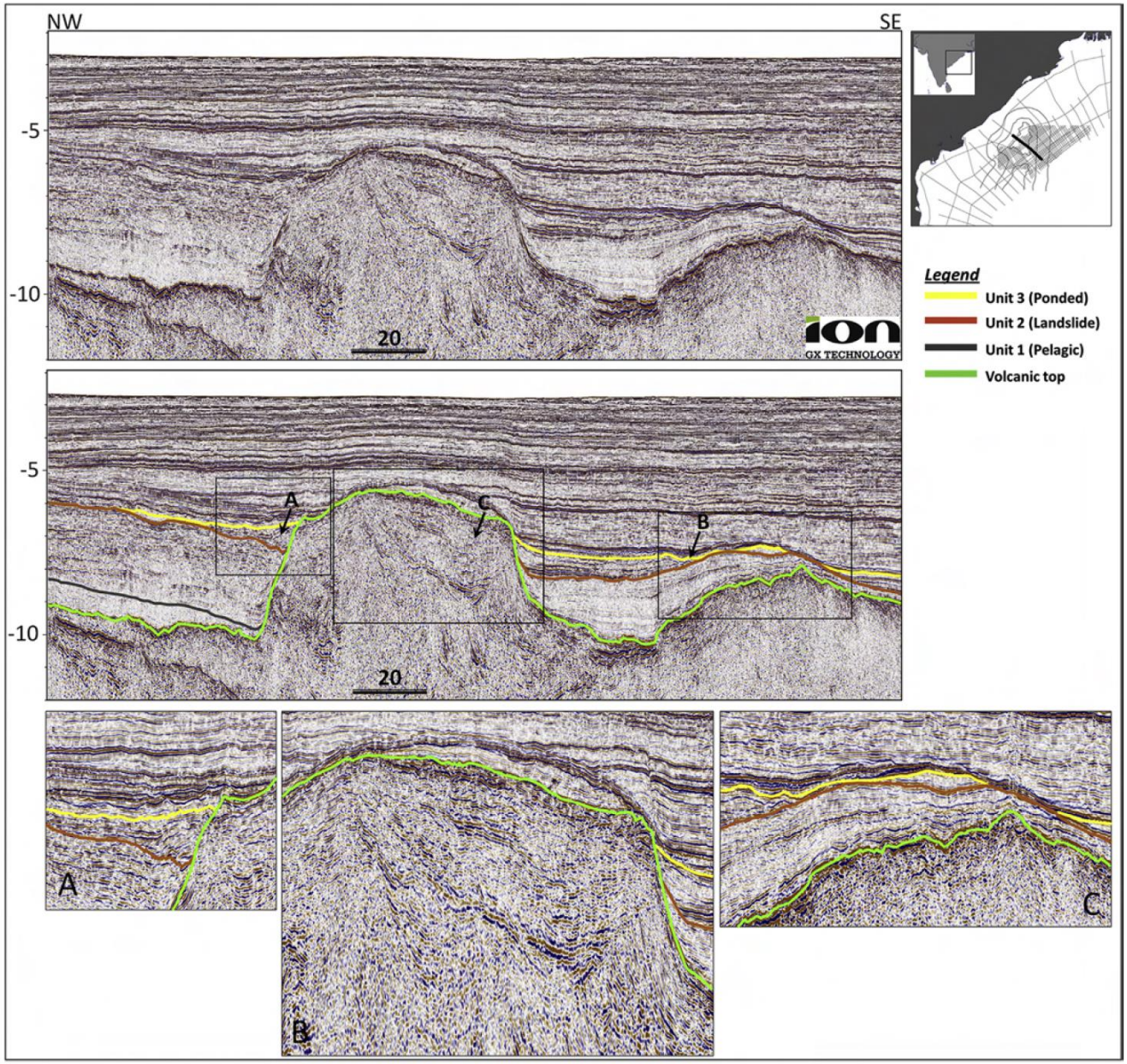

Fig. 3. Portion of the dip-oriented profile IE-1400 crossing the northern segment of the 85°E Ridge. Both the horizontal and vertical scales are in kilometers. A — slumping and syn-depositional disturbances within the ponded unit, B — upwarped landslide unit over the eastern arch, C — presence of lava deltas within the ridge indicating sub-aerial volcanism.

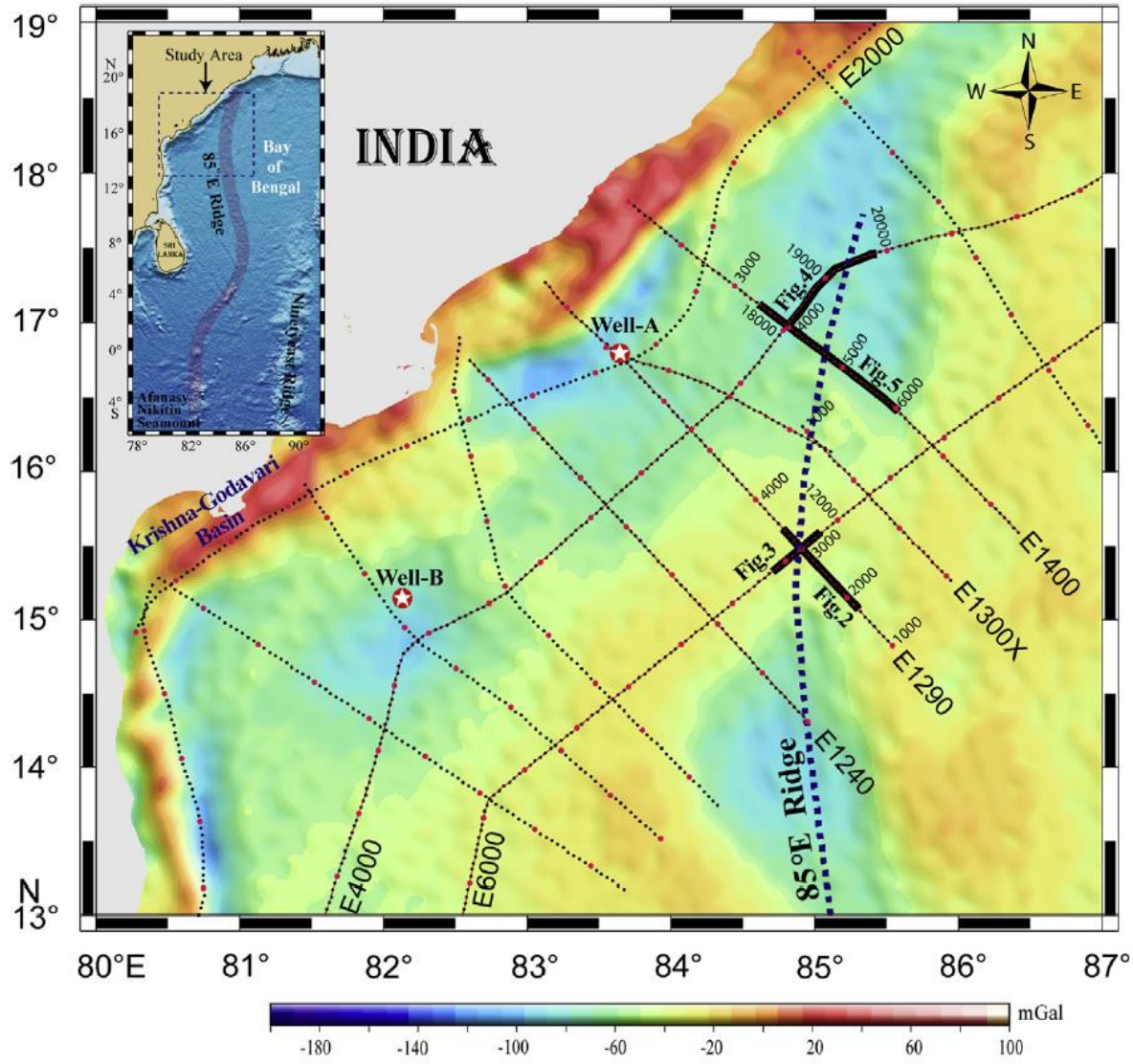

Fig. 1. Satellite free-air gravity anomaly color code map of the 85°E Ridge and adjacent area of the Bay of Bengal (Sandwell et al., 2014). Black dotted lines show the network of GXT multi-channel seismic profiles investigated in the present work. The solid red circles with white star show the locations of industry (ONGC) drill wells "A" and "B" locat Eastern Continental Margin of India. Thick black lines show the locations of seismic sections illustrated in Fig. 2 and 3. The inset map shows the satellite derived bathymetry i of the Bay of Bengal and trace of the 85°E Ridge from the Mahanadi Basin in the north Bay of Bengal to the Afanasy Nikitin seamount in the equatorial Indian Ocean interpretation of the references to colour in this figure legend, the reader is referred to the web version of this article.)

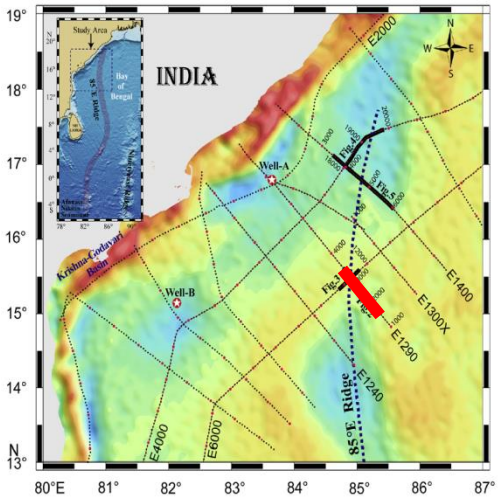

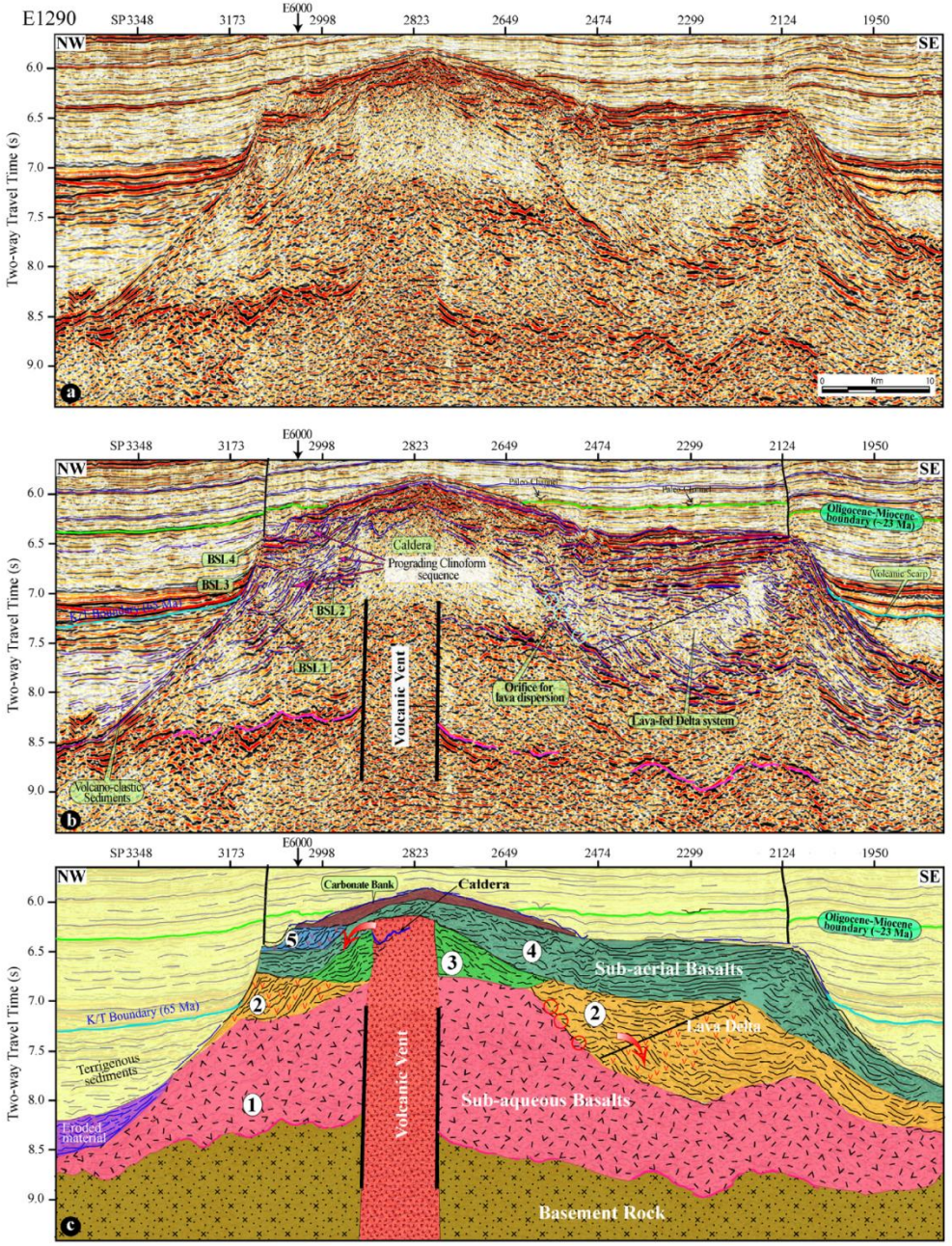

Fig. 2. The section of the seismic profile E1290 illustrates the internal structure of the 85°E Ridge. And its interpreted line diagram is shown below. The section displays characteristic of volcanic plug, lava-fed delta units, etc. The ridge structure is completely buried under the thick Bengal Fan sediments deposited since the Oligocene-Miocene time (~23 Ma). SP shown along the horizontal-axis and BSL marked within the ridge structure indicate the shot-point and Bottomset/Base of the Lava Delta, respectively.

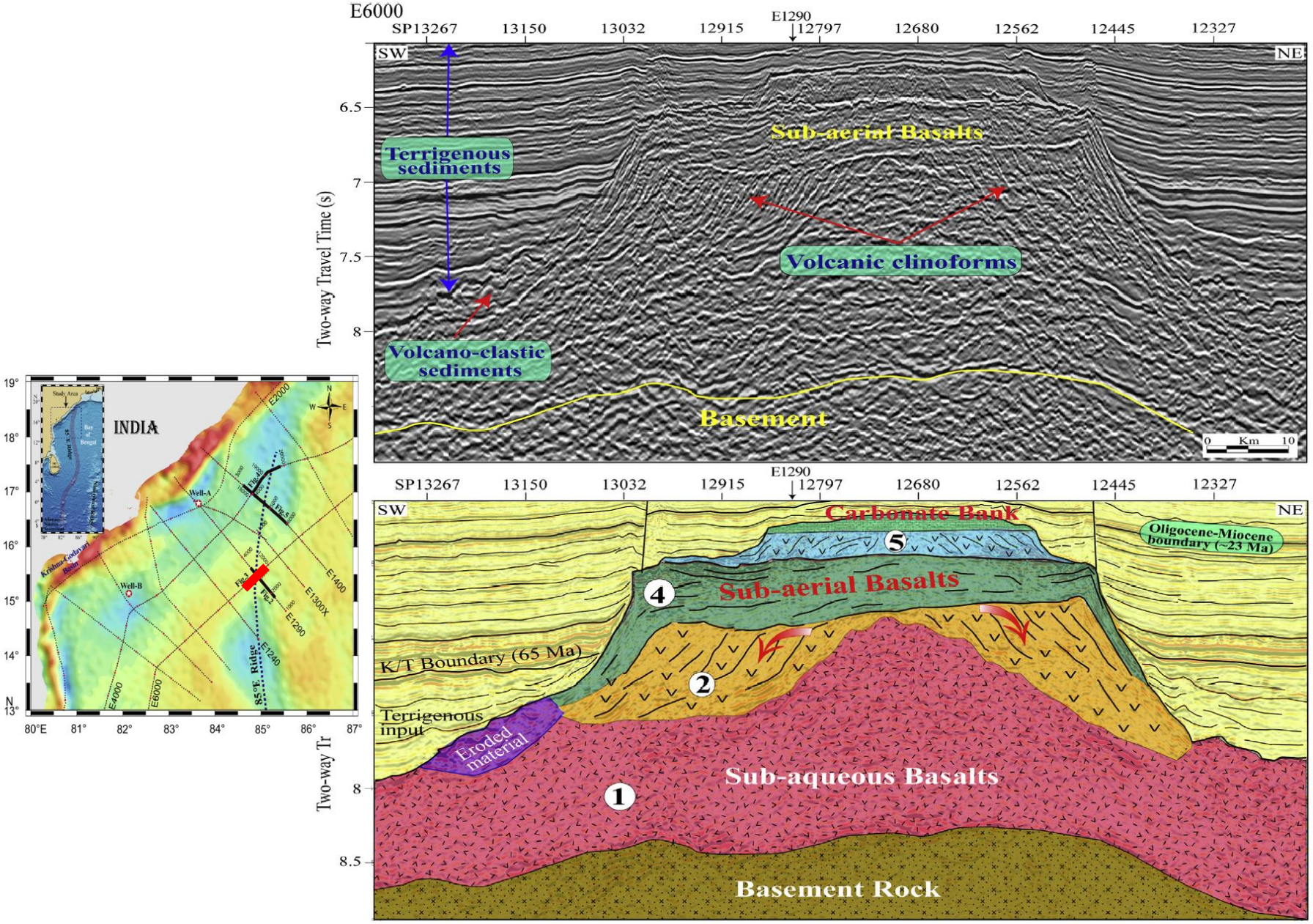

Fig. 3. The coast parallel deep-water seismic profile E6000 crossing the 85°E Ridge and its interpretation are shown (for location, see Fig. 1). The profile nearly orthogonally crosses the profile E1290.

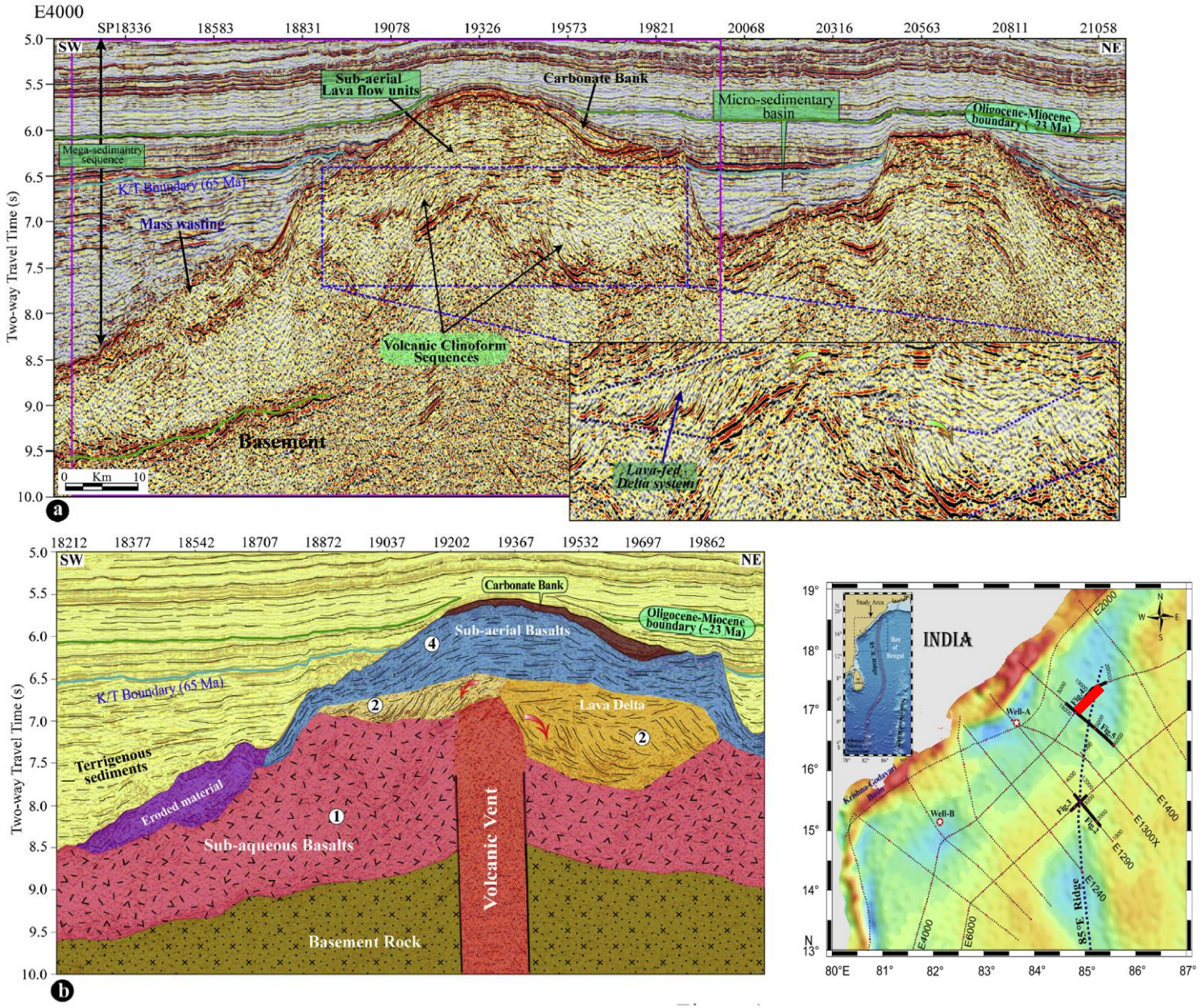

Fig. 4. The coast parallel offshore Mahanadi Basin profile E4000 depicting the two peaks of the 85°E Ridge. Packs of volcanic clinoform reflectors within the ridge structure and mass-wasting on west flank of the ridge are clearly seen.

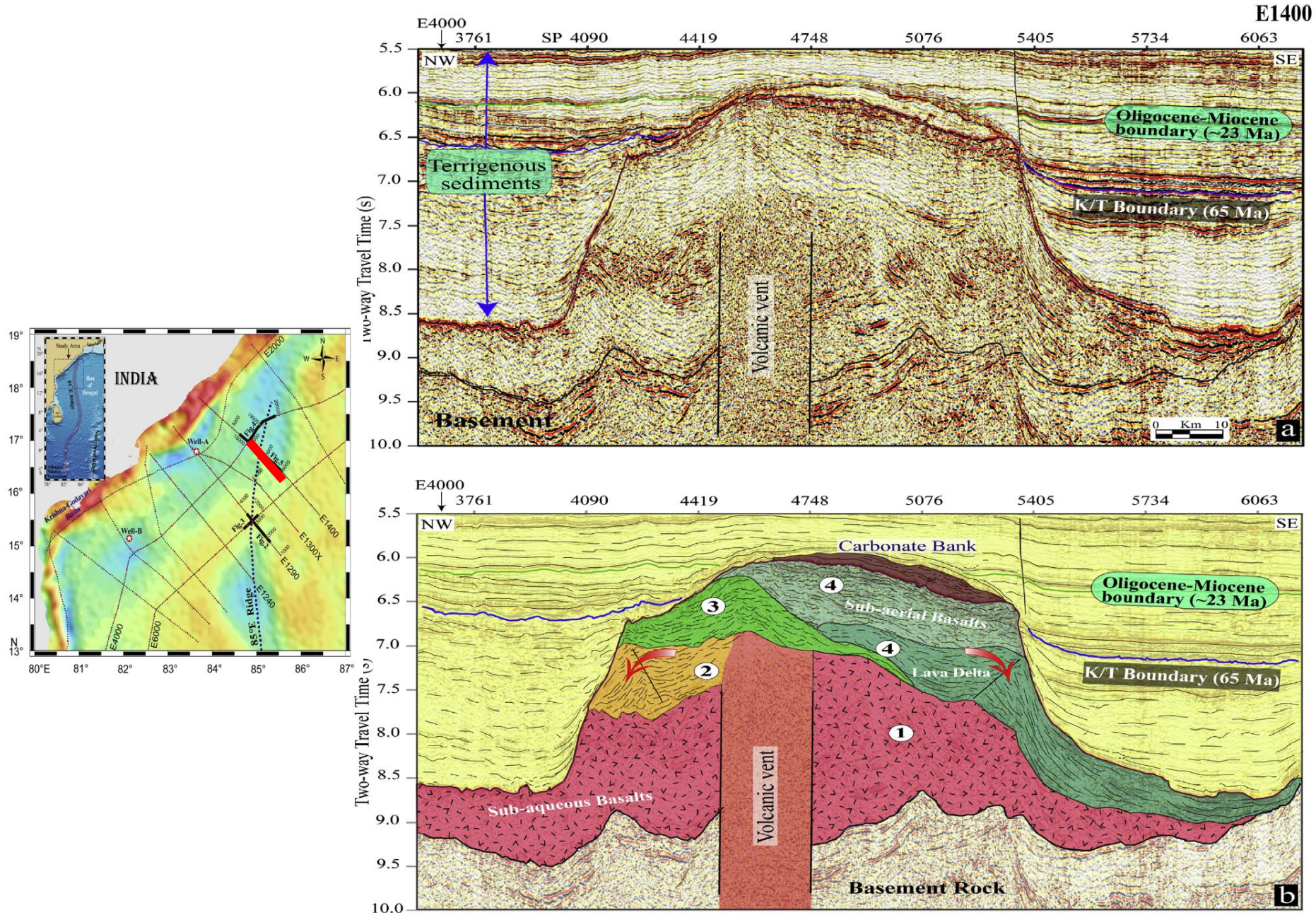

Fig. 5. The coast perpendicular seismic profile E1400 and its interpretation depict the internal structure of the northern segment of the 85°E Ridge.

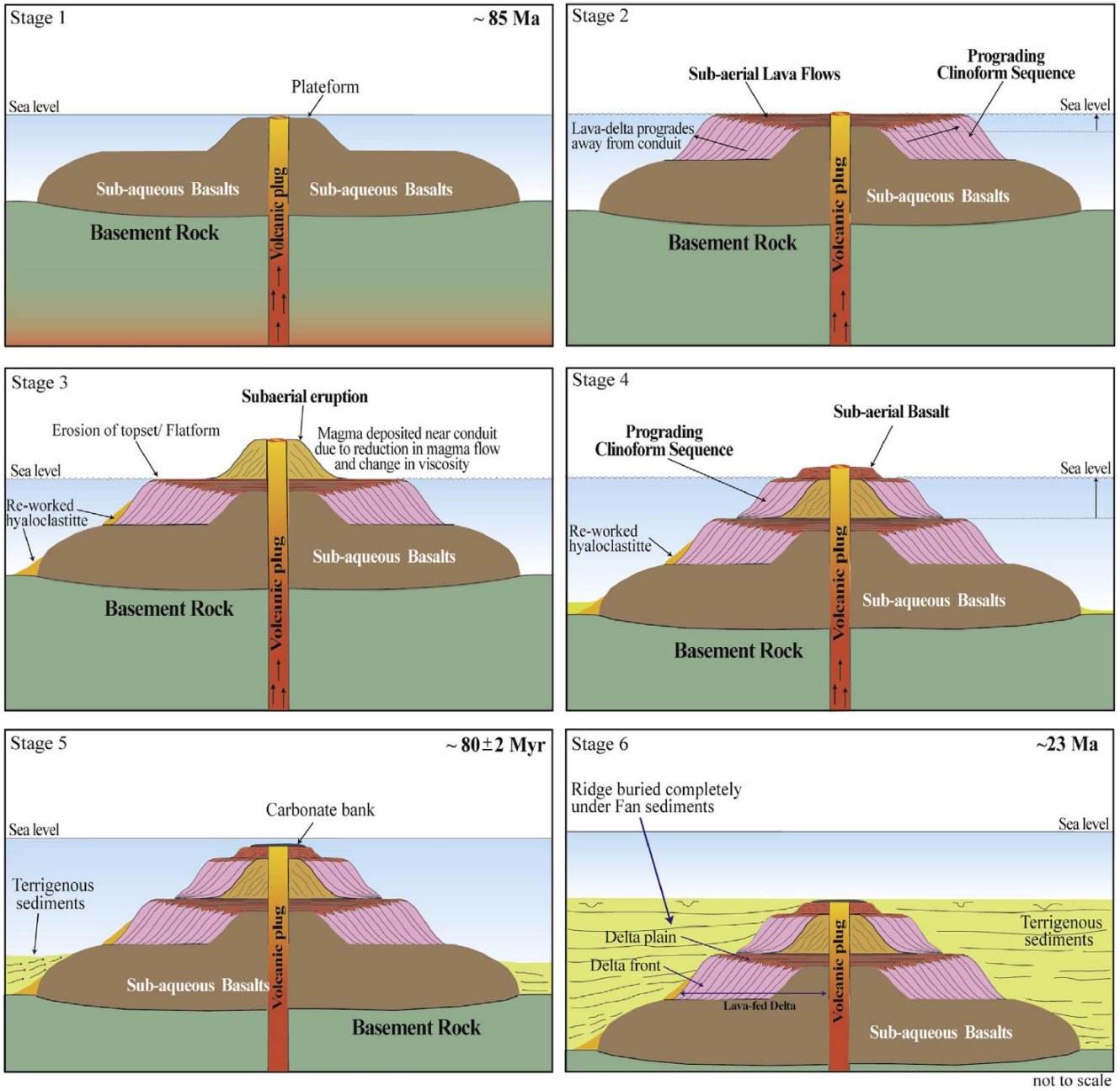

Fig. 6. Schematic illustration showing the development of the 85°E Ridge through geological age.

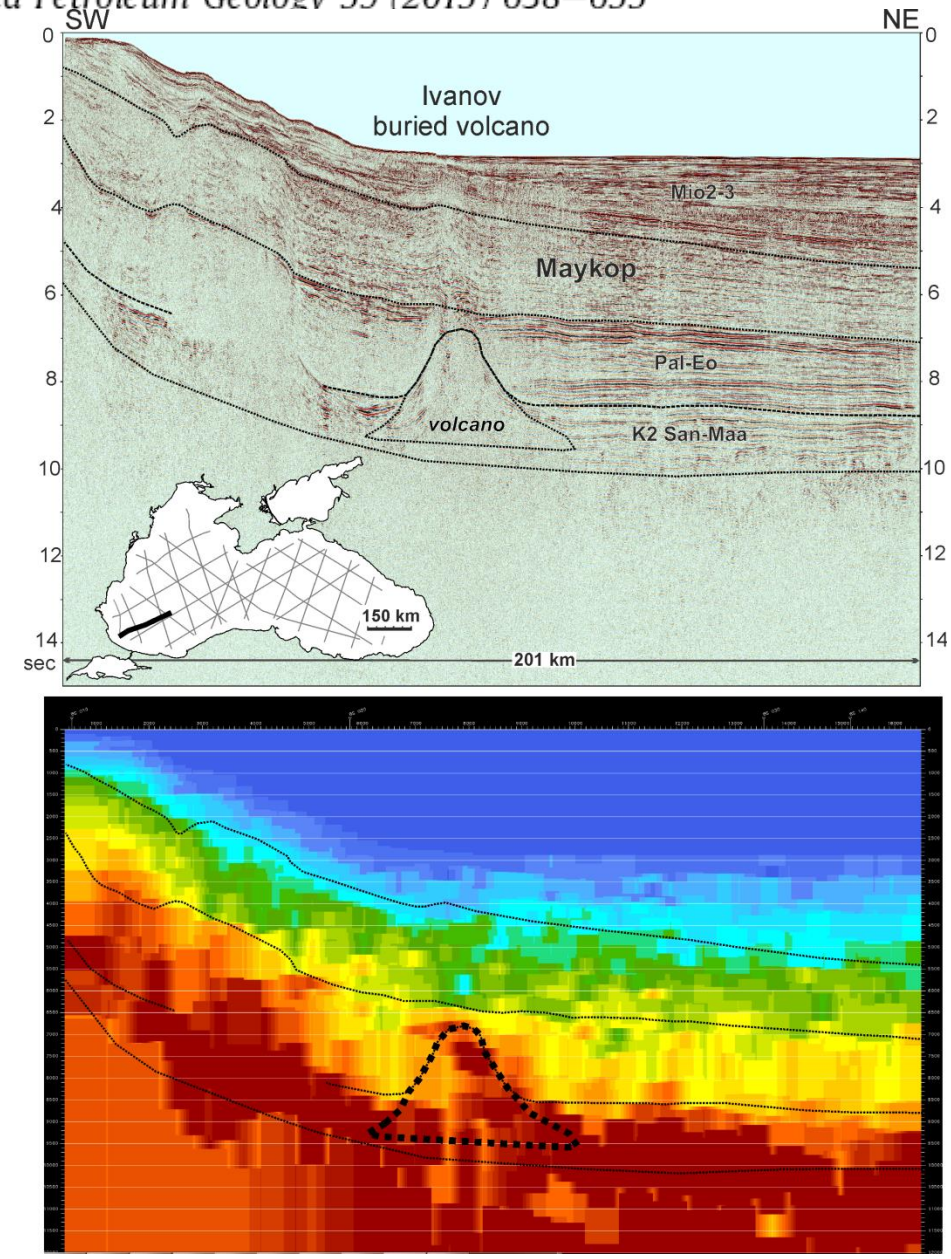

Figure 17. Geological interpretation of seismic line BS-222 (above) and seismic velocities along the same line (below). A sizeable mountain-like feature can be recognized at bottom of the layered sedimentary sequence. This structure has a positive seismic velocity anomaly indicating dense rock origin of the structure; we interpret this feature as a likely Cretaceous volcano. The volcano was not eroded and its height is up to 2.5 s, indicating a Late Cretaceous water depth in excess of 2–3 km. The volcano was buried by sediments later, during the Eocene. This hypothetical volcano is not mud volcano as was proposed by Graham et al. (2013).

Внутриплитный магматизм

Японское море

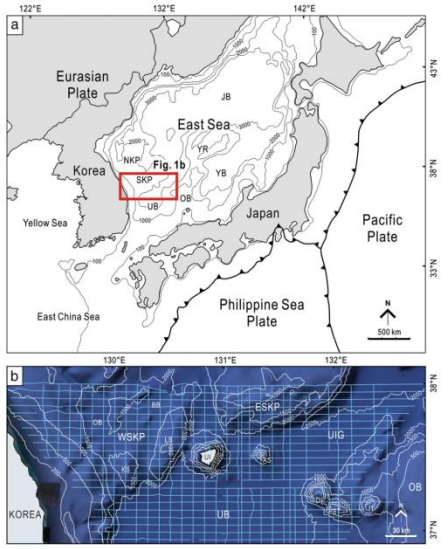

Fig. 1. (a) Physiography of the East Sea, JB, YB, and UB: Japan, Yamato, and Ulleung basins, respectively, YR: Yamato Rise, OB: Oki Bank, NKP and SKP: North a (b) Locality map of the study area. Blue lines represent tracklines of the seismic profiles collected during 2001–2004 from aboard the R/V *Tamhae II*. Bathym and ESKP: Western and Eastern South Korea Plateau, UIG: Ulleung Interplain Gap, UI: Ulleung Is., AS: Anyongbok Seamount, DI: Dok Is., KS: Kimina Seamou Tablemount, IT: Isabu Tablemount.

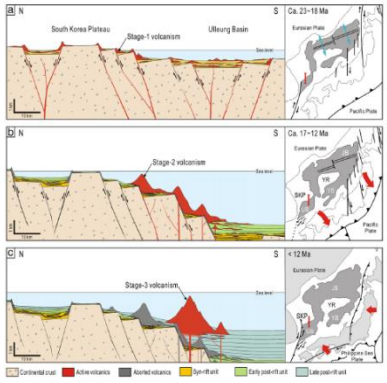

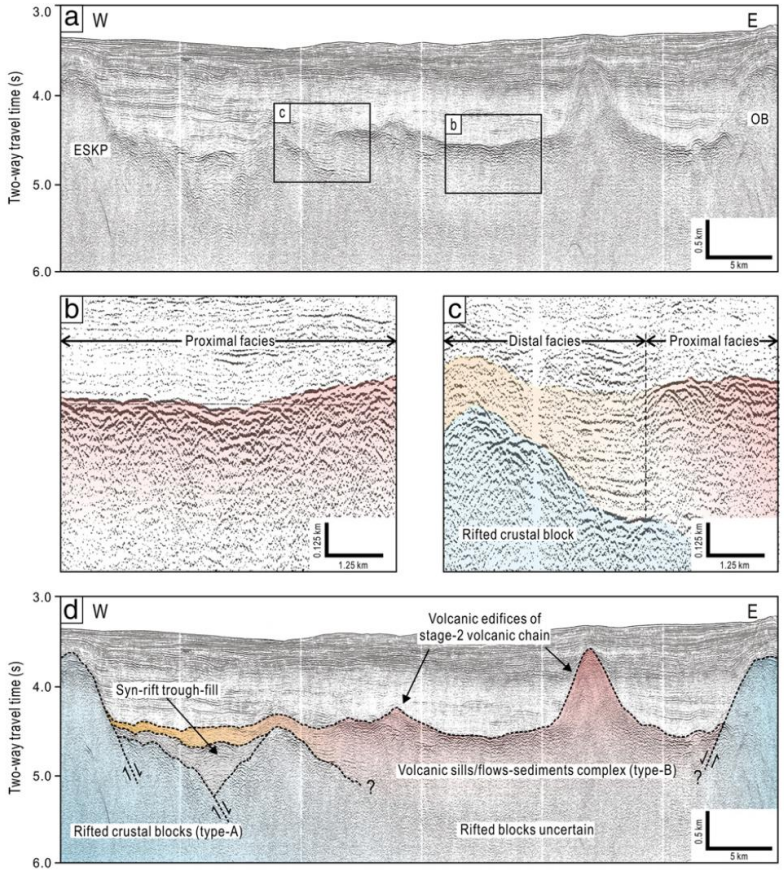

Fig. 6. (a) Selected seismic reflection profile showing overall topography of the UIG (for location, see Fig. 2a). (b) Details of the highly rugged acoustic basement of the UIG. Irregularly overlapping high-amplitude hyperbolae with almost transparent internal reflection configurations occur near the volcanic eruption centers. (c) Details of the crudely stratified seismic reflection facies of acoustic basement identified relatively far from the eruption centers. (d) Details of the acoustic basement types in the UIG. Rifted crustal blocks of the ESKP and OB are bordering on the NW and SE of the UIG. Volcanic edifices are scattered along the eruption center. Underlying rifted blocks are identified in the western boundary of the

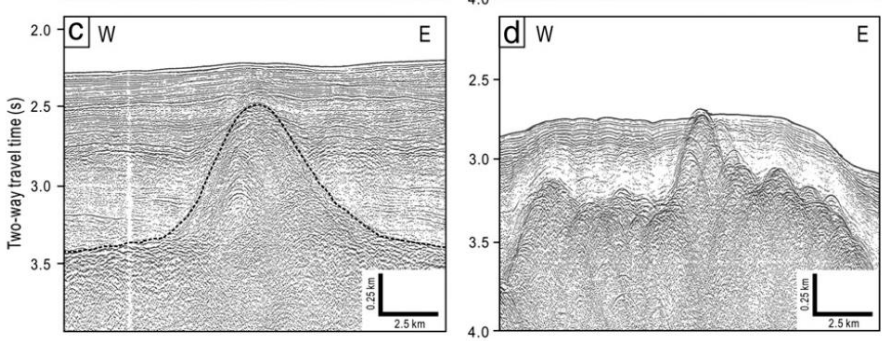

(c) One of the small volcanic cones scattered around the UIG. (d) Volcanic mound which supports small pinnacles with various vertex elevations.

Африка. Шельф Гвинеи

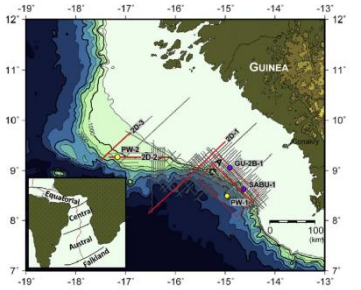

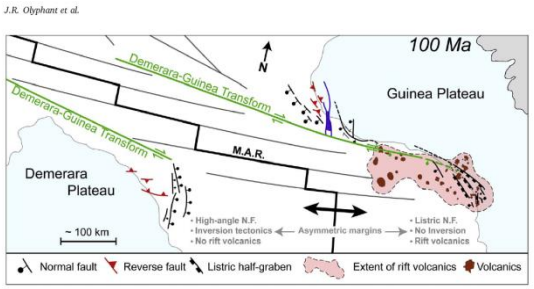

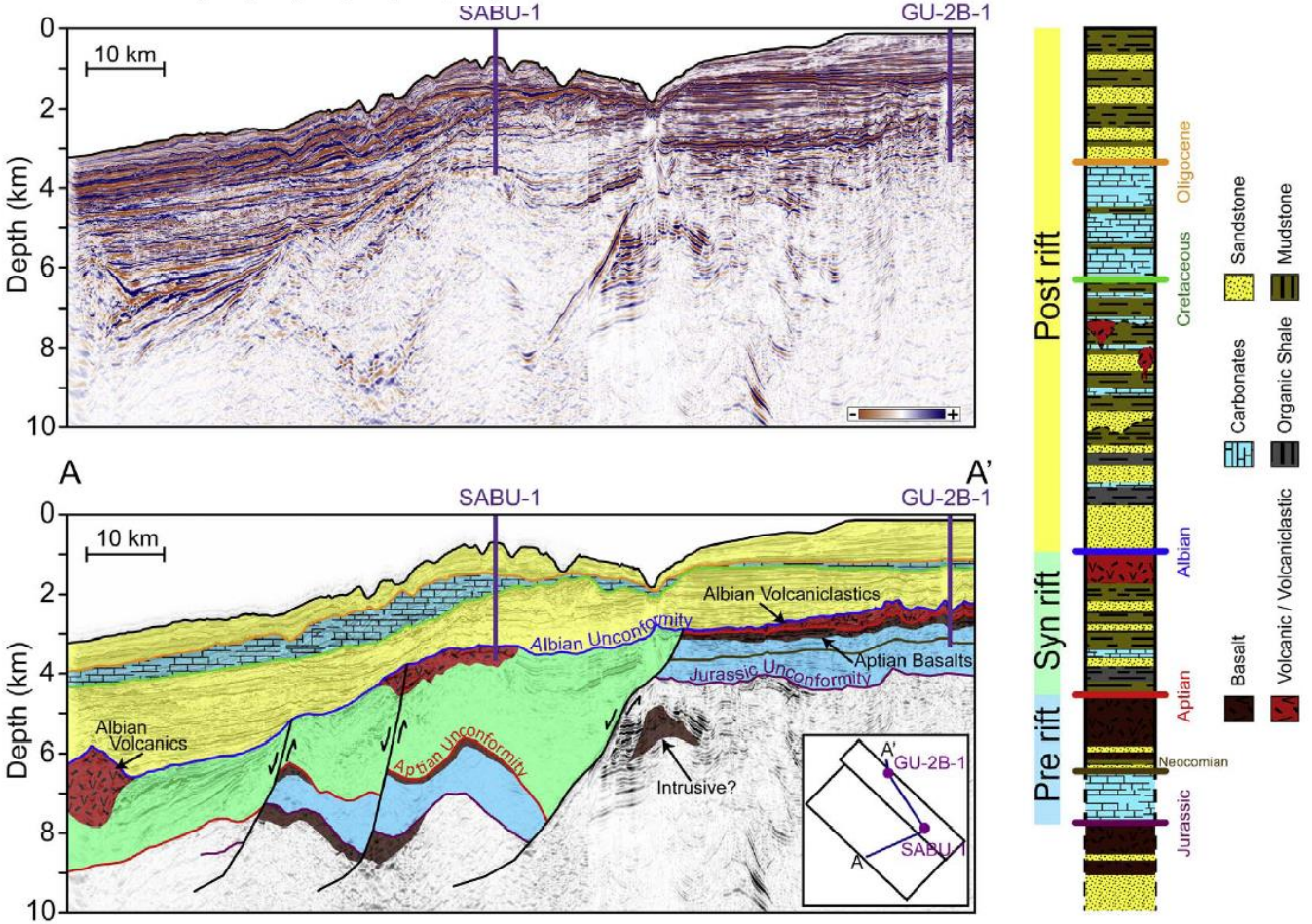

Fig. 2. (Right): Generalized stratigraphic section of the Southern Guinea Plateau based on seismic and well data. (Left) Arbitrary seismic profile taken through both 3-D surveys. Naming convention of rift-timing in relation to stratigraphic section is shown to the left of the stratigraphic column. Unless explicitly stated elsewhere, pre-rift strata refer to all strata deposited prior to the Cretaceous rifting event. The Jurassic, Aptian, Albian, Cretaceous, and Oligocene horizons are typically manifested as unconformities, while the Neocomian (brown) is a conformable horizon representing the top of Neocomian carbonates. (For interpretation of the references to color in this figure legend, the reader is referred to the web version of this article.)

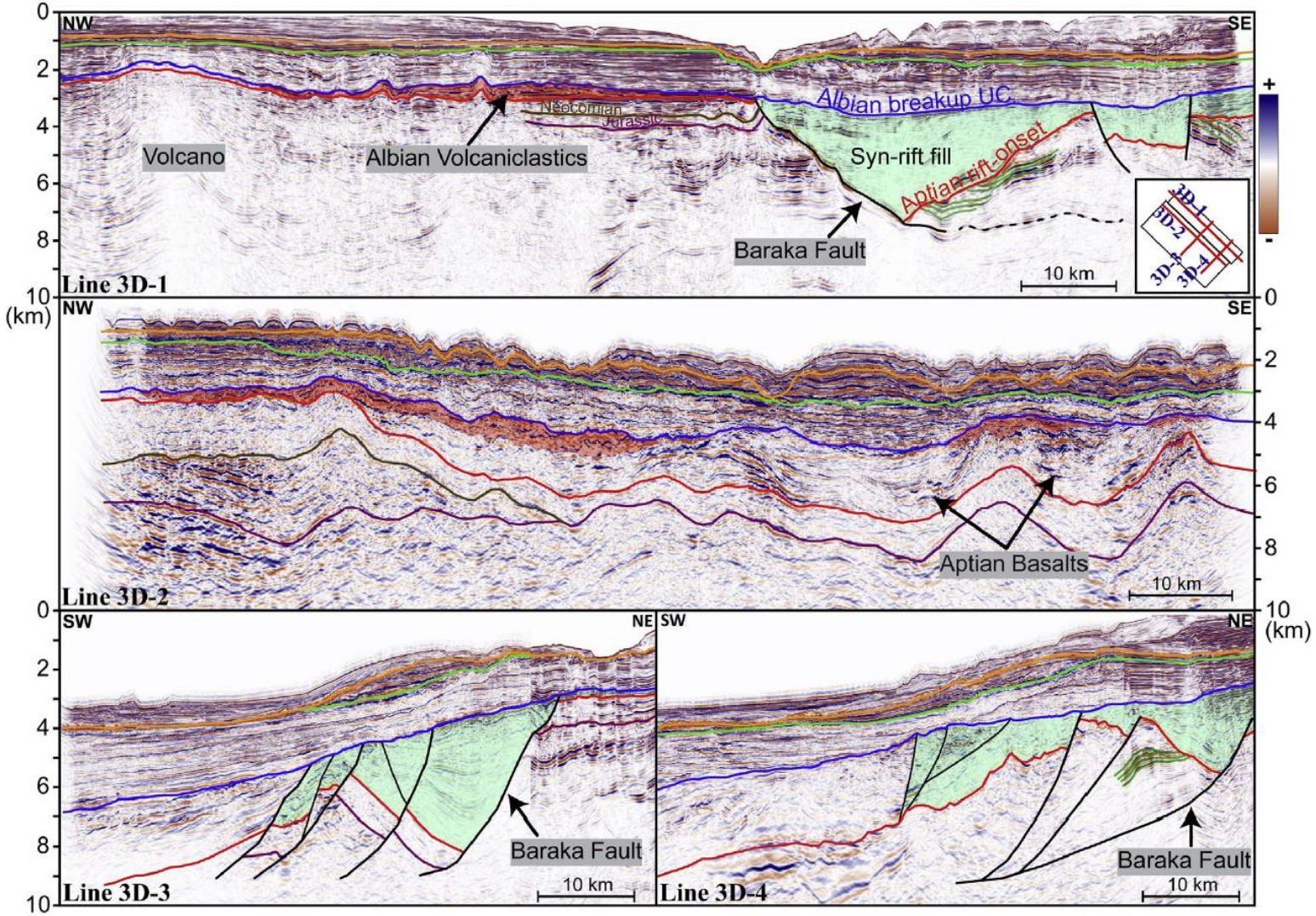

Fig. 3. Four interpreted seismic profiles from the 3-D surveys, A & C. Inset map of line locations shown in bottom-right corner of Line 3D-1. Lines 3D-1 and 3D-2 are inlines oriented roughly parallel to the strike of the shelf margin. Lines 3D-3 and 3D-4 are crosslines that provide a dip-direction perspective of the continental shelf-slope-rise margin. Horizon/unconformity colors are consistent with the stratigraphy presented in Fig. 2. The semi-transparent green lines beneath the Aptian ROU in Lines 3D-1 and 3D-4 highlight the top-lapping angular unconformity characteristic of rift-onset unconformities (Franke, 2013). The red-shaded polygons represent interpreted Albian volcanics. (For interpretation of the references to color in this figure legend, the reader is referred to the web version of this article.)

Район Австралии

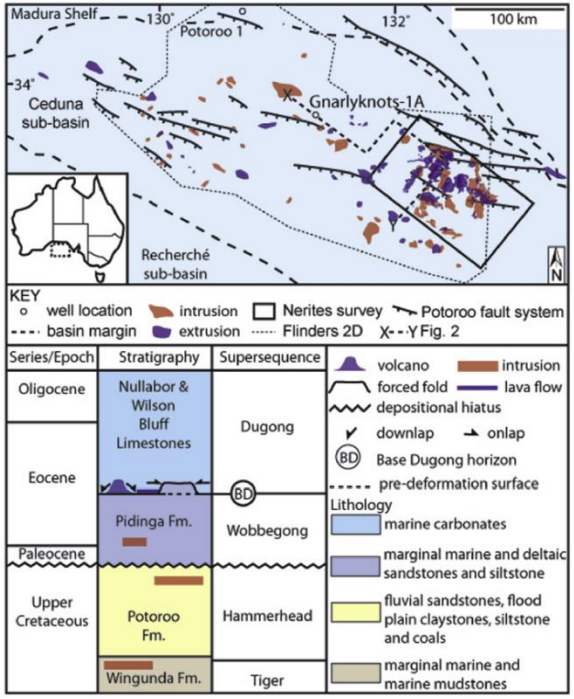

Fig. 1. Map showing the location of the study area along the southern Australian margin and a stratigraphic column indicating that the intrusions are of Mid Eocene age.

P. Reynolds et al. / Marine and Petroleum Geology 88 (2017) 605–616

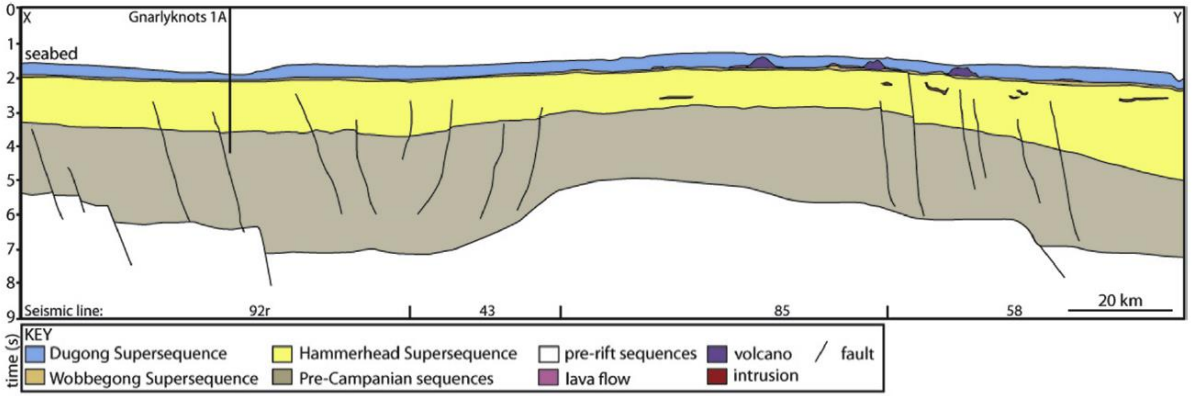

Fig. 2. Composite seismic section using lines 43, 58, 85 and 92r from the Flinders 2D seismic survey. Uninterpreted version provided in Supplementary Data (Fig. S1).

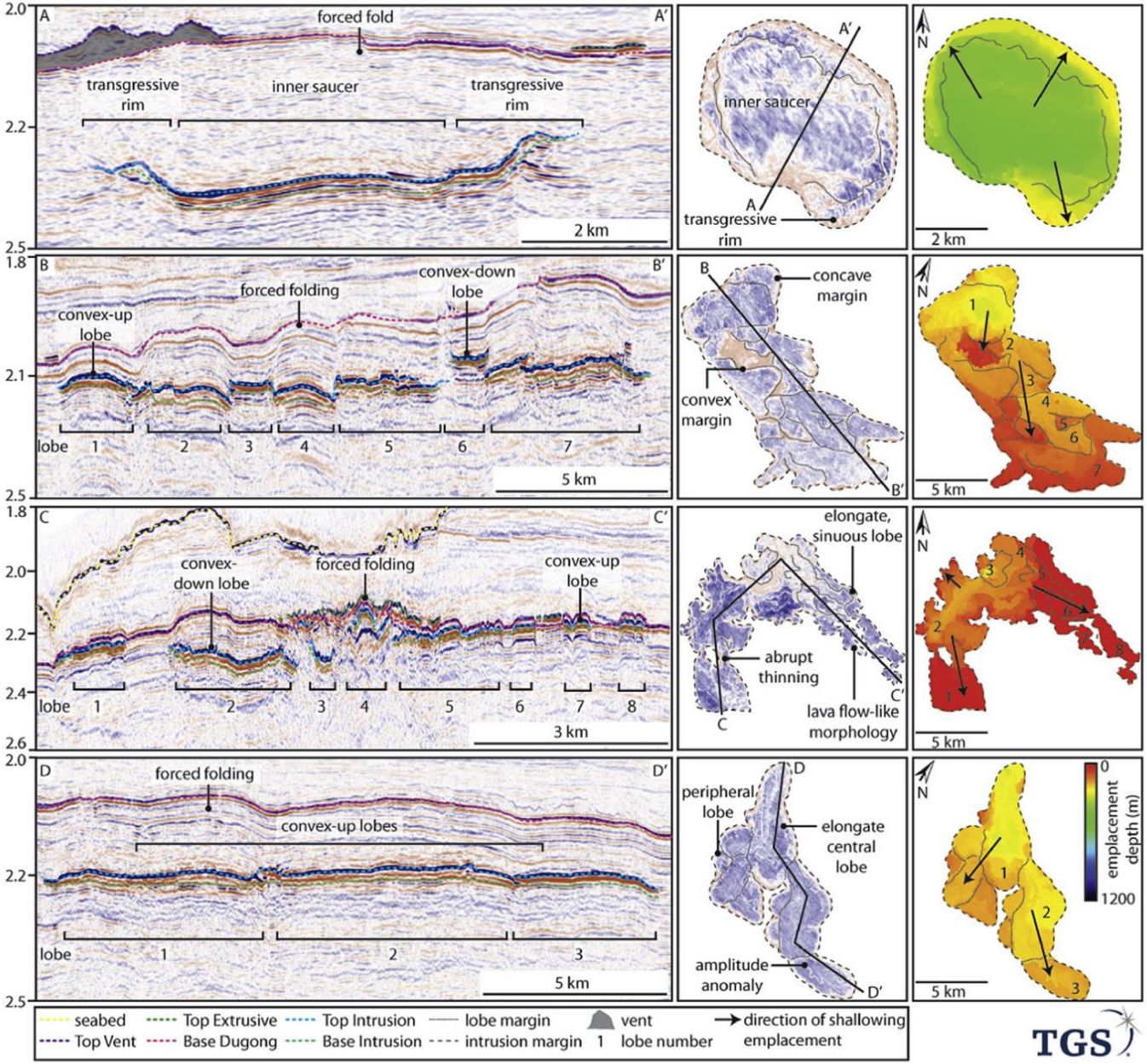

Fig. 3. Seismic cross sections through intrusion number S13, a saucer-shaped sill (A); intrusion number C27, a compound sill (B); intrusion number H36, hybrid sill (C) and intrusion number L4; a laccolith (D). Emplacement depth and amplitude maps are also shown. See Fig. 4 for their locations.

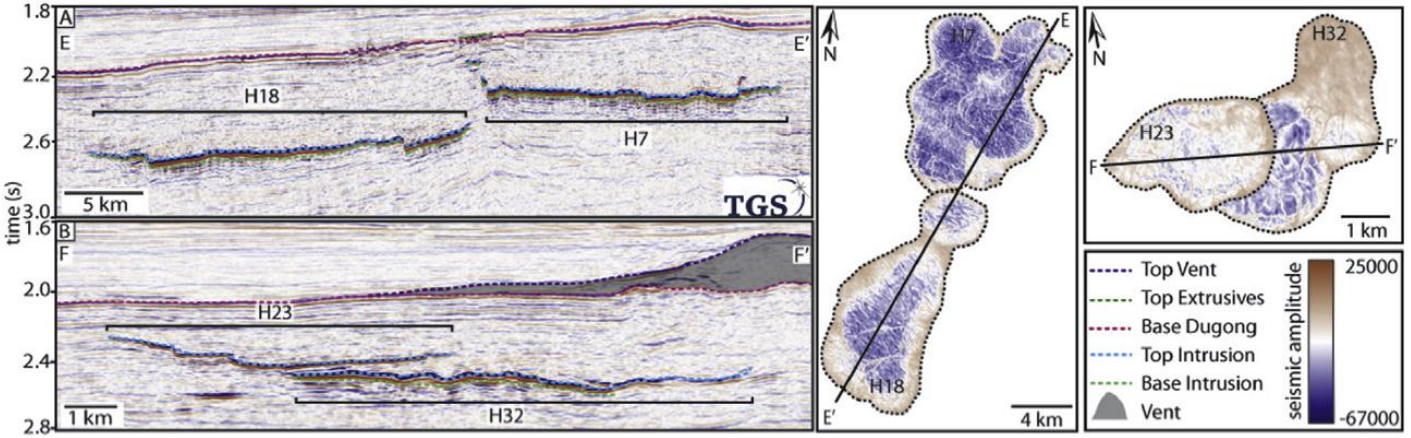

Fig. 7. Seismic cross sections of sills 7 and 18 (A) and 23 and 32 (B). In A, the intrusions overlap but are not connected. These intrusions are typical of those within the Ceduna Sub-basin. In the B the sills form a complex, perhaps allowing lateral and vertical transport of magma.

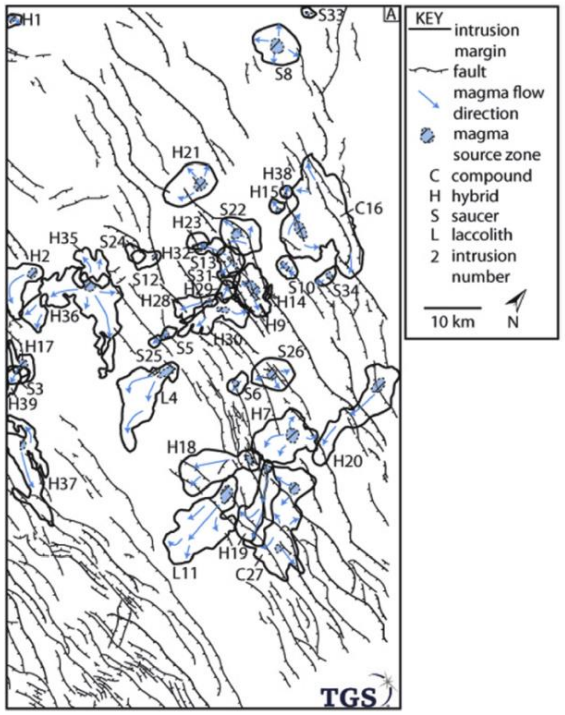

Fig. 8. Map showing the direction of magma flow within the intrusions and their source regions.

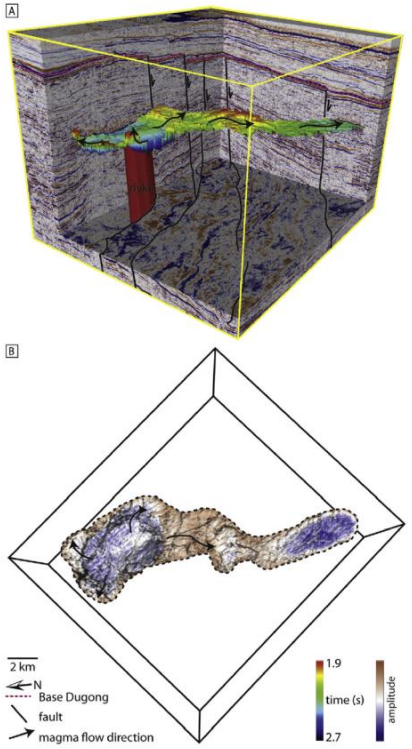

Fig. 9. 3D visualisation of a hybrid sill (number H20) showing time (A) and amplitude (B) maps and interpreted magma flow directions. The intrusion overlies a fault and is interpreted to have been fed by a dyke. See Fig. 8 for location.

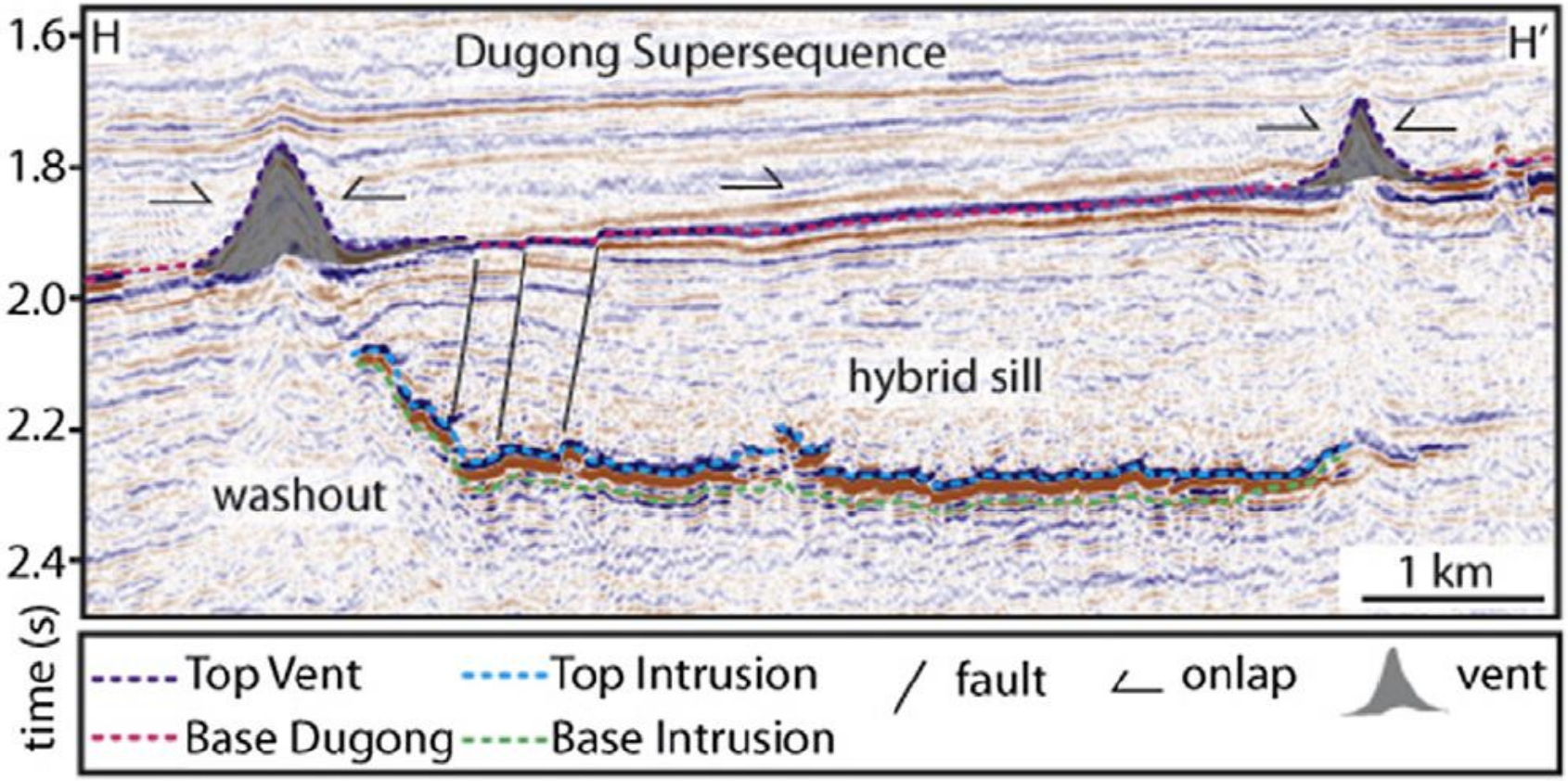

Fig. 12. Seismic section showing a saucer-shape sill and volcanogenic vents. The left-most vent is located above the shallowest termination of the sill ~200 m beneath the paleosurface. See Fig. 10 for location.

Южно-Китайское море

Igneous features	Geometry	Description	Interpretation
Concordant, high-amplitude reflection		Amplitude anomalies with distinct lateral extent and sharp edges	Sill
Bowl-shaped, high-amplitude reflection		A narrow bowa-shaped geometry with a rough seismic character	Sill
Saucer-shaped, high-amplitude reflection		A saucer-shaped geometry with a rough seismic character	Sill
Vertical intrusive		Narrow, tall, upright seismic dead zone; upturned host rock and uplifted overburden	Stock
Top-of-basement complex		Consisting of irregular mounds and peaks formed on top of basement	Volcanic edifices and/or necks
Vertical eruption		Eruption from seafloor/land	Seamount/Volcano

Fig. 2. Igneous features, geometry, description, and interpretation of the igneous complexes (Modified from Lee et al., 2006).

X. Song et al. Marine Geology xxx (xxxx) xxx–xxx

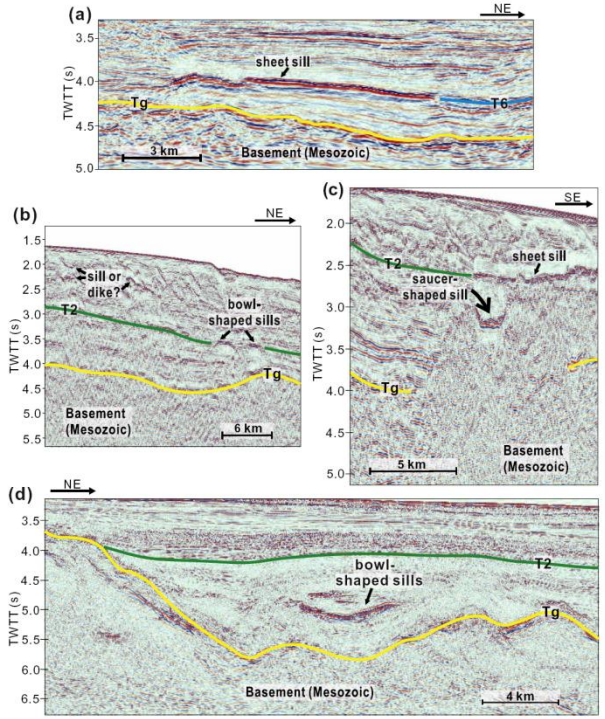

Fig. 5. (a) Concordant sill shown on a seismic reflection profile. (b), (c) and (d) are seismic reflections of saucer- or cup-shaped sills. T2: ~5.3 Ma; T6: ~23 Ma; Tg: top basement. TWTT: two way travel time. See Fig. 1 for location.

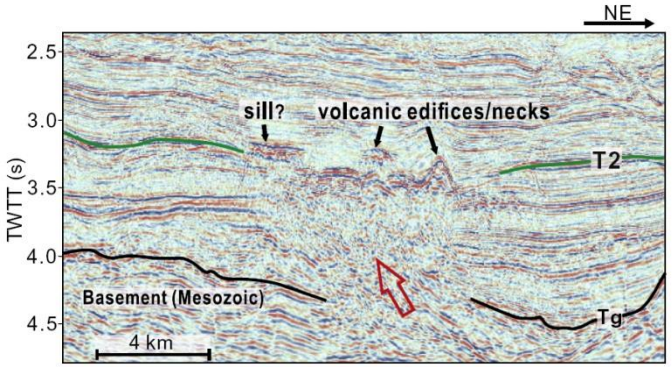

Fig. 7. Volcanic edifices/necks shown on a seismic reflection profile. The red arrow shows the migration path of magma. T2: ~5.3 Ma; Tg: top basement; TWTT: two way travel time. See Fig. 1 for location. (For interpretation of the references to colour in this figure legend, the reader is referred to the web version of this article.)

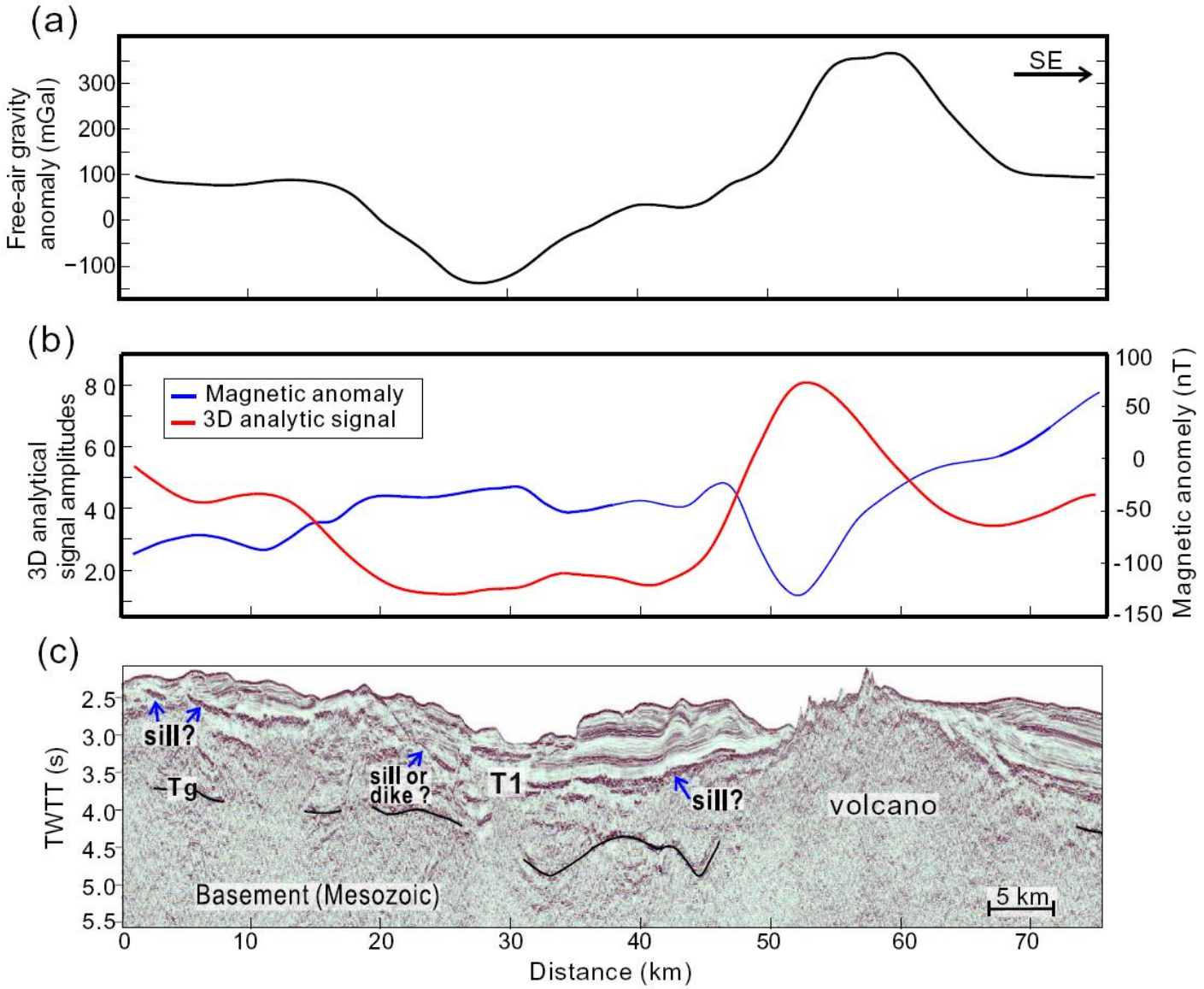

Fig. 9. An example of gravity and magnetic characteristics of igneous bodies. T1: ~2.6 Ma; Tg: top basement; TWTT: two way travel time. See Fig. 1 for location.

Южно-Китайское море

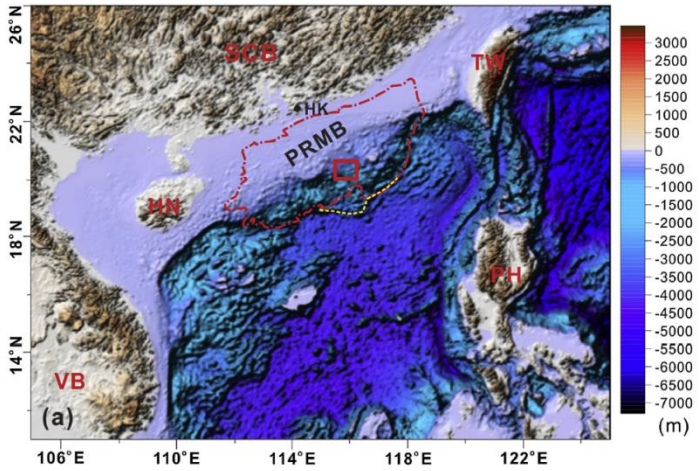

Q. Sun et al. / Marine and Petroleum Geology 54 (2014) 83–95

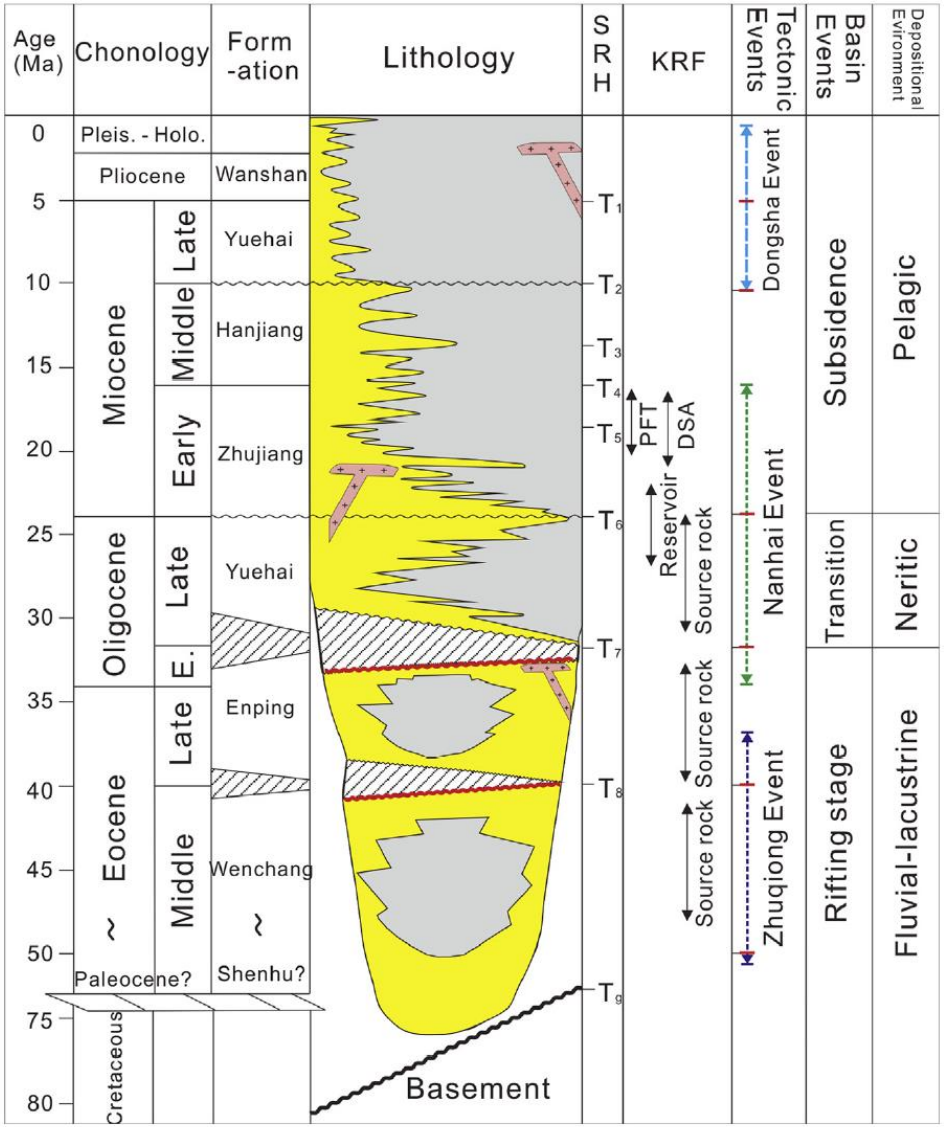

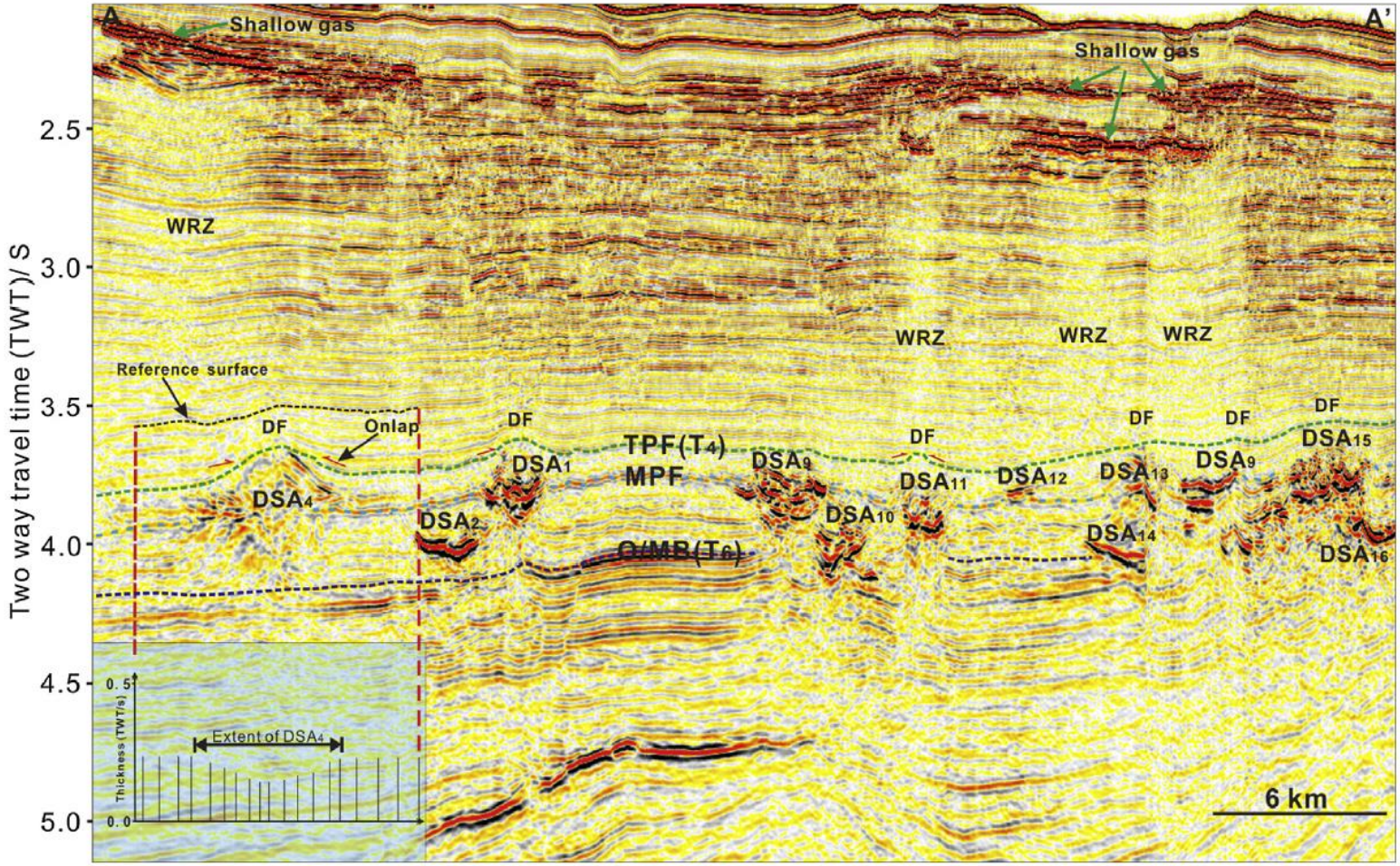

Figure 4. Representative 3D seismic profile of the study area. Discordant seismic anomaly (DSA), domal structure (DF), weak/blanking reflection zone (WRZ) and shallow gas are labelled. The discordant seismic anomalies are subdivided into two levels. The first level (e.g. DSA_1 and DSA_{11}) has its axis approximately along the MPF (middle of polygonal fault tier, blue dashed line) where the polygonal faults have their largest throws and shows positive reliefs at the surface of TPF (top of polygonal fault tier, green dashed line); the second level (e.g. DSA_2 and DSA_{10}) is just below the first and does not show topographic expression at the TPF marker. O/MB = Oligocene/Miocene boundary. Note the insert in the left bottom shows the thinning of overlain sediments of DSA_4 between surfaces TPF and the reference surface. The lateral scale is same with this bounded between the two red dashed lines. (For interpretation of the references to colour in this figure legend, the reader is referred to the web version of this article.)

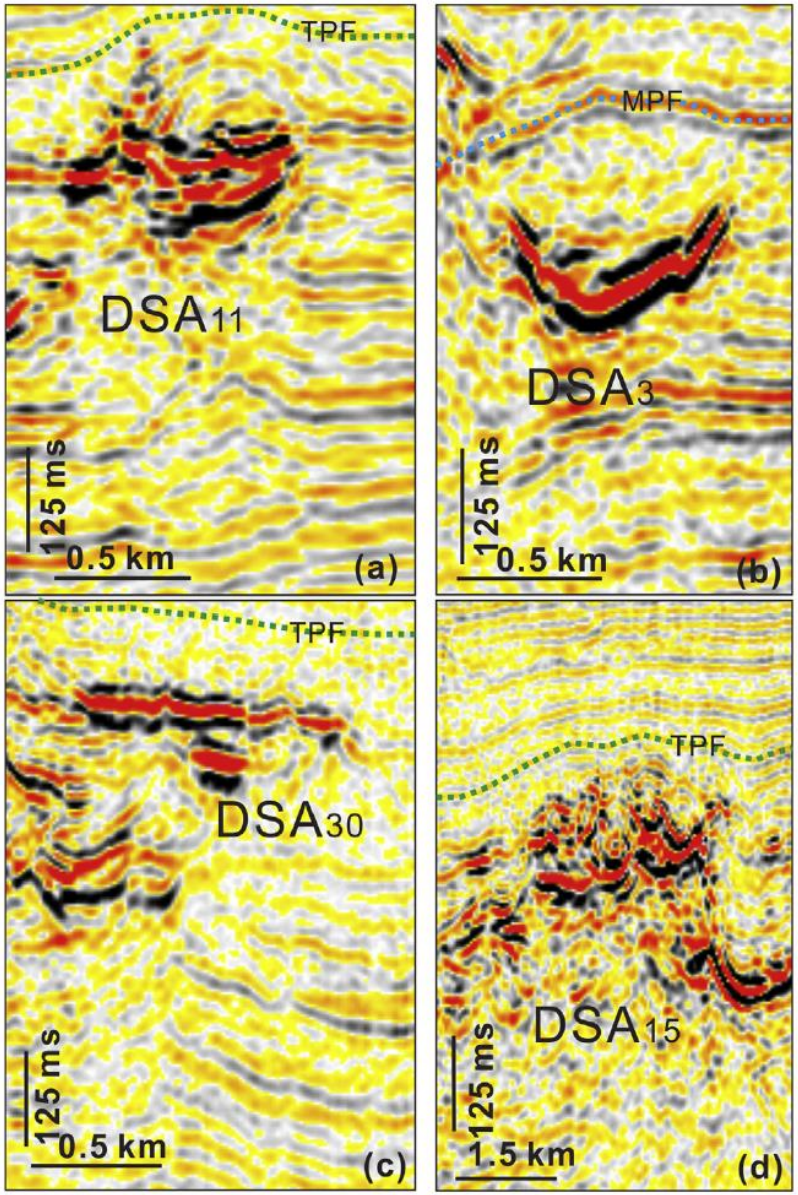

Figure 5. Four categories of discordant seismic anomalies. (a): lensoid-shaped seismic anomaly (DSA_{11}); (b): saucer-shaped seismic anomaly (DSA_3); (c): stacked seismic anomaly (DSA_{30}); (d): composite seismic anomaly (DSA_{15}). The key horizons are: TPF (Top of Polygonal Fault Tier or Early/Middle Miocene Boundary) and MPF (Middle of Polygonal Fault Tier).

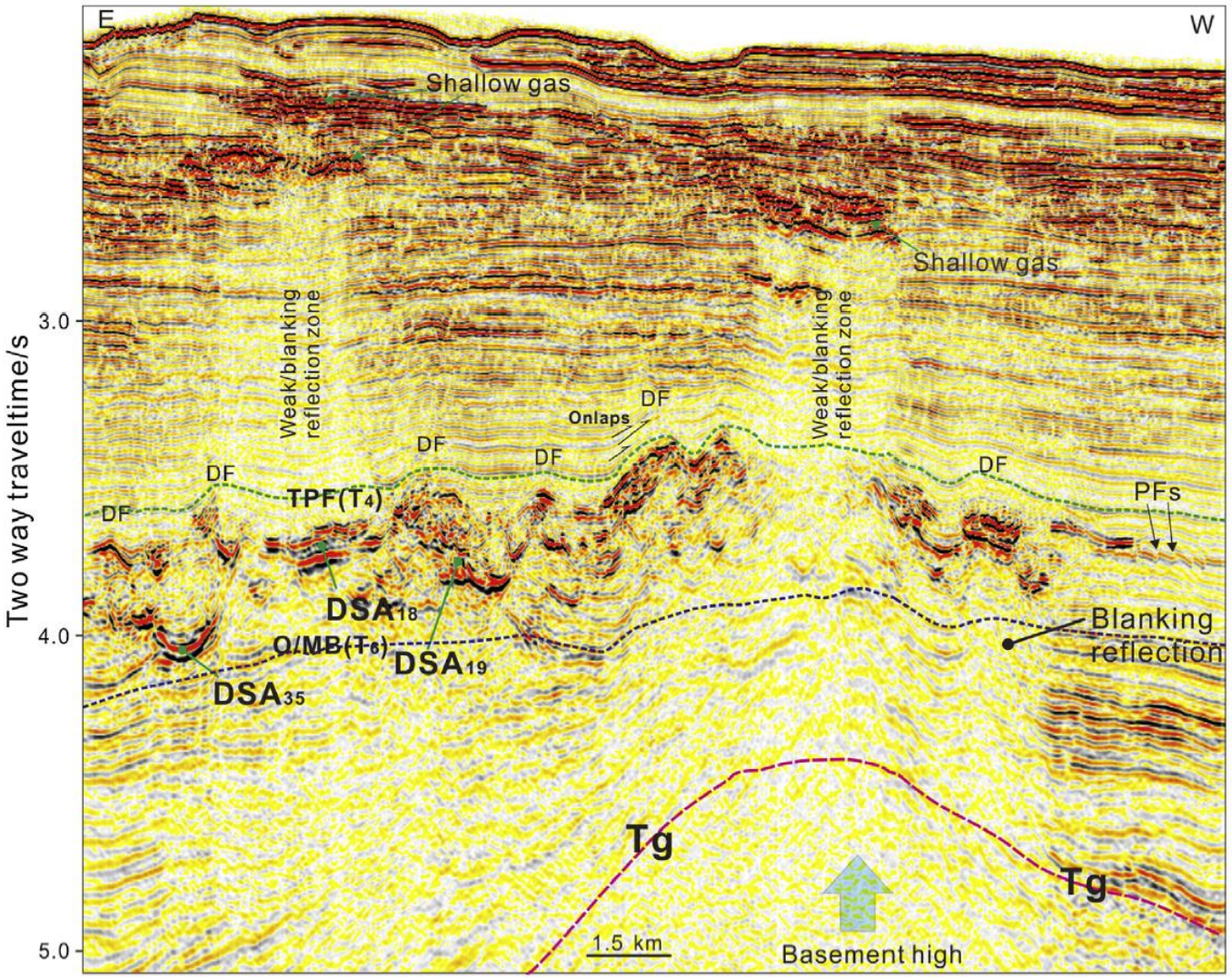

Figure 6. Representative 3D seismic profile of discordant seismic anomalies. The discordant anomalies become complex towards to the basement high. Weak/blanking reflection zones (WRZs), shallow gases, 'saucer'-shaped anomaly (DSA_{35}), stacked anomaly (DSA_{18}), composite anomaly (DSA_{19}) and polygonal faults are labelled. O/MB = Oligocene/Miocene boundary.

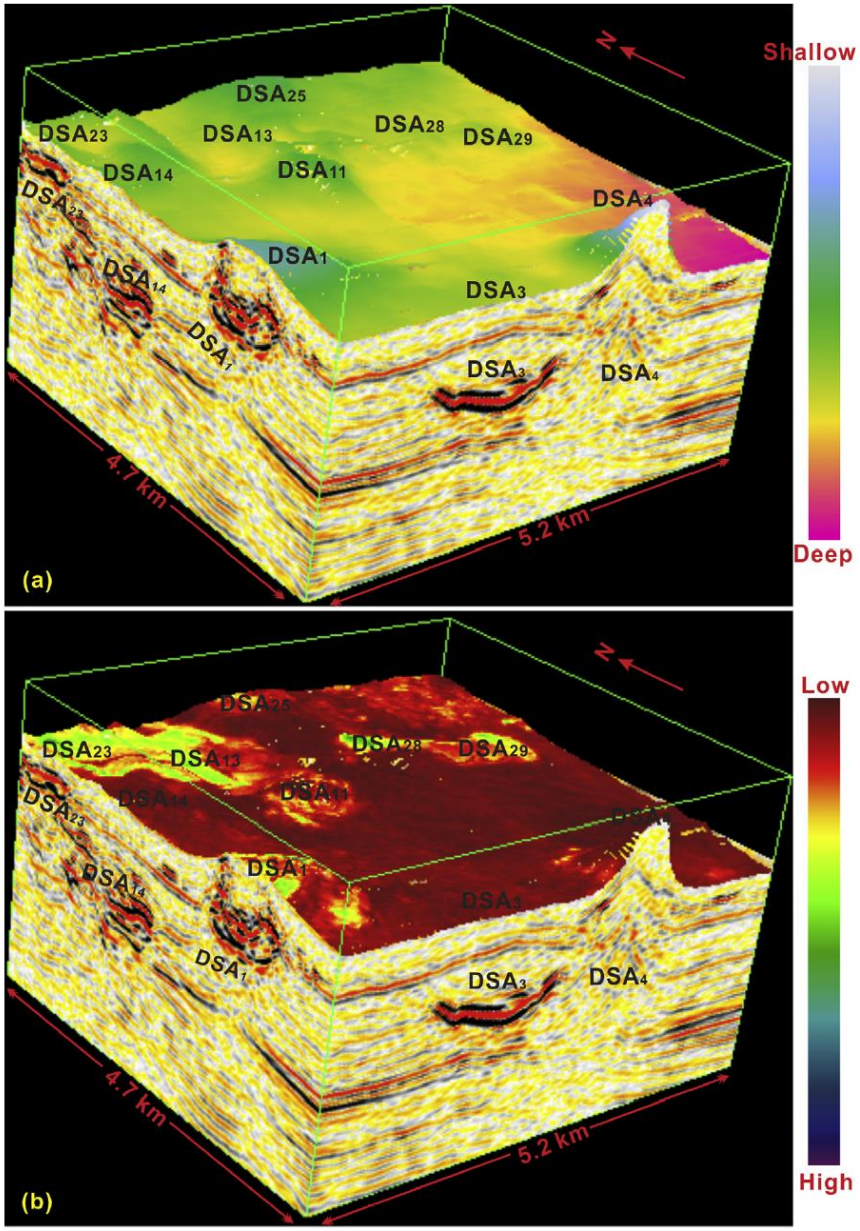

Figure 9. (a) Three dimensional visualization of the seismic volume superimposed with the surface of top of polygonal fault tier (TPF). The positive reliefs indicate the occurrence of discordant seismic anomalies (DSAs) below. (b) Three dimensional visualization of seismic volume superimposed with RMS amplitude attribute windowed 200 ms below the TPF. The RMS amplitude attribute of discordant seismic anomalies have a positive relationship with the topographic reliefs of the TPF.

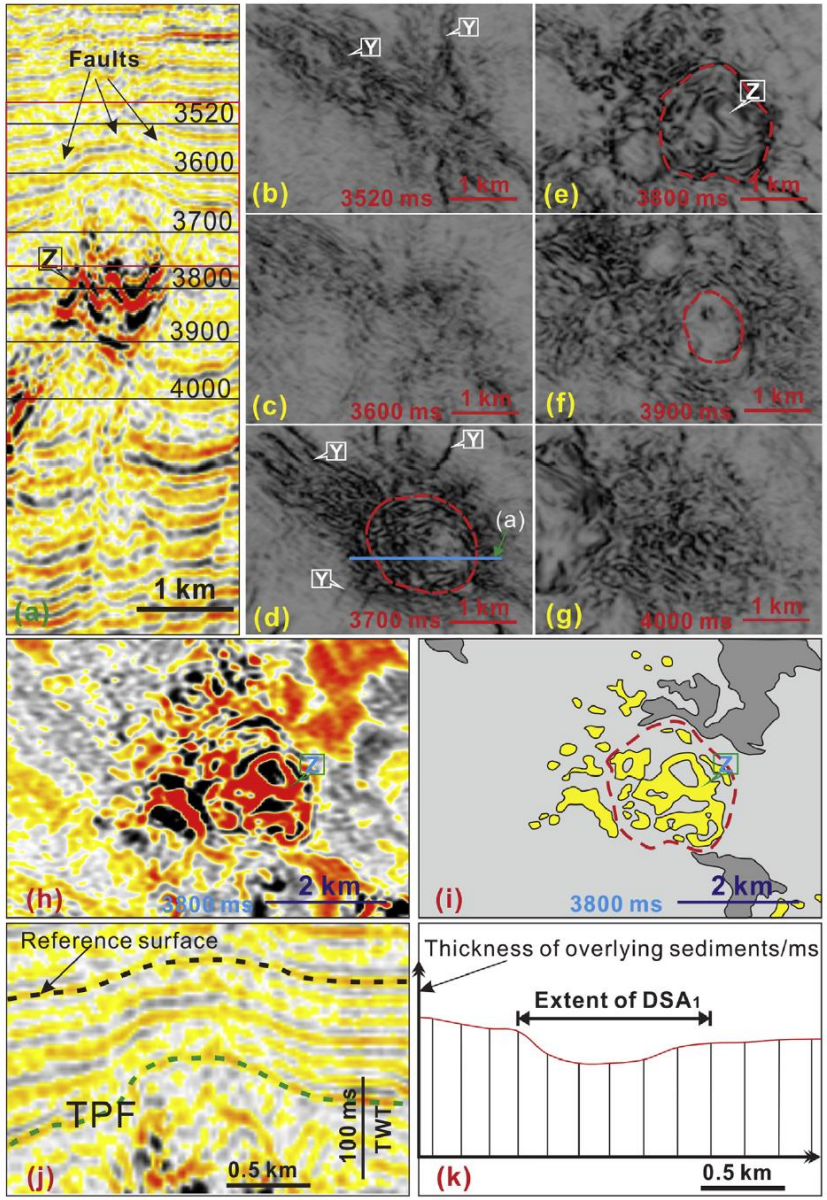

Figure 10. The characteristics of lensoid-shaped discordant seismic anomaly (DSA_1). (a) Representative seismic profile. Faults and block-like structure (marked Z) are labelled; (b)–(g): coherence slices through the lensoid-shaped anomaly. Red dashed line is the boundary of the lensoid-shaped discordant seismic anomaly, Y = radial faults, Z = intrusive block; (h) and (i): time slice at 3800 ms and line drawing interpretation; (j): the amplification of the area in red square in (a) shows the folded strata become thinner toward to the forced fold; (k) shows the variable thickness between the surface of TPF and reference surface. (For interpretation of the references to colour in this figure legend, the reader is referred to the web version of this article.)

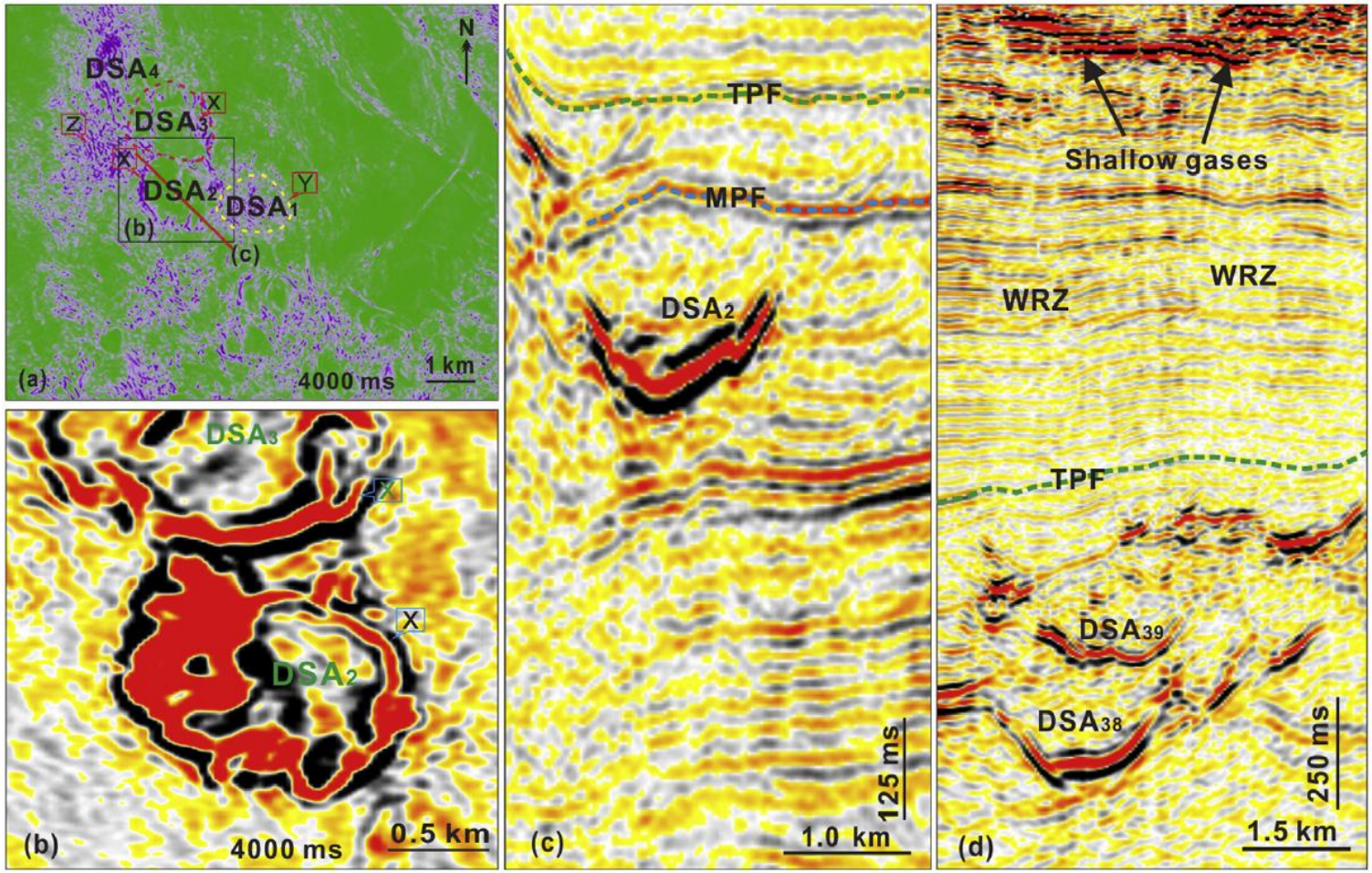

Figure 11. Representative characteristics of 'saucer'-shaped seismic anomalies. (a) Coherence slice at 4000 ms (TWT), showing saucer-shaped discordant seismic anomalies DSA_2 and DSA_3 are nearly circular. Zones of chaotic reflections are indicated with letter Z. (b) Time slice at 4000 m showing the circular shape of discordant seismic anomalies DSA_2 and DSA_3 (marked X); (c) Representative seismic profile through DSA_2 (marked X). WRZ = weak reflection zone; TPF = top of polygonal fault tier; location in (a); (d) Representative seismic profile through DSA_{38} and DSA_{39}.

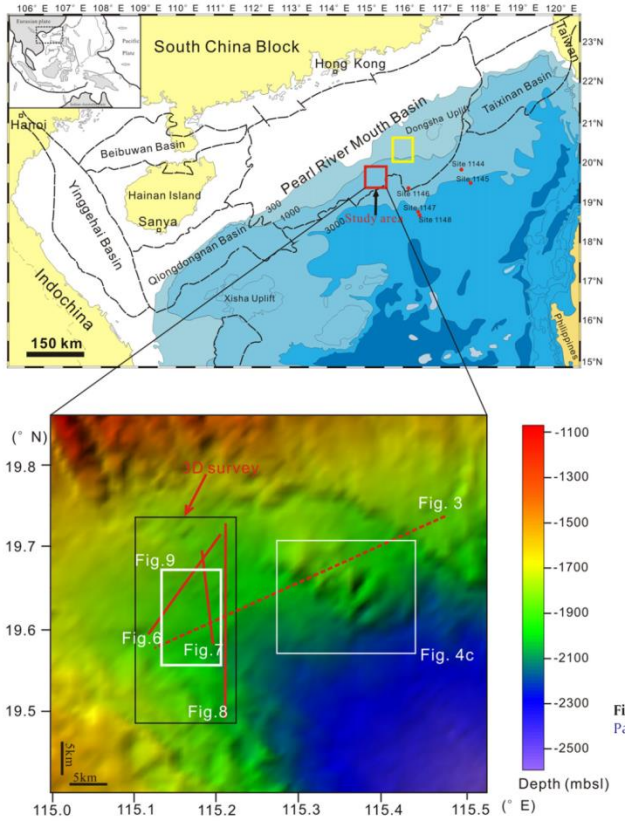

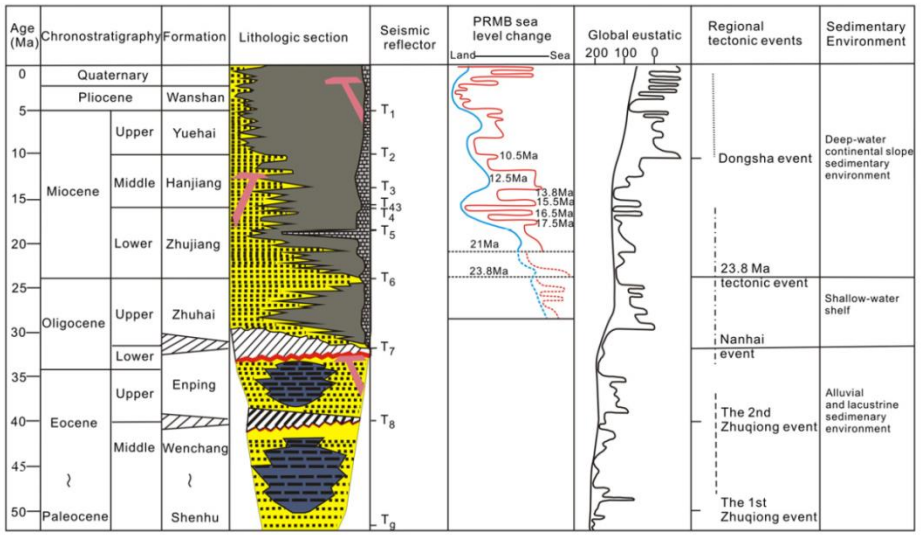

Fig. 2. Schematic stratigraphic column of the Baiyun Sag in the Pearl River Mouth Basin showing lithostratigraphy, sea level variation, tectonic event and sedimentary environment (after Pang et al., 2008). The mounds occur between sequences T_5 and T_2.

Fig. 1. (A) The location of the study area and sedimentary basins in the northern South China Sea. Inset (top left): regional geological setting (after Sun et al., 2012). The yellow rectangle shows the location of Sun et al.'s (2014) study area; (B) Multi-beam bathymetry image of the study area showing water depth and the details of the seismic surveys used in this study. The 3D seismic survey is outlined by the black rectangle. The red dotted line and red solid lines indicate the locations of 2D seismic line and 3D seismic lines, respectively. The right white outline shows the location of a 3D visualization section. mbsl, meters below sea-level.

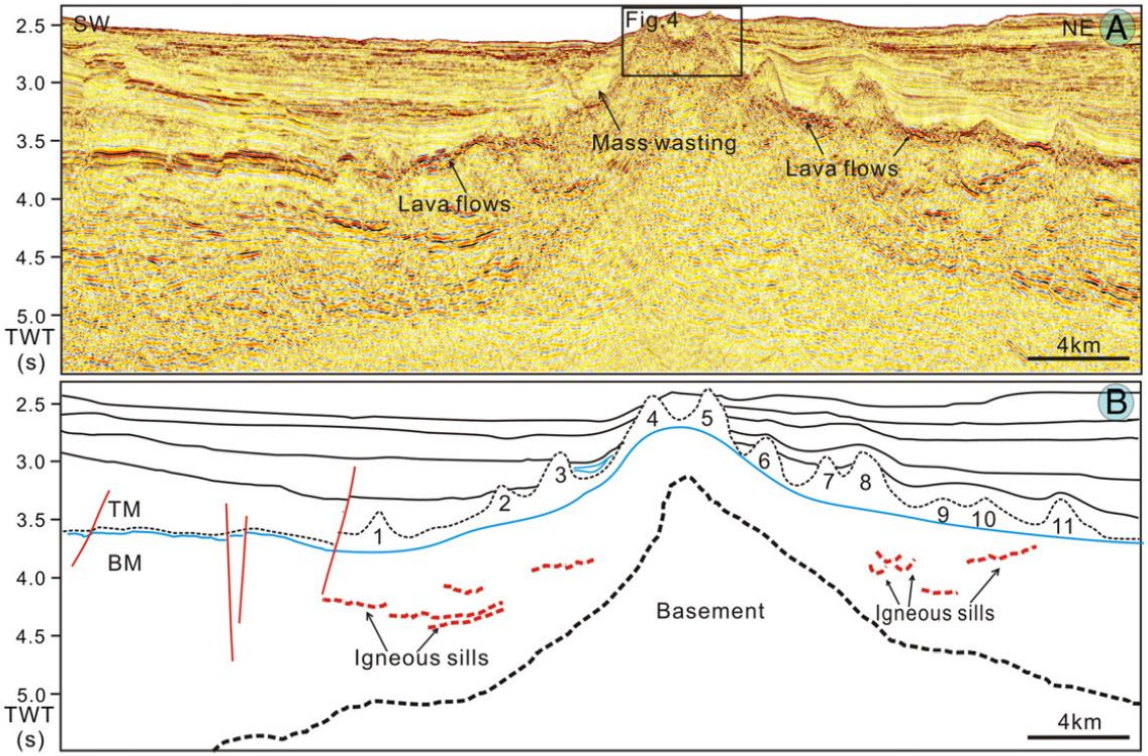

Fig. 3. Regional SW–NE trending 2D seismic line and interpretational sketch illustrating the spatial and stratigraphic relationship between the intrusive and extrusive component; the section presents 11 magmatic mounds and associated structures include igneous sills, lava flows and compaction folds. The single mounds (1–11) form part of a "composite" mound complex. Two mapped seismic surfaces (TM and BM) are indicated. Mound 4 and mound 5 protruded above the seabed and form seamounts. Detailed descriptions are shown in Fig. 4. TM, top mound reflection; BM, base mound reflection. See location in Fig. 1.

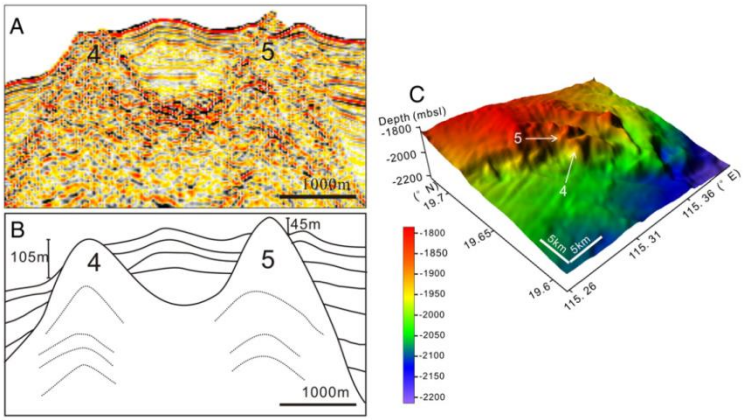

Fig. 4. (A) Enlargement map of the black square in Fig. 3. (B) Schematic illustration of (A). The heights of mound 4 and mound 5 above seabed are 105 m and 45 m, respectively. (C) Multibeam bathymetric map of mound 4 and mound 5; see location in Fig. 1B. The mounds are clearly shown on the map. See location in Fig. 1.

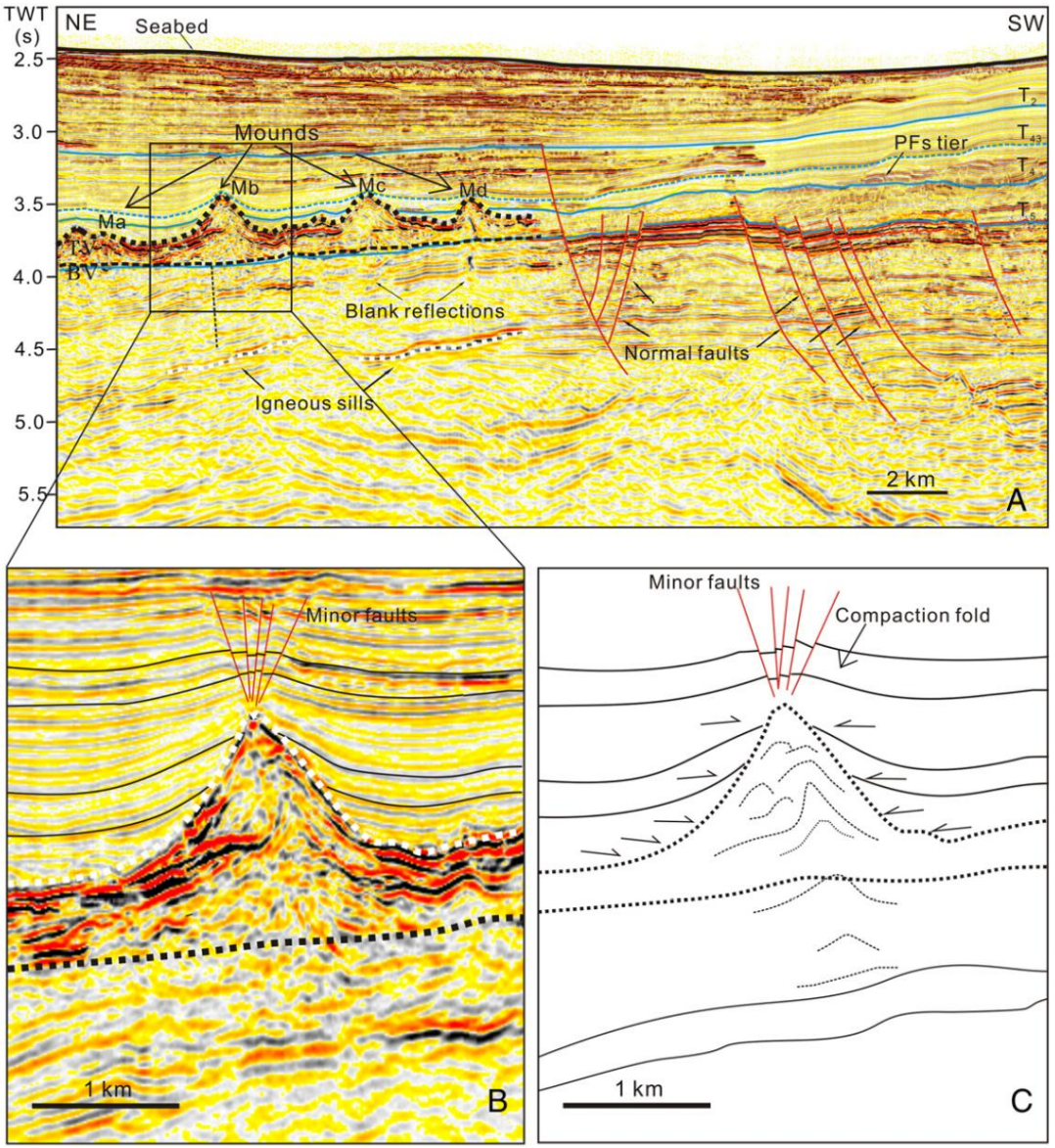

Fig. 6. (A) Representative 3D seismic section illustrating main features described in this paper; see location in Fig. 1B. The section shows 4 mounds (mound a, b c, d) and their geometrical characteristics. The seismic surfaces TM and BM mark the top and the base of the mounds. Three sequence boundaries T_2 (10.5 Ma), T_4 (16 Ma) and T_5 (18.5 Ma) are projected as reference. (B) Close-up of a mound structure developed near the Early Miocene. The internal geometry of the mounds looks layered but discontinuous and reflections within the overburden show a divergent configuration away from the mound structure. (C) Schematic illustration of (B). The mound is downwards defined by horizon BM. T_2, 10.5 Ma; T_4, 16 Ma; T_5, 18.5 Ma. See location in Fig. 1.

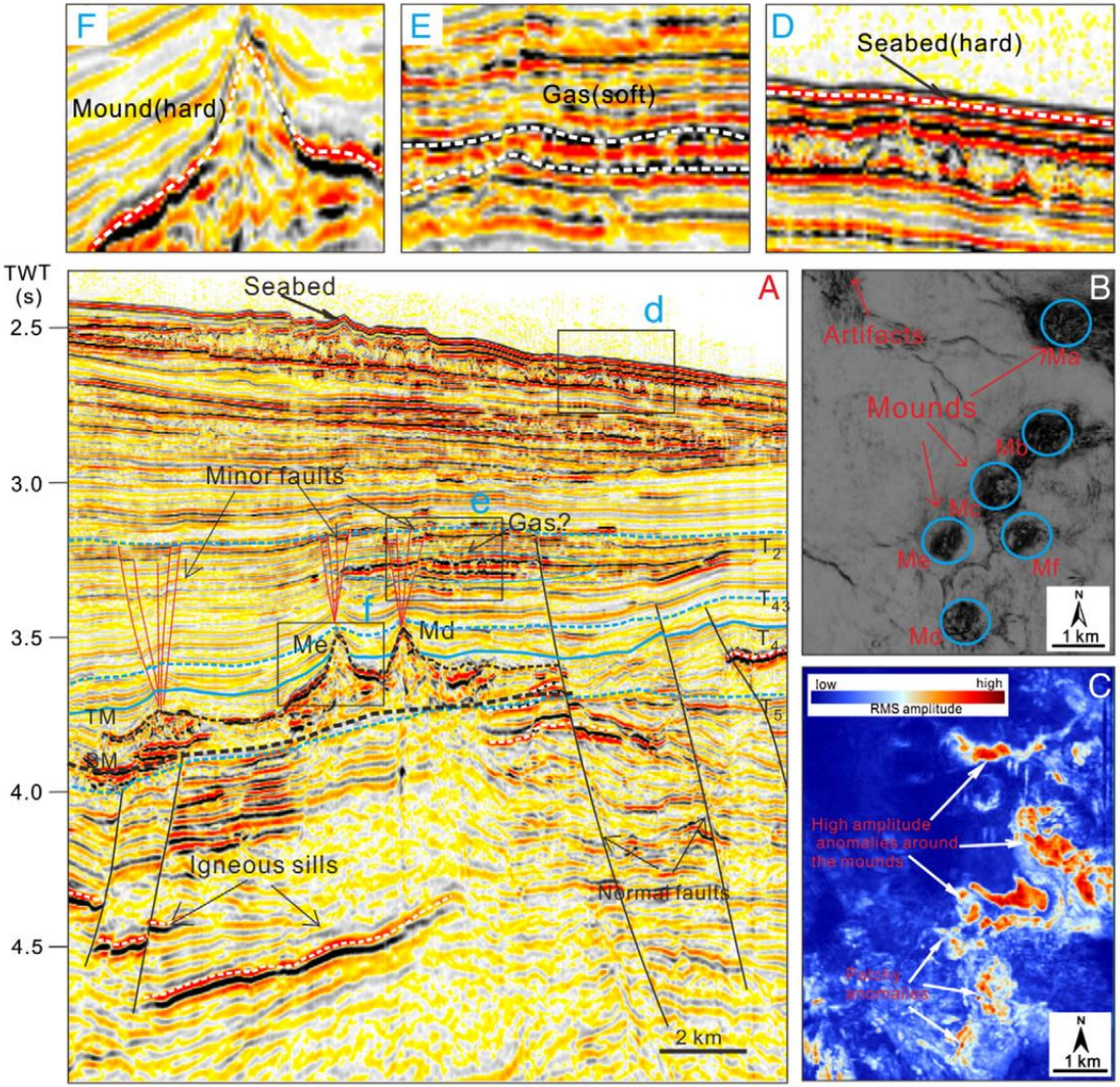

Fig. 7. (A) Seismic section showing three mound-shaped structures; see location in Fig. 1B. Mound e and mound f are developed above the upper tips of faults. Igneous sills are also developed along the faults. Mound d is located above an underlying sill to which they are linked by vertical zones (pipes). (B) The coherence map extracted along a time-slice 3528 ms between horizon T_2 and horizon TM shows low coherence around the mounds that can separate strongly from the surroundings. Mound structures, polygonal faults and tectonic faults are clearly shown. The mounds are imaged as the circular plan view geometry on this map. (C) RMS amplitude extraction from the top and base reflection shows high amplitude anomalies around the mound structures. TM, top mound; BM, base mound. See location in Fig. 1.

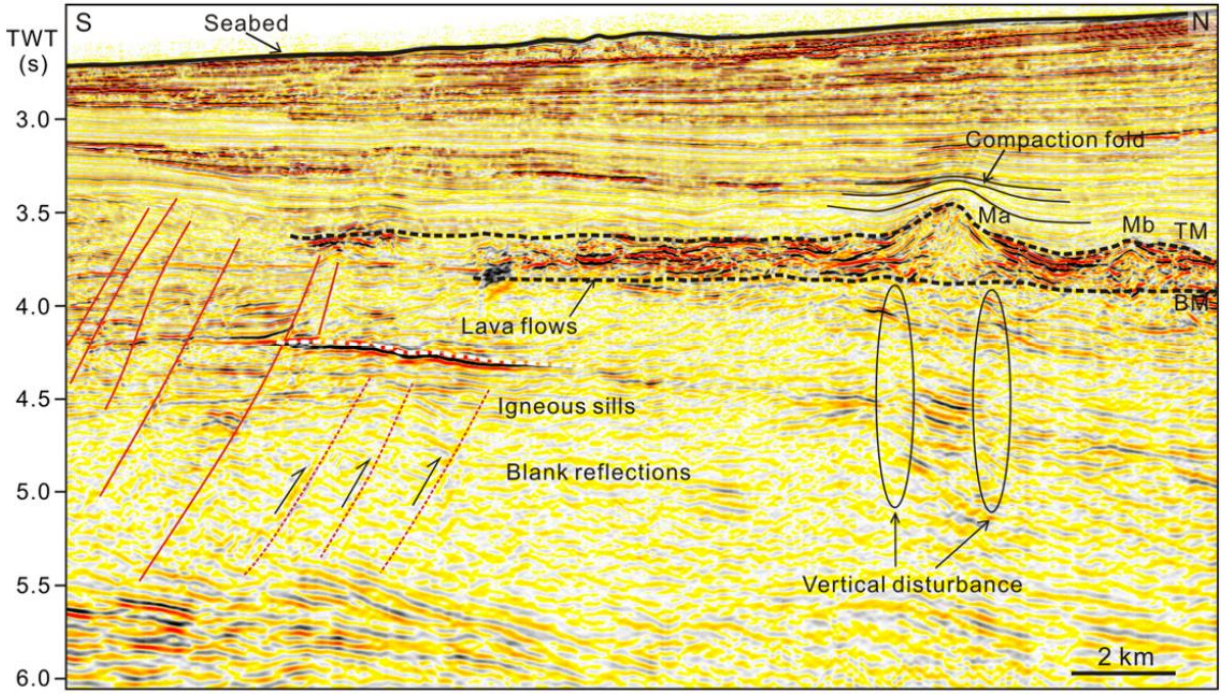

3. Seismic profile from 3D survey area showing the geometry of the mound structures. The mounds are embraced by lava flow units and are clearly onlapped by overlying stratal re-ions. The internal structure has a chaotic, transparent internal geometry different from the surrounding strata. Amplitude anomalies are seen right below the mounds and vertical ırbance can also be seen. The mounds and lava flow units are linked to deep parts by normal faults. Referred vertical magma migration from the interpreted deep lava flow unit to ower levels was facilitated along inclined fault planes. See location in Fig. 1.

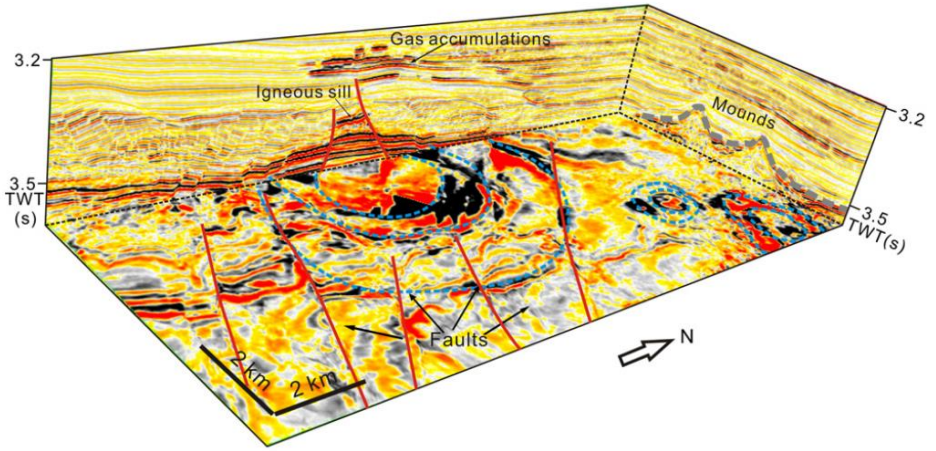

Fig. 9. 3D visualization map showing the internal structure of submarine mounds imaged as a series of internal stacked cones. The NW–NWW faults are represented in seismic section. See location in Fig. 1.

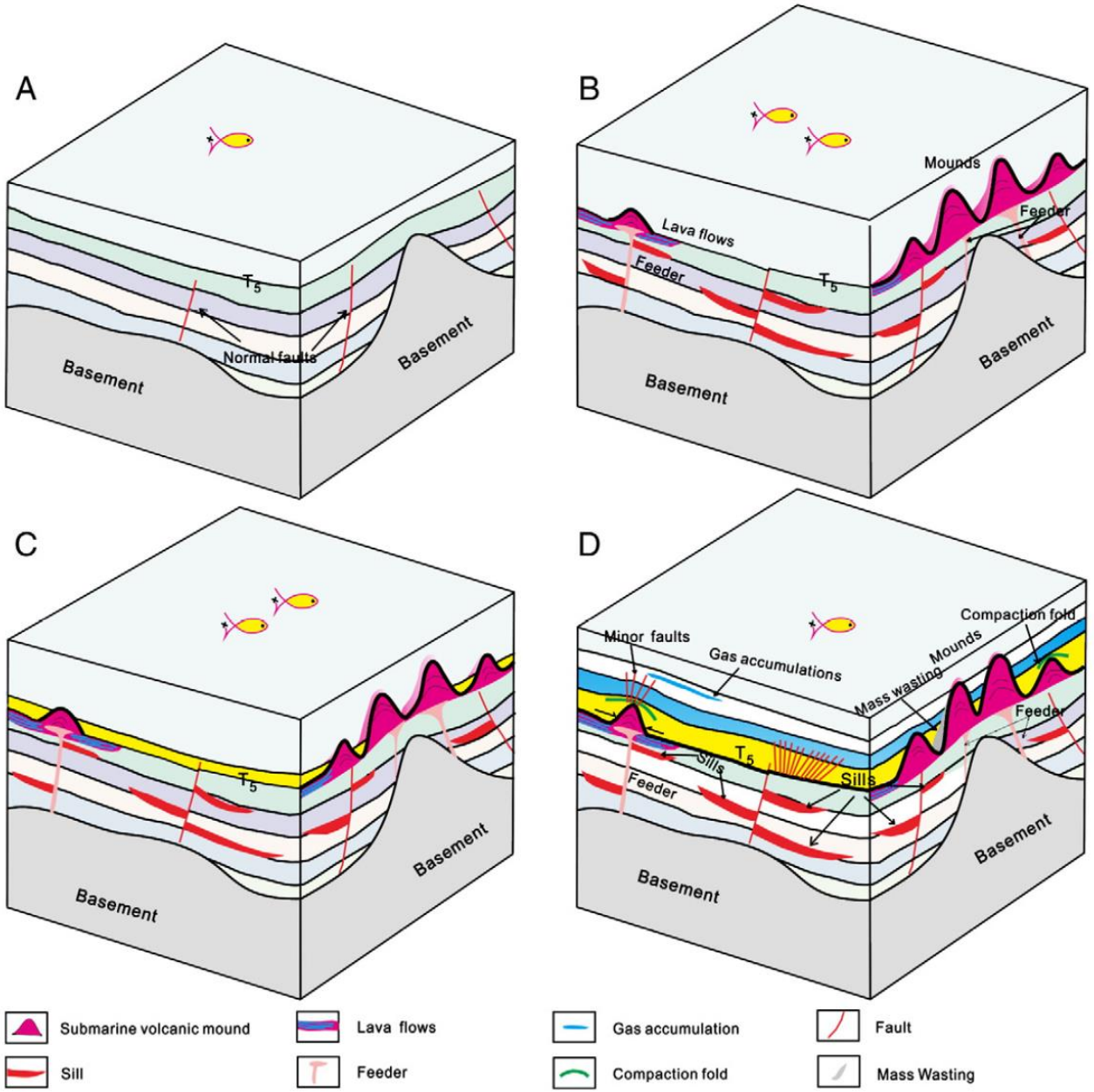

Fig. 10. Schematic four-stage evolution of submarine volcanic mounds and associated structures. The igneous structures (submarine mounds, igneous sills, lava flows, compaction folds, minor faults) and tectonic features (normal faults) were represented to reveal the formation of the igneous plumbing system. For details see Section 5.5.

Норвежская континентальная окраина Баренцева моря

K.O. Omosanya et al. / Marine and Petroleum Geology 76 (2016) 397–411

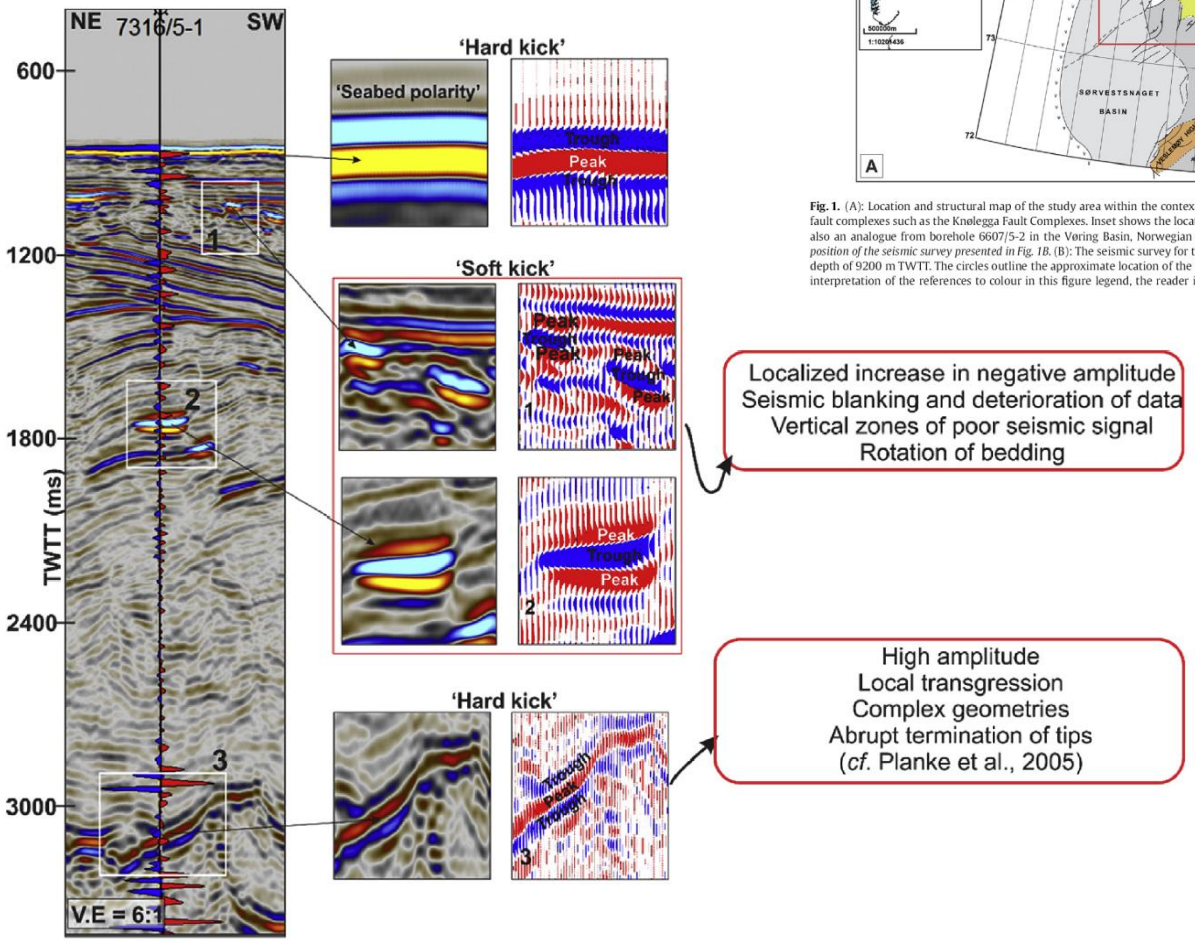

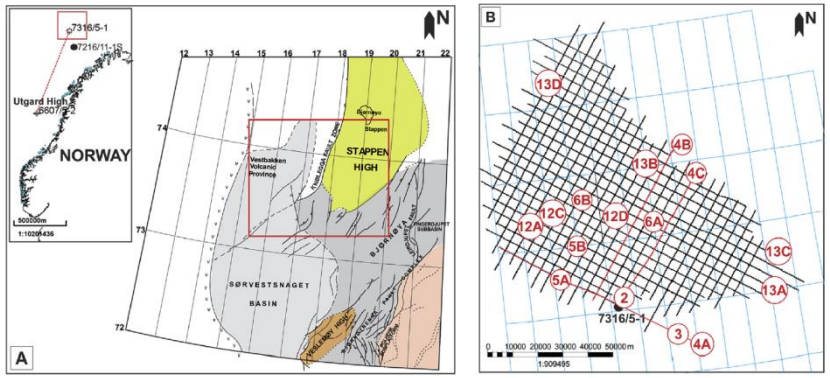

Fig. 1. (A): Location and structural map of the study area within the context of the Southwestern Barents Sea. The Stappen High developed in response to activity along the major fault complexes such as the Knølegga Fault Complexes. Inset shows the location of the borehole used for seismic well tie and cross-plots for the igneous rocks in the study area and also an analogue from borehole 6607/5-2 in the Vøring Basin, Norwegian Sea. The structural map is modified from Gabrielsen et al. (1990). *The red box shows the approximate position of the seismic survey presented in Fig. 1B.* (B): The seismic survey for this study includes approximately 3360 km of multiple 2D seismic reflection lines, which are recorded to depth of 9200 m TWTT. The circles outline the approximate location of the seismic sections shown in the paper. Please note that Fig. 12A and B are the same seismic sections. (For interpretation of the references to colour in this figure legend, the reader is referred to the web version of this article.)

Fig. 2. Workflow used for this research includes using the polarity of the seabed reflector to characterize seismic high-amplitude anomalies into a) 'hard' and b) 'soft' kicks (*cf.* Alves et al., 2015). Hard kicks have complete loop of 'trough-peak-trough' polarity in the same manner as the seabed, while soft kicks are reflected as reversed polarity of 'peak-trough-peak'. Soft kicks are considered as indications of fluid or hydrocarbon in the subsurface. The white boxes on the seismic section highlight example of soft kicks (1 & 2) and hard kick (3). *See* Fig. 1B *for location of the seismic line.*

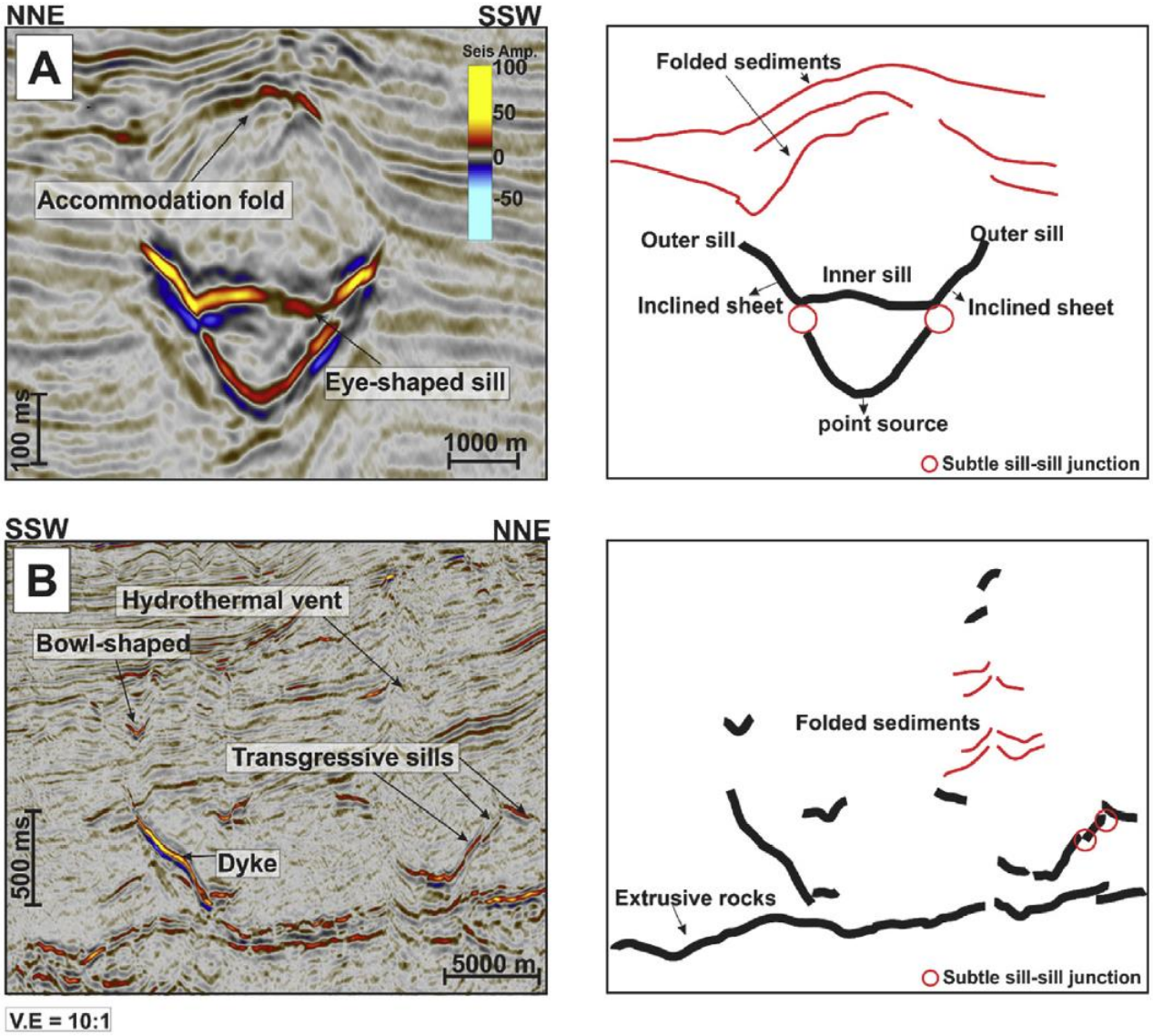

Fig. 5. Examples of 'hard kicks' in the study area. A) The eye -shaped sills are formed by the combination of a saucer-shaped sill (at the top) and a bowl-shaped sill (at the base). The saucer-shaped sill have inner sill and outer sills that are linked by an inclined sheet. Eye-shaped sills are also characterized by accommodation folds at their upper part, which is evidence for post-depositional deformation of the overlying strata B) Transgressive and bowl-shaped sills are found above extrusive rocks. Dykes are vertical to sub-vertical hard kicks, which acted as conduits for emplacement of other sills in the study area. The extrusive rocks are parallel to sub-parallel layered positive high amplitude anomalies. *See* Fig. 1B *for location of the seismic sections.*

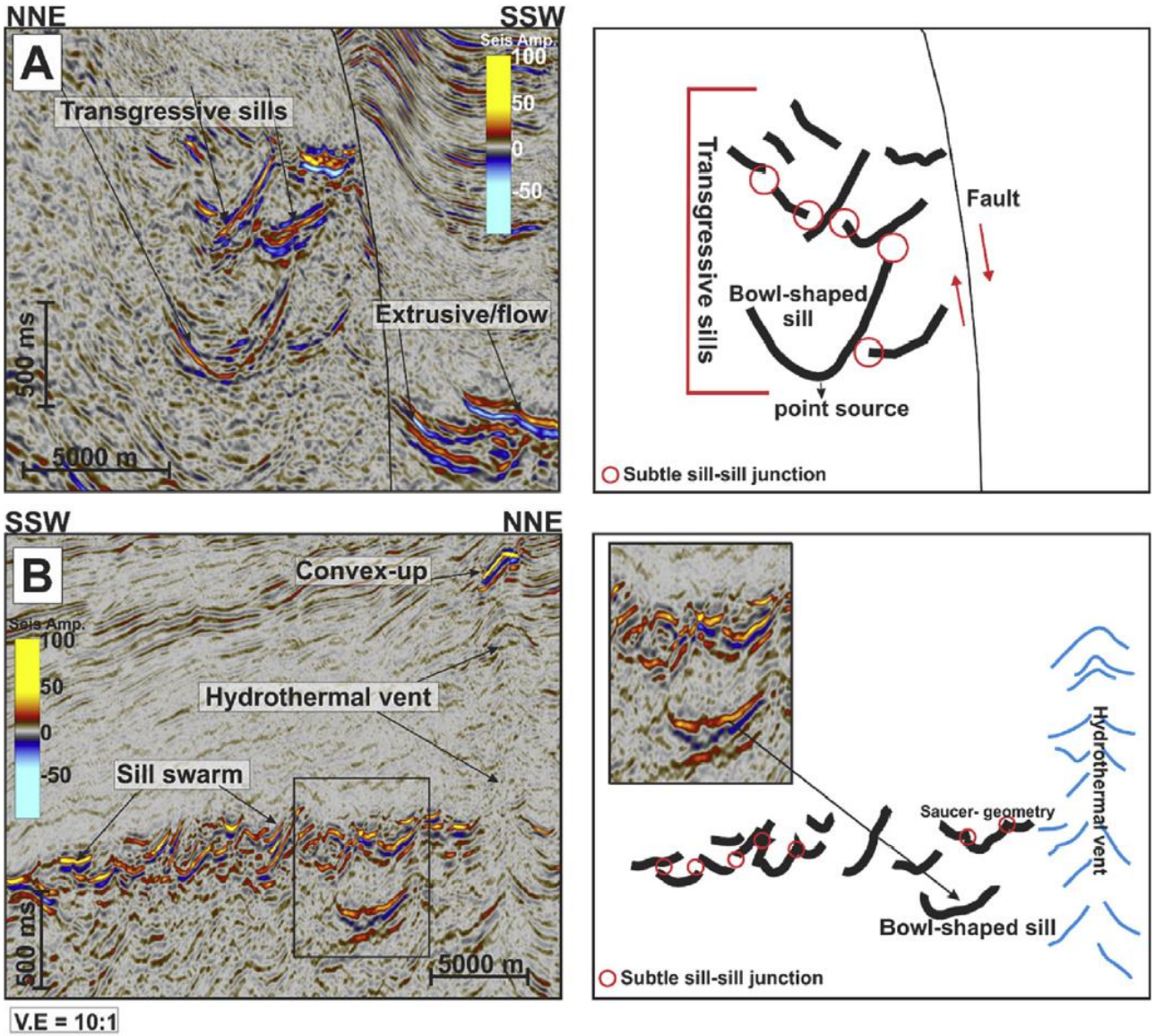

Fig. 6. A) Transgressive sills are upward stepping sills that are connected at subtle sill-sill junctions. They are regularly found close to the extrusive rocks or lava flows. B) The sill swarms are formed by groups of saucer and bowl-shaped sills. They are often associated with hydrothermal vents. Sill swarms in the southern part of the study area form the topography beneath most of the sedimentary overburden. At a local scale, individual sills making up the swarms have diverse geometries. *See* Fig. 1B *for location of the seismic sections.*

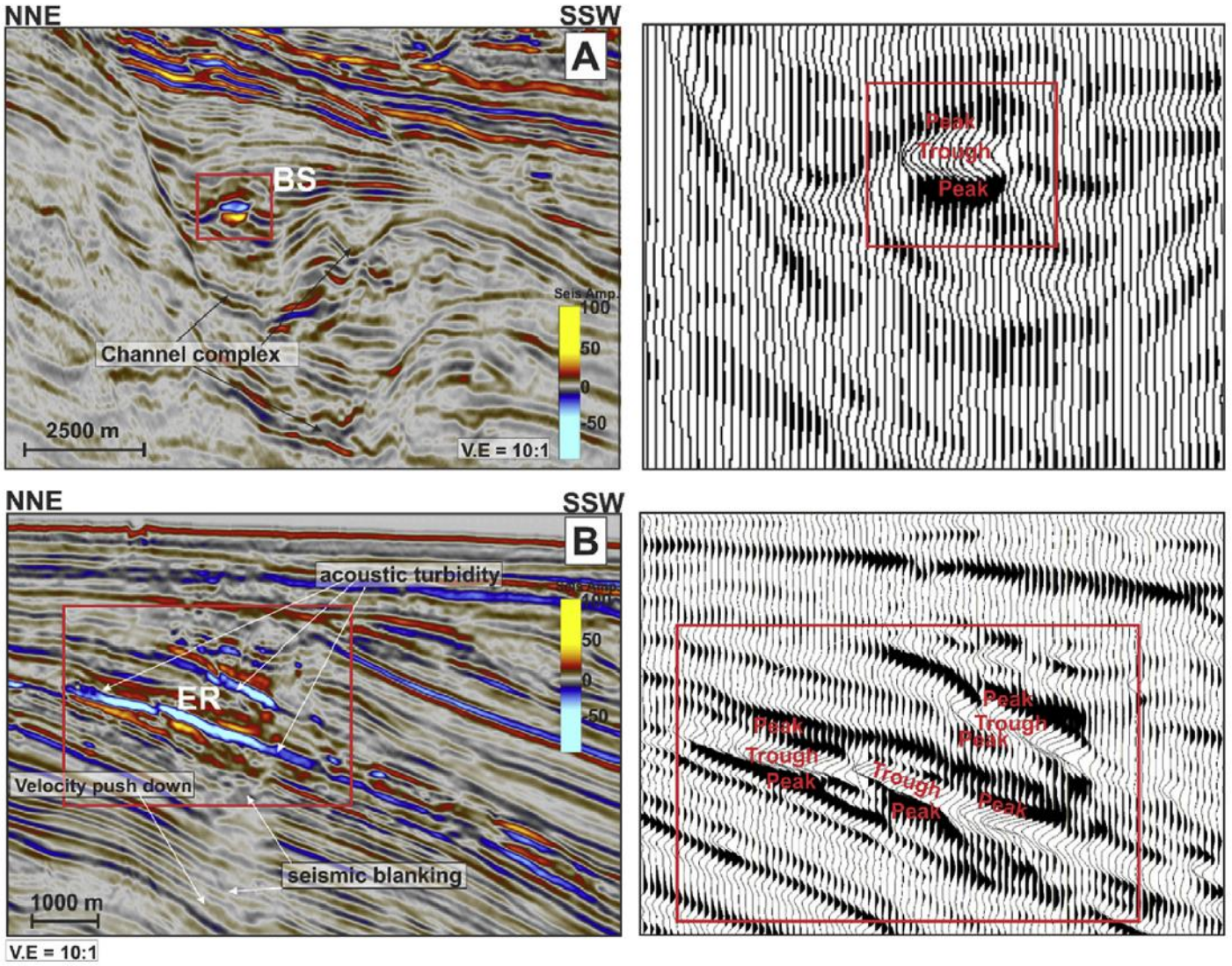

Fig. 7. 'Soft kicks' in this study were interpreted at shallower depth than their 'hard kick' counterparts. They are found within complex channel systems, canyons and also along angular unconformities and bedding planes in the southern and eastern part of the study area. *ER- Enhanced Reflection, BR – Bright Spot. The vertical scales were omitted from the two figures and the locations of the seismic sections are not shown due to the confidential agreement.*

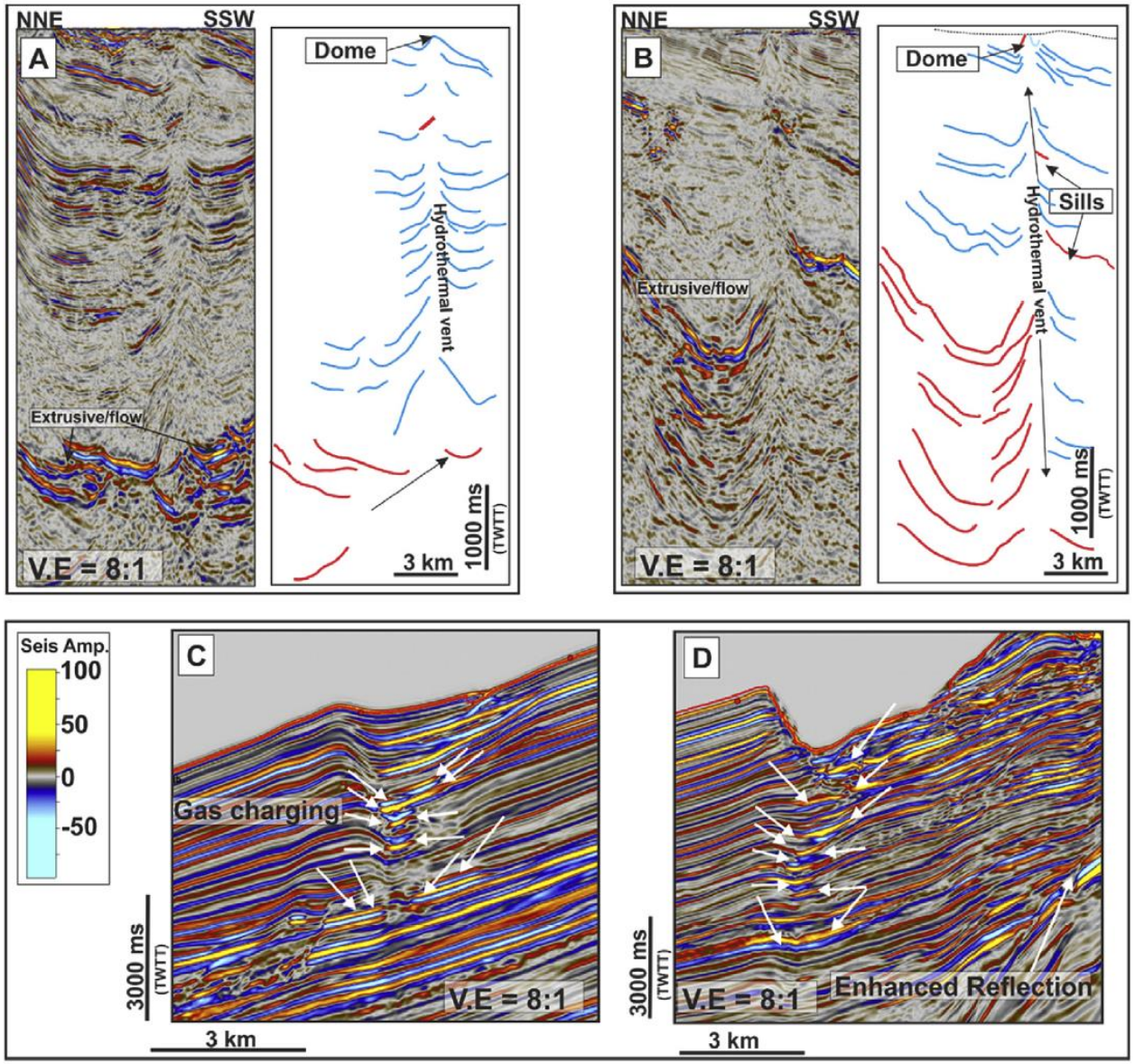

Fig. 13. Examples of focused fluid-flow features include hydrothermal vents which are characterized by (A) a dome at their tops, and (B) whose upper tips have been eroded by the URU. (C) and (D) display a vertical clsuter of enhanced reflections and gas-charged sediments. These kinds of 'soft kick' anomalies are associated with depressions which are manifested as U-shaped craters on the seabed reflector. *See* Fig. 1B *for location of the seismic sections.*

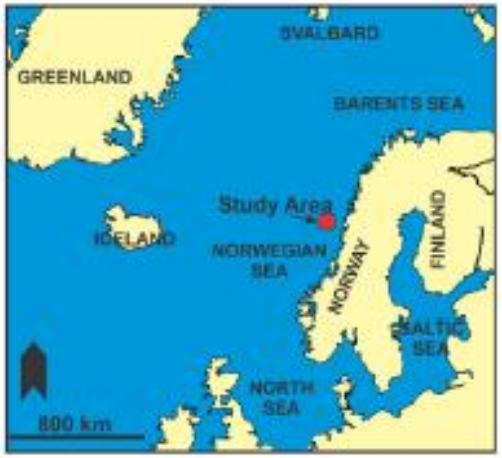

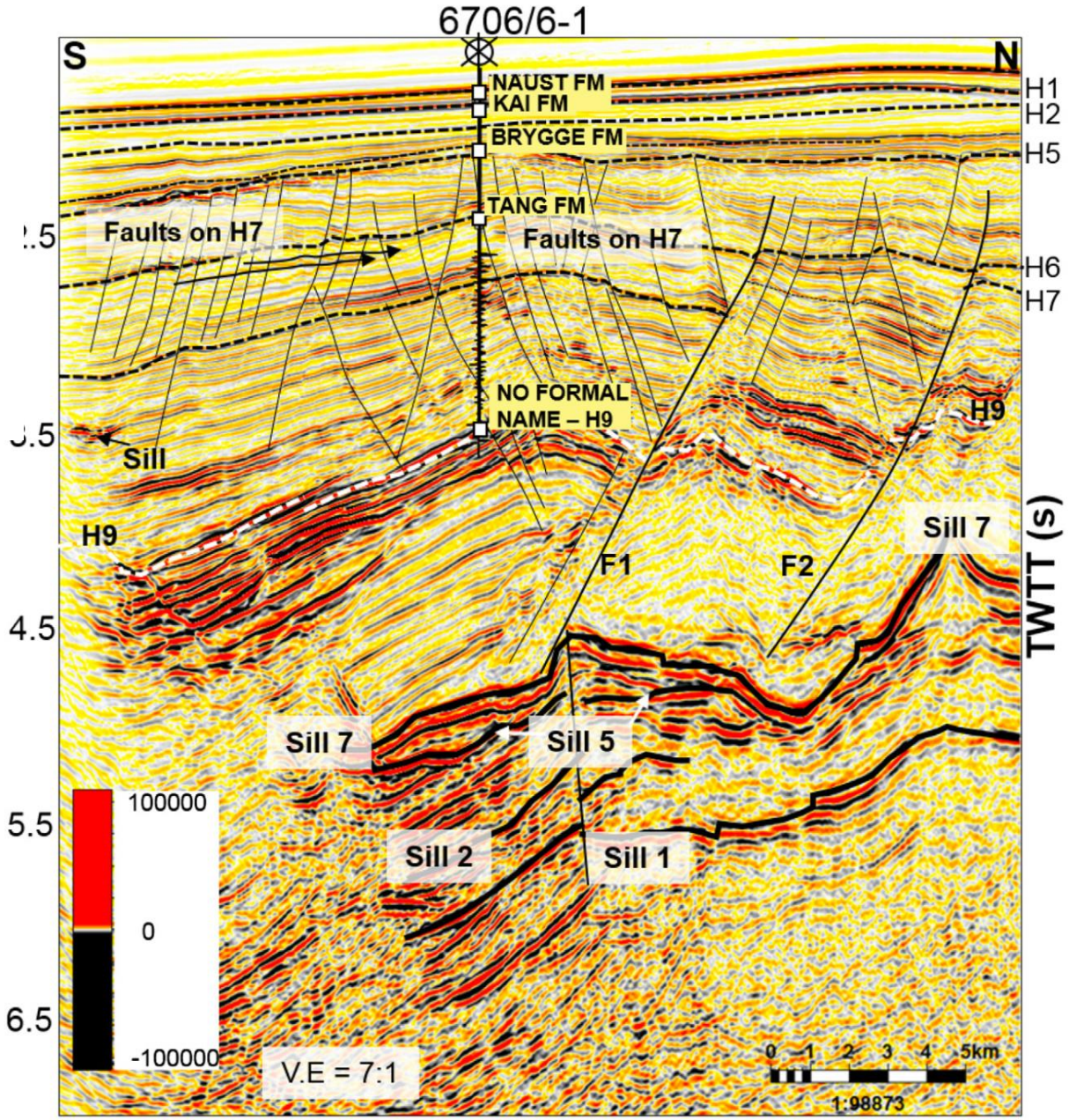

Fig. 2. S-N seismic section showing extensive faulting of the overburden associated with magmatic intrusion and subsequent stretching of the sediments above H9 and H7. Fault F1 and F2 are parts of the principal faults discussed in the text. In association with the magmatic sills are several crisscrossing reflections interpreted as seismic processing artefacts at depth of 5.5 s to 6.5 s TWTT. See Fig. 4d for location of the seismic line. Arrows in the figure are showing onlap reflections above H7.

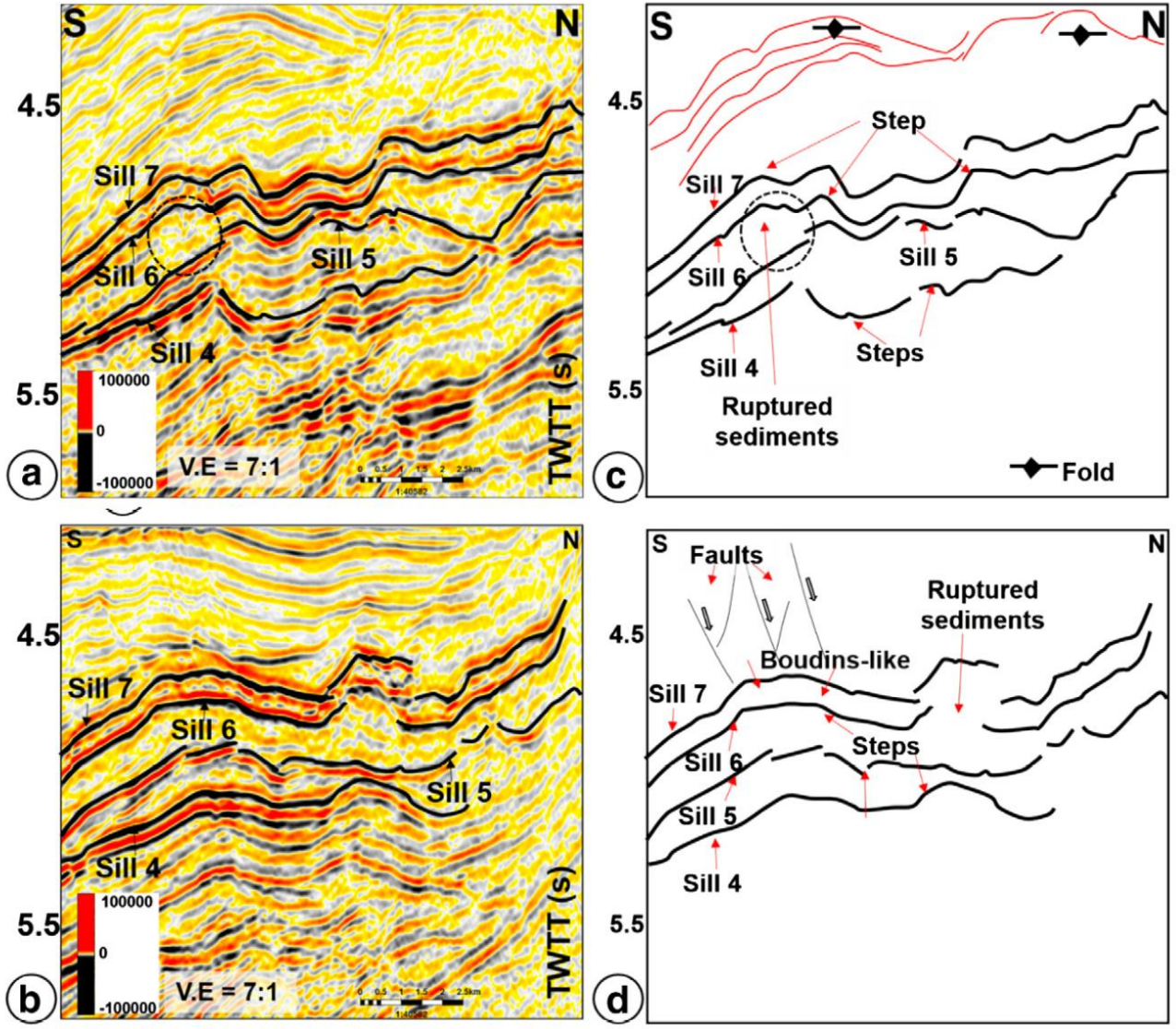

Fig. 10. Seismic section showing steps and other structures associated with brittle deformation of the sills. Steps are flow indicators within magmatic sills, which are generally oriented parallel to the axis of sill emplacement (Schofield et al., 2012a, 2012b; Pollard et al., 1975; Thomson and Hutton, 2004). Steps can be concordant and disconnected when the sills is extended or subjected to brittle deformation. (a) Seismic section showing a concordant pattern of steps in sills 6 and 7, which is discordant with respect to the underlying steps in sills 4 and 5 (b) Seismic section showing faults and steps associated with sills 4 to 7 (c) and (d) schematic interpretation of the seismic section in Fig. 11a and b. See Fig. 7 for location of seismic lines.

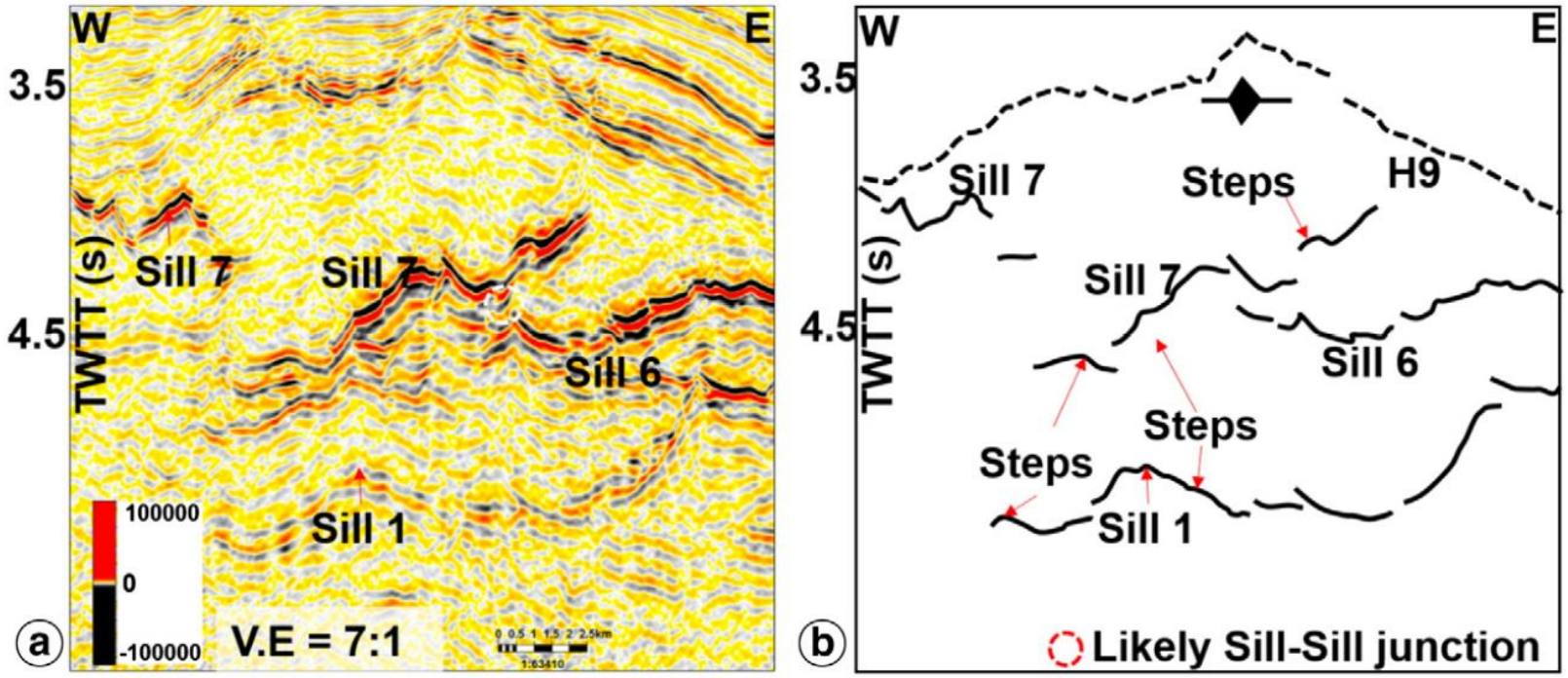

Fig. 11. (a) and (b) Uninterpreted seismic and schematic section showing example of likely sill-sill junctions between Sill 7 and Sill 6. The combination of the two sills would give rise to a transgressive sill in 2D seismic section but in reality, the sills are disconnected and distinct sills in 3D. Also shown in the figure are examples of steps. The figure shows that the apex of the interpreted fold on Horizon H9, which coincides with the crests of the underlying sills. See Fig. 7 for location of seismic line.

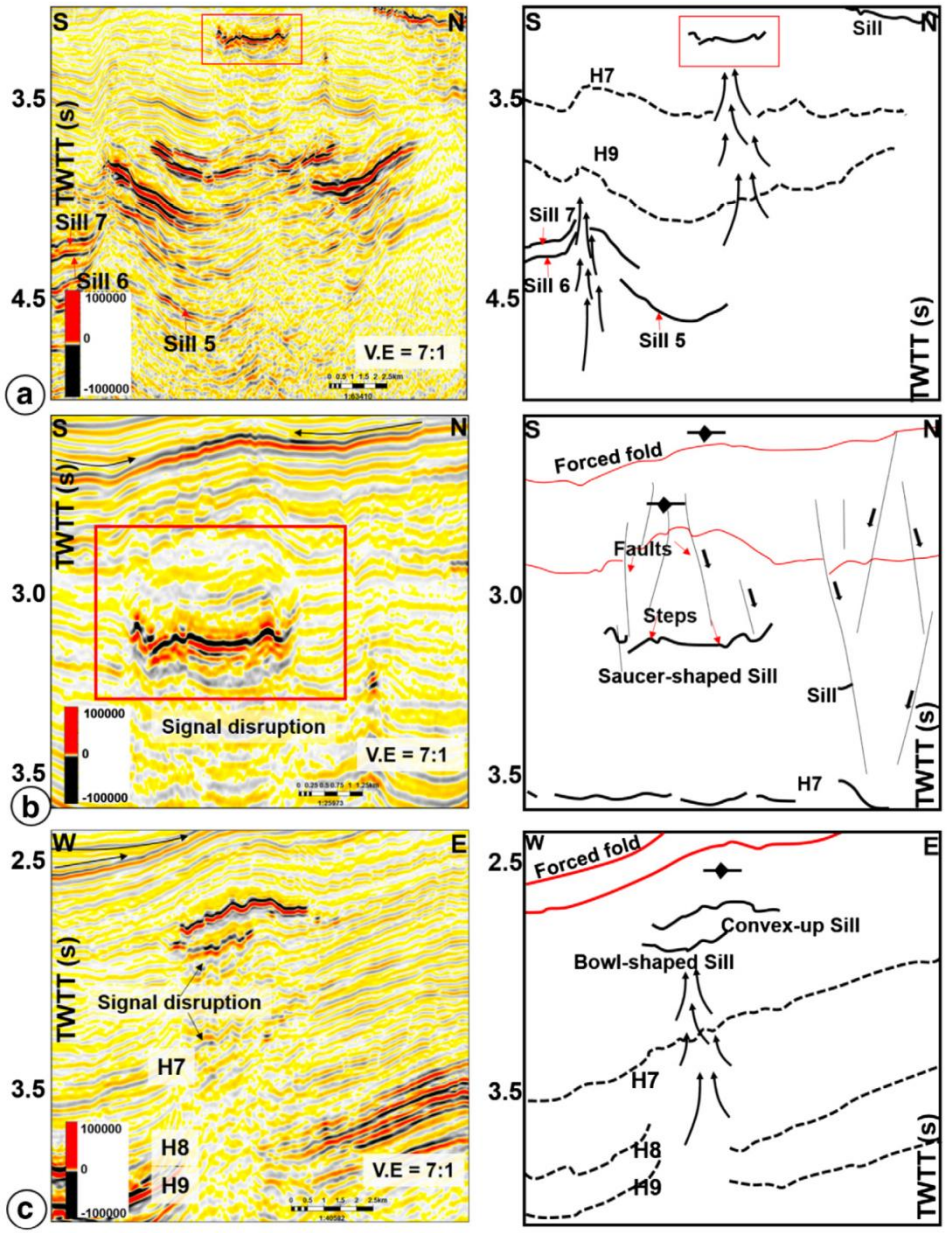

Fig. 12. Additional local accommodation folds interpreted in the study area (a) show that the underlying reflections have moderate amplitude and are disrupted relative to the background reflections. Signal disruption is attributed to fluids emanating from the underlying sills. The bowl-shaped sill is characterized by small-scale fractures and faults on its flanks. Amplitude of the fold is approximately 242 m (using velocity of 2200 m/s) (b) magnified version of the sill in Fig. 13a (c) convex-up sills and evidence for fluid-flow in the study area. Amplitude of the fold at the top of this sill is <110 m (using velocity of 2200 m/s). The adjacent figures are schematic representation of the seismic sections in Fig. 13a–c. See Fig. 6c for location of seismic lines.

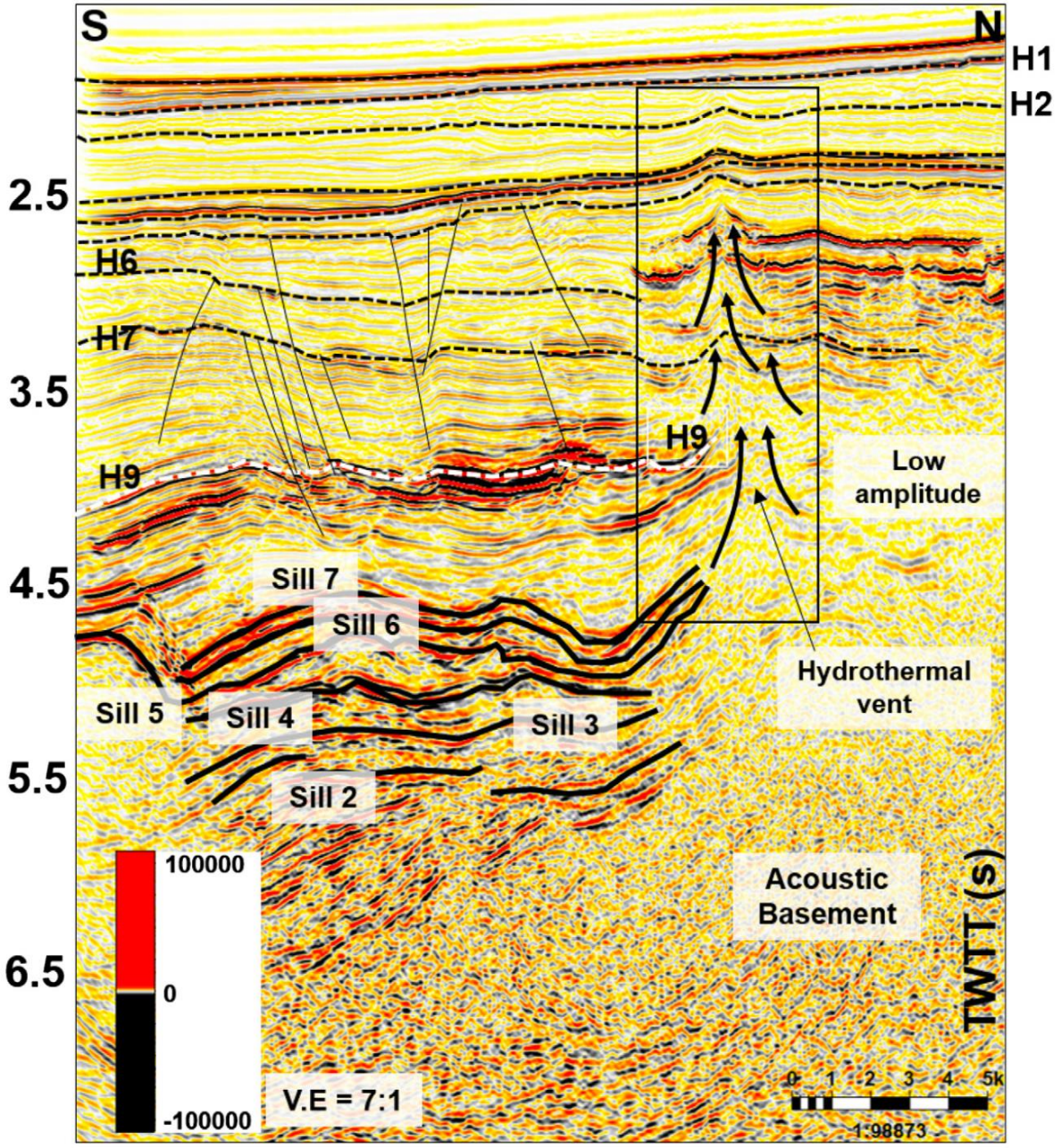

Fig. 13. S-N seismic section showing example of a fluid flow conduit interpreted in the study area. In this example, the fluid flow conduit is characterized by an upper part that is dome-shaped typical of hydrothermal vent complex. From top to base, the hydrothermal vent is intersected by several sills. Hence the conical shape from base to top. The seismic character of the reflections below the sills is distinct from those of the vent complex and the underlying inferred acoustic basement. See Fig. 4d for location of seismic line.

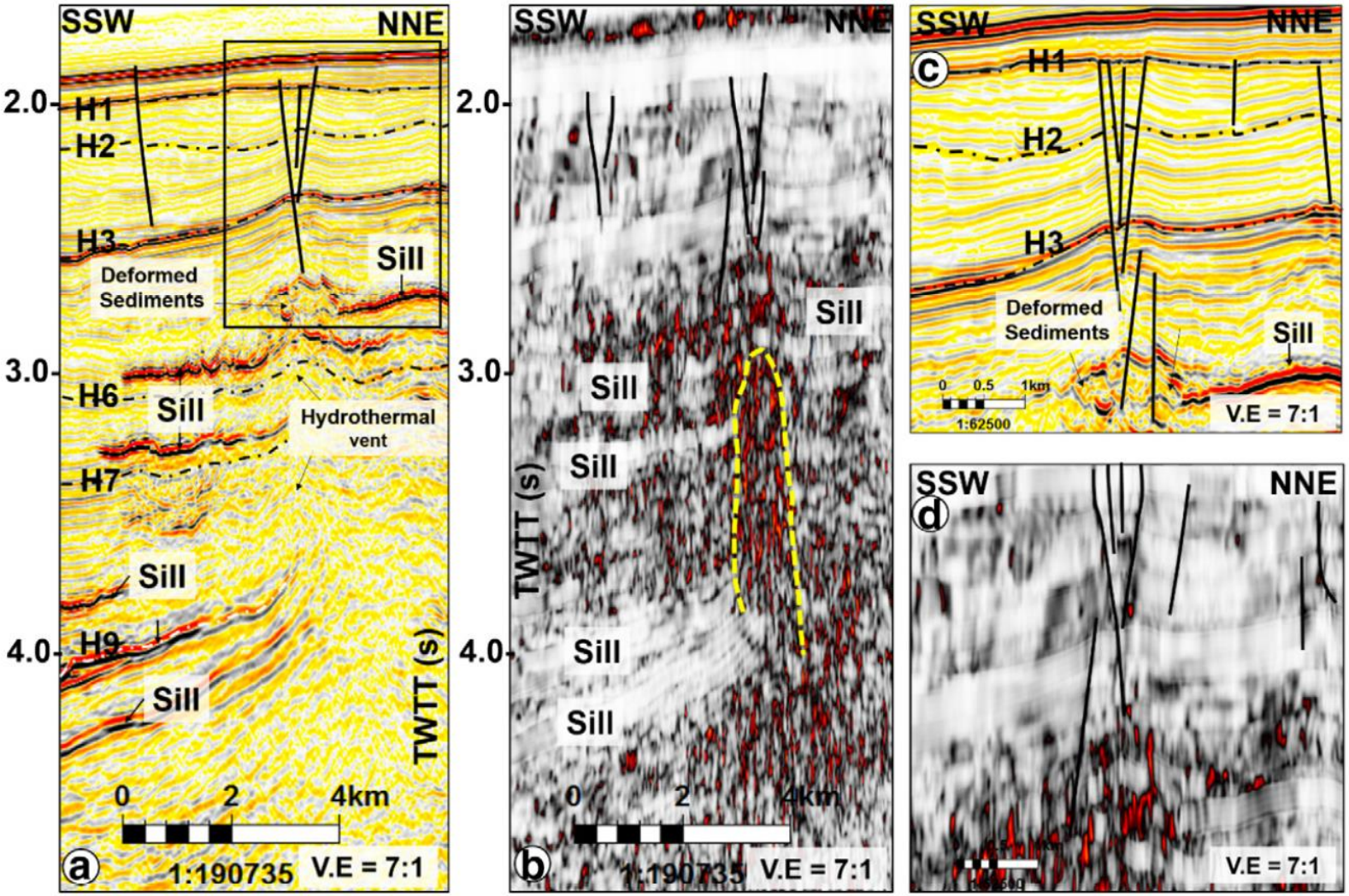

Fig. 14. (a) SSW-NNE seismic section through the hydrothermal vent complex. Towards the upper part of the conduit, sills deformed the sediments into disrupted low to medium reflections and are interpreted as deformed sediments. (b) Chaos seismic section through the vent shown in 14a. The chaotic signal associated with the migration of fluid through the vent made it possible to interpret the geometry of the vent (c) Faulting at the upper of the vents is related to the presence of older sills (d) a chaos seismic section through the same section in Fig. 14c. See Fig. 7 for location of seismic line.

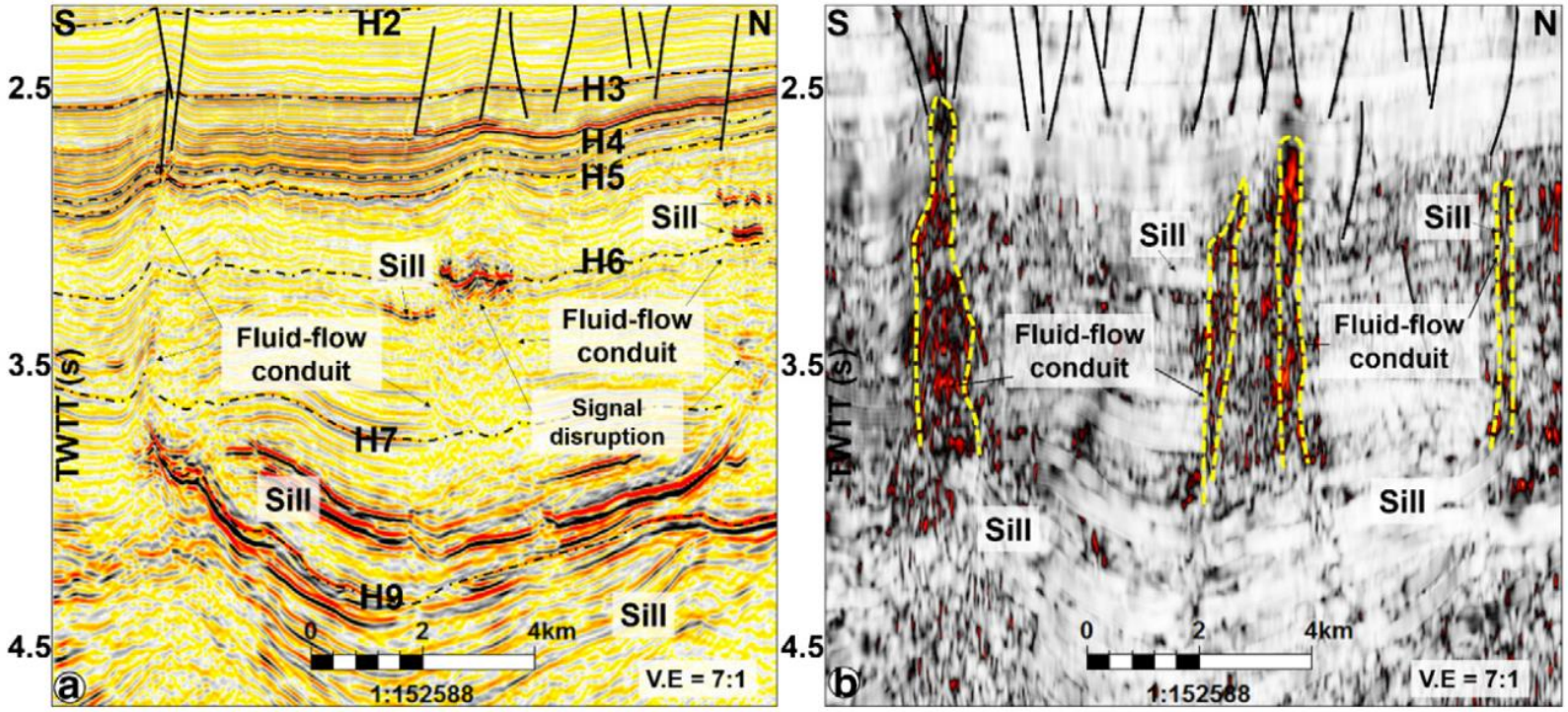

Fig. 15. (a) Examples of distinct fluid-flow conduits or like hydrothermal vent complexes that show less interaction with magmatic sills from across stratigraphic levels. The bases of the vents are located on at the tips of the underlying sill complex. (b) Chaos seismic section through the same section in Fig. 14c. This seismic attribute has allowed the geometry of the conduits/hydrothermal vents to be interpreted as conical and columnar. See the yellow circle in Fig. 7 for location of seismic line.

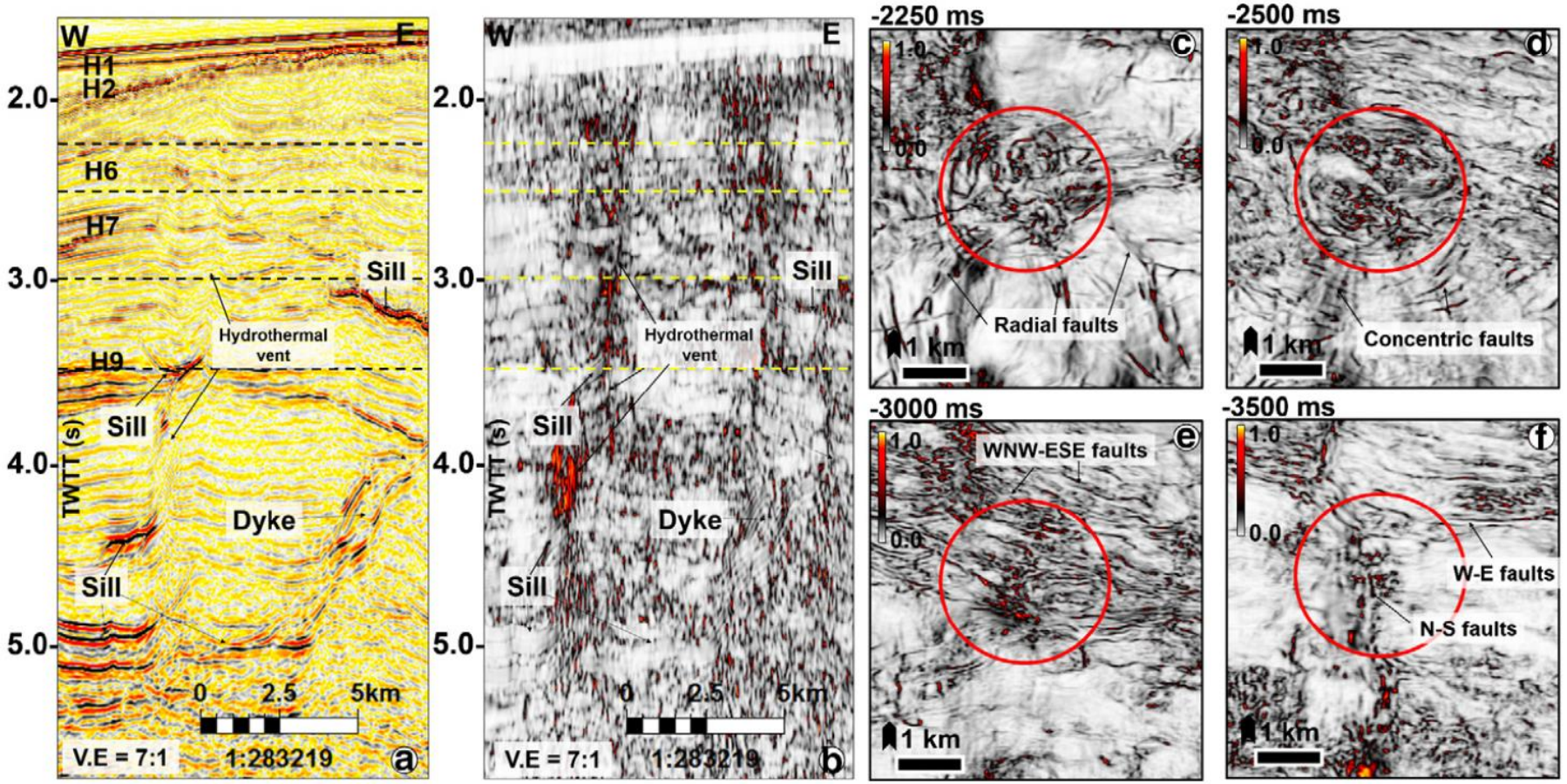

Fig. 16. Examples of hydrothermal vent complexes that are intersected by magmatic sills across stratigraphic levels. The presence of the sills along the path of the vents makes it hard to distinguish the individual reflections on seismic sections. Also interpreted in the study area are dykes, which are sub-vertical high amplitude reflections between sills. To distinguish the sills, vents, dykes and other reflections, a chaos seismic section is provided in (b). In addition to sills interacting with hydrothermal vents, the passage of fluid from these vents is linked to disparage deformation of the overburden. (c) to (f) shows the different faults types that are associated with the vent shown in (a). See Fig. 7 for location of seismic line.

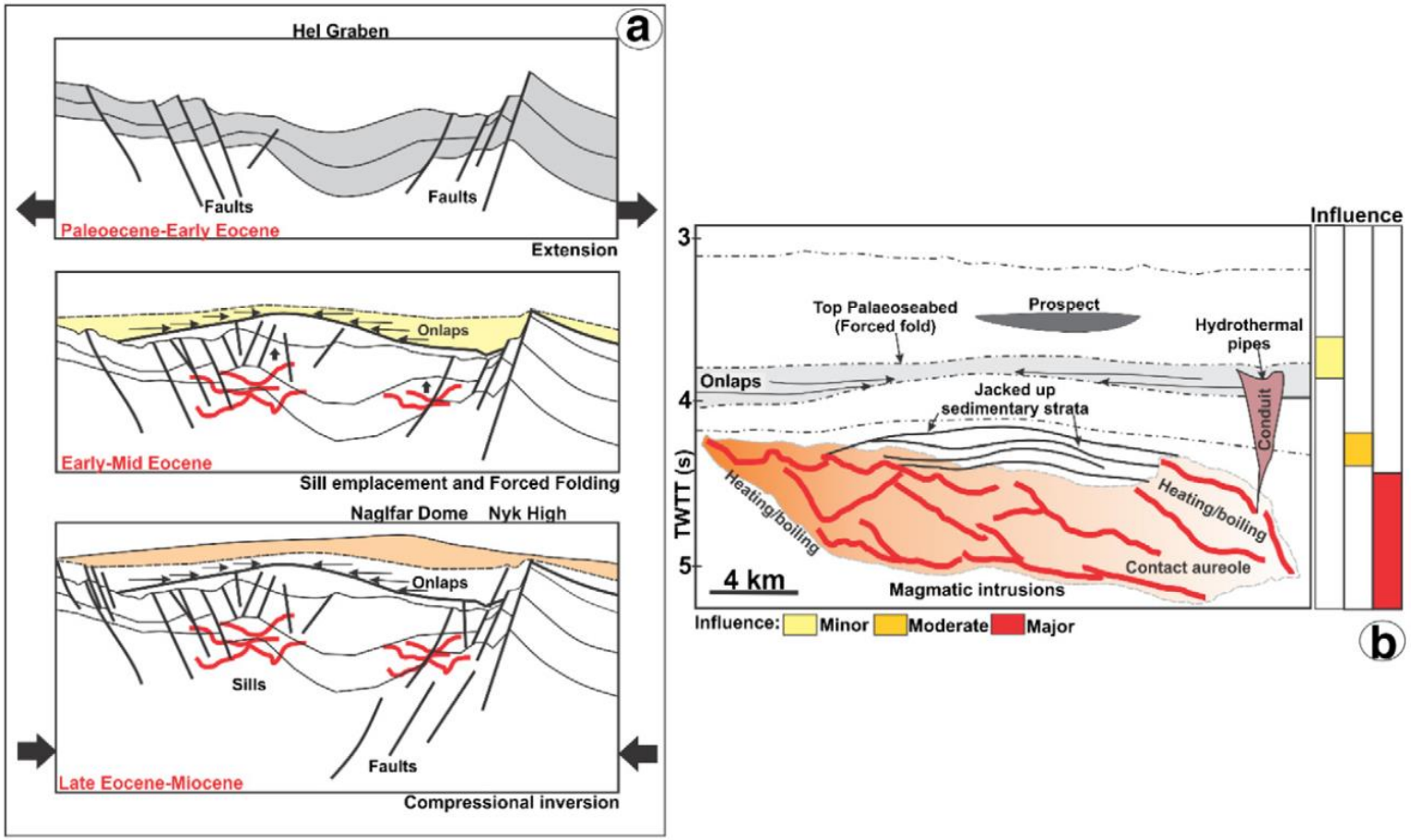

Fig. 17. (a) Conceptual model explaining the evolution of the regional forced fold on Horizon 7 and the Naglfar Dome. The forced fold is direct manifestation of the forceful emplacement of magma through the sedimentary rocks in Early to Mid-Eocene while the Naglfar Dome on the other hand evolved in Miocene in response to regional compressional inversion that affected the Vøring Basin. (b) Schematic diagram explaining the implication of magmatic intrusion on reservoir and source rock quality and compartmentalization as modified the work of Rohrman (2007). The geosection is located in the North Atlantic Igneous Province (NAIP). The effect of magmatic intrusion decreases with increasing distance from the sills. The contact aureole has been included based on the model of Planke et al. (2005).

Южная Америка

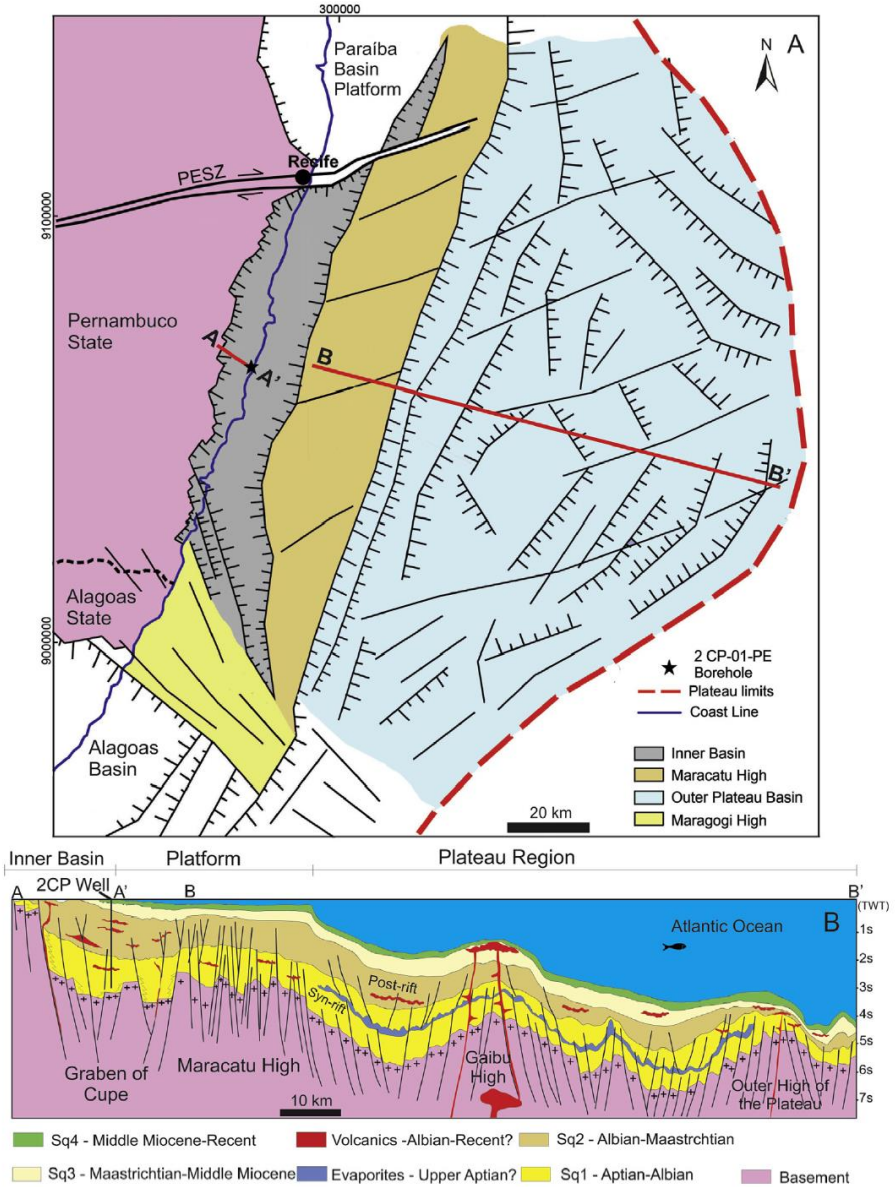

Fig. 2. A) Simplified structural map that shows the main domains of the Pernambuco Basin. B) Schematic geological section based on the interpretation of two 2D seismic sections (A–A′ and BB′), which are marked by the red continuous lines. The black star marks the location of the 2CP-01-PE stratigraphic well. The individualizations and estimated ages of the main seismic-sequences are based on the stratigraphic analysis performed under this research, the onshore stratigraphic framework (Barbosa et al., 2014), and correlation with the stratigraphy of the offshore neighbouring Alagoas Basin. (For interpretation of the references to colour in this figure legend, the reader is referred to the web version of this article.)

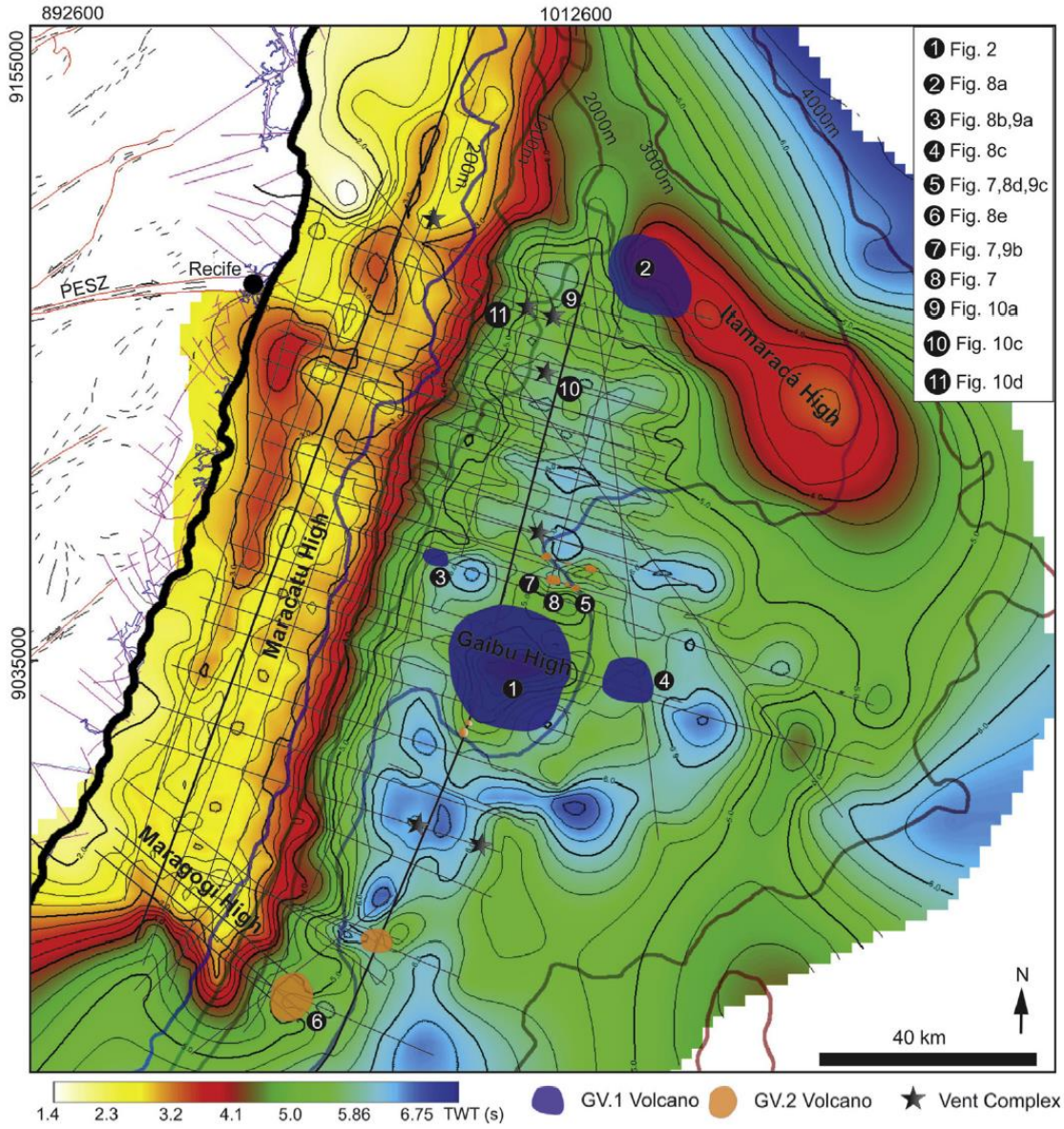

Fig. 4. Map showing the locations of the 59 selected seismic sections across the offshore domains of the Pernambuco Basin; they were selected to best describe the volcanic structures. The basement structural contour in time is also shown, revealing the main topographic highs and depocentres of the basin. The blue polygons indicate the location of the GV1 volcanic group, the orange polygons indicate the volcanic structures included in the GV2 group, and the black stars indicate the locations of vents. (For interpretation of the references to colour in this figure legend, the reader is referred to the web version of this article.)

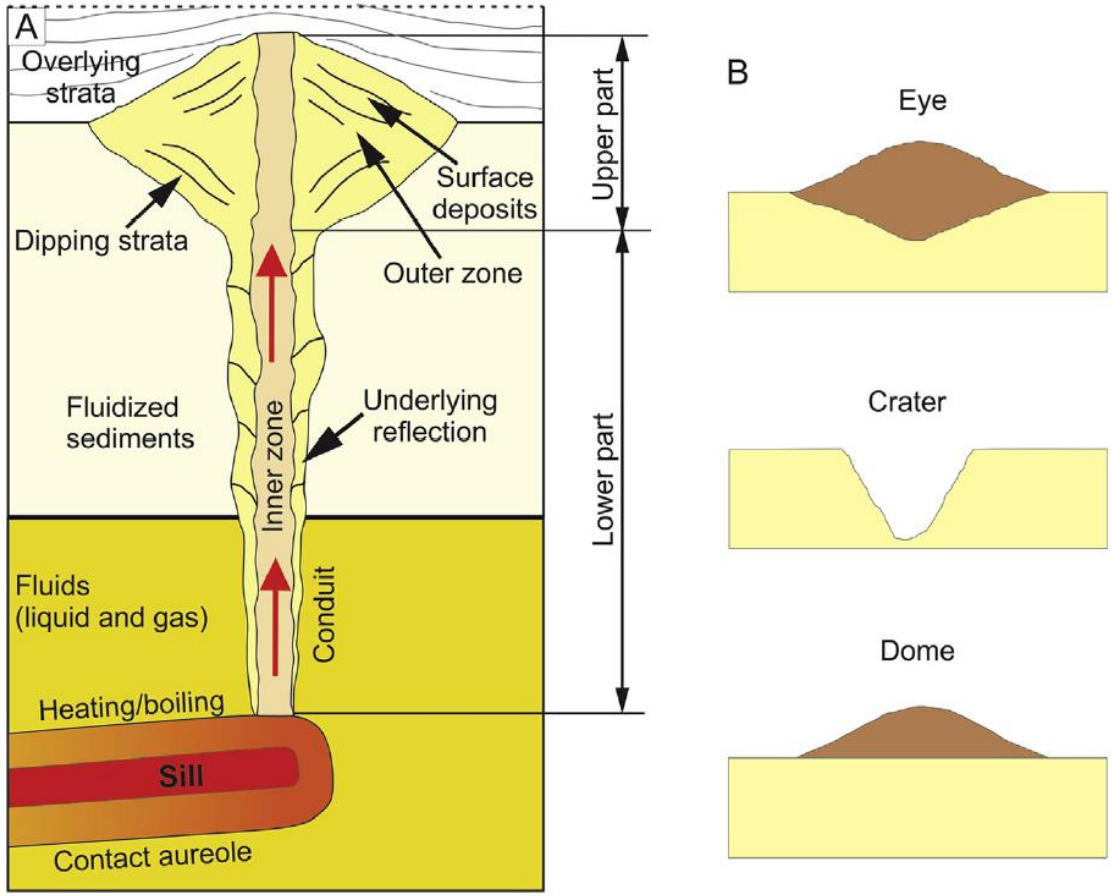

Fig. 5. A) Schematic description of a volcanic vent, with the main relations of the overlying and internal strata geometries that were used to define its general classification (modified from Planke et al., 2005). B) geometry of the upper part of the vent complexes.

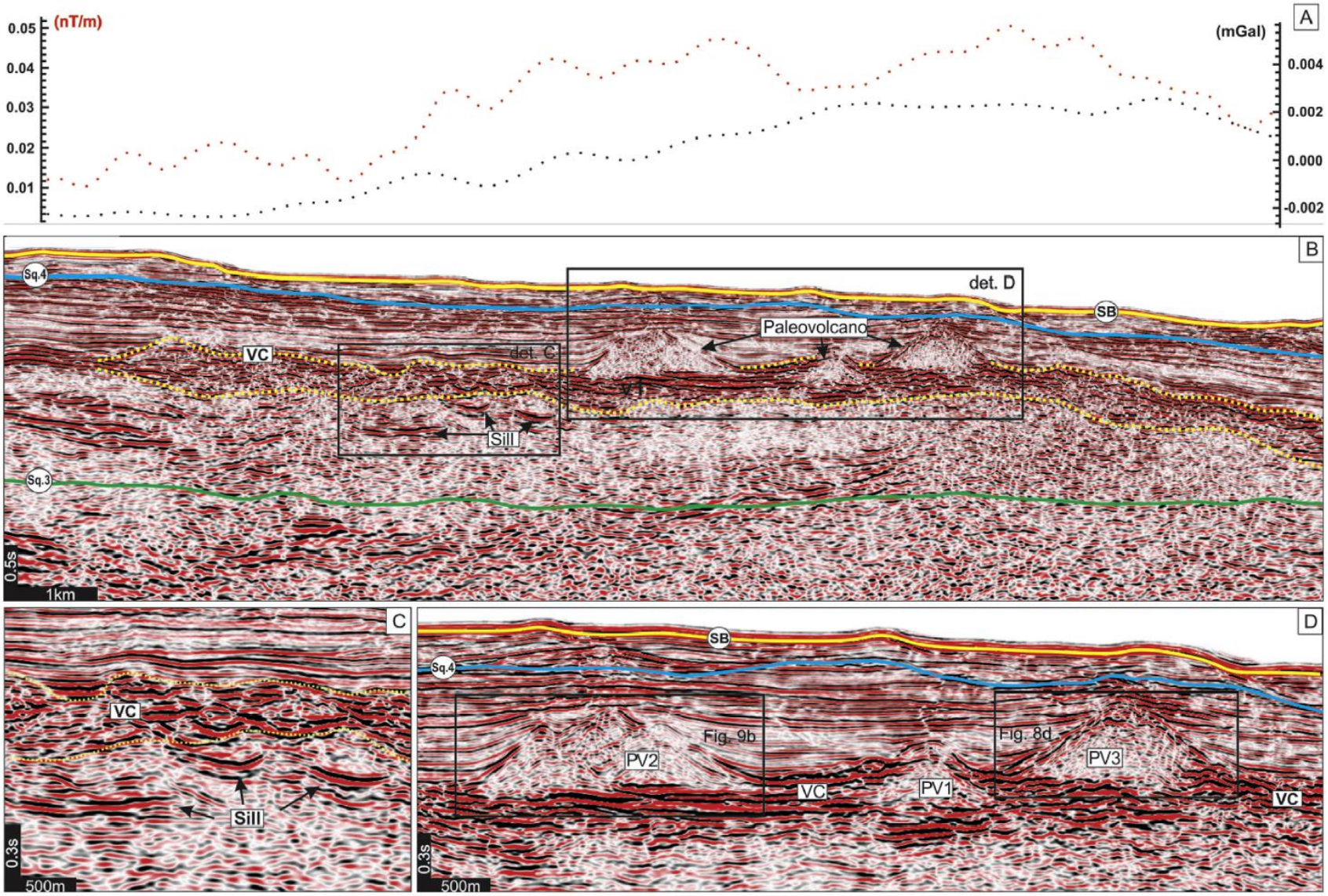

Fig. 7. Seismic section (see the location in Fig. 4) showing a series of volcanic structures. A) Magnetic and gravimetric curves acquired over the seismic section showing an anomaly caused by the volcanic structures. B) Examples of the interpreted volcanic buildings (PV1–PV3), sills and related sequences of volcaniclastic deposits (VC–dotted yellow line). SB = Sea bed; Sq.4 = Middle Miocene Unconformity; Sq.3 = Maastrichtian Unconformity. C) Detail of volcaniclastic deposits and sill intrusions presenting high amplitudes with abrupt terminations. D) Detail of cone-shaped volcanic buildings and volcaniclastic deposits between them. PV2 is interpreted as having a polygenetic evolution. (For interpretation of the references to colour in this figure legend, the reader is referred to the web version of this article.)

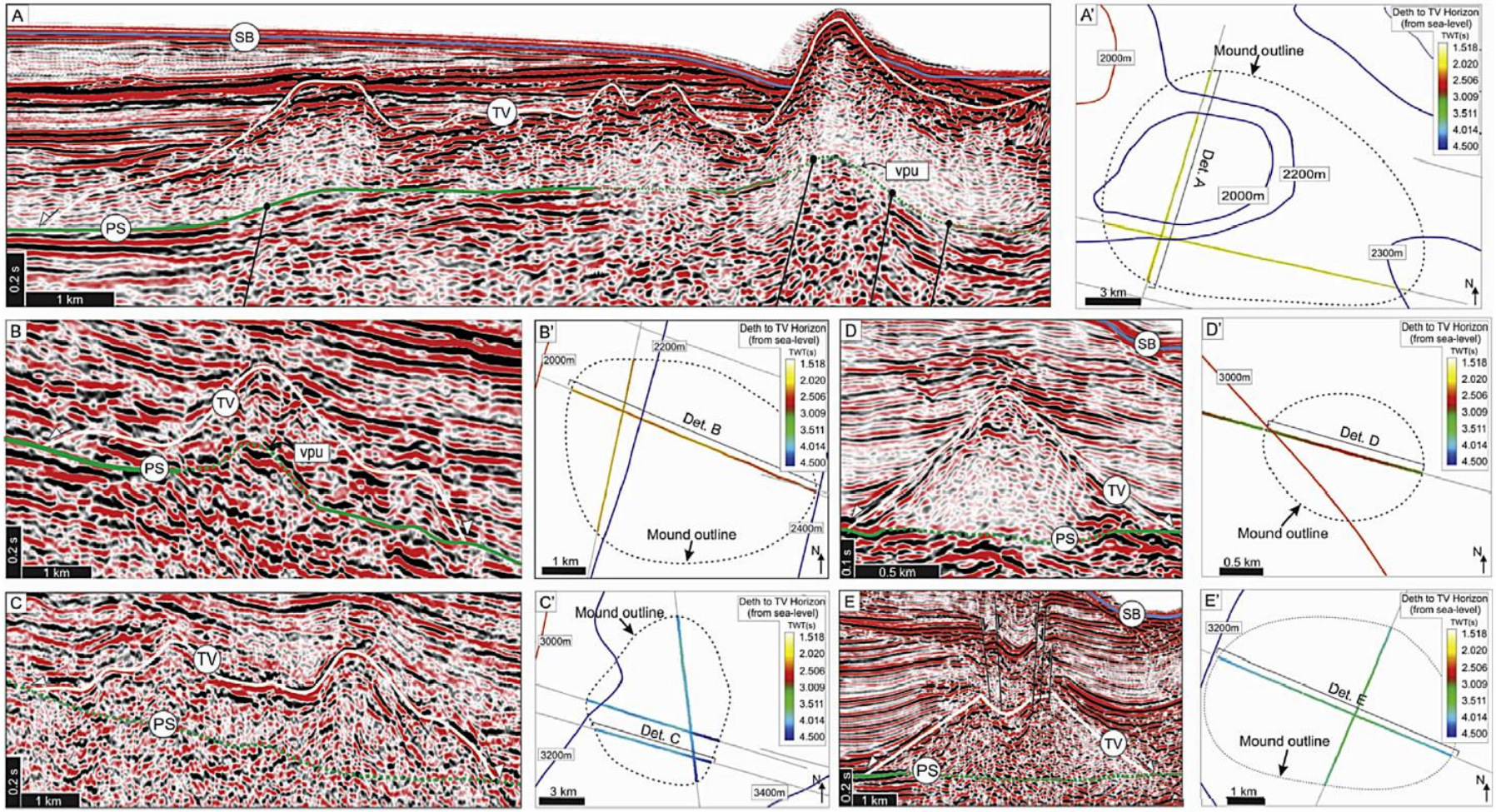

Fig. 8. Volcanic structures observed in seismic sections of the Pernambuco Plateau. A to E) composed detail of the samples and the location of the structure shown in Fig. 4. A, B, and C) volcanoes of group GV1. D and E) volcanoes of group GV2. The dotted lines represent the estimated diameters of the structure as interpreted in intersecting seismic sections (vpu – velocity pull-up, PS – reflector marking the palaeo seabed horizon that served as the base for extrusive building, TV – reflector marking the top of the horizon).

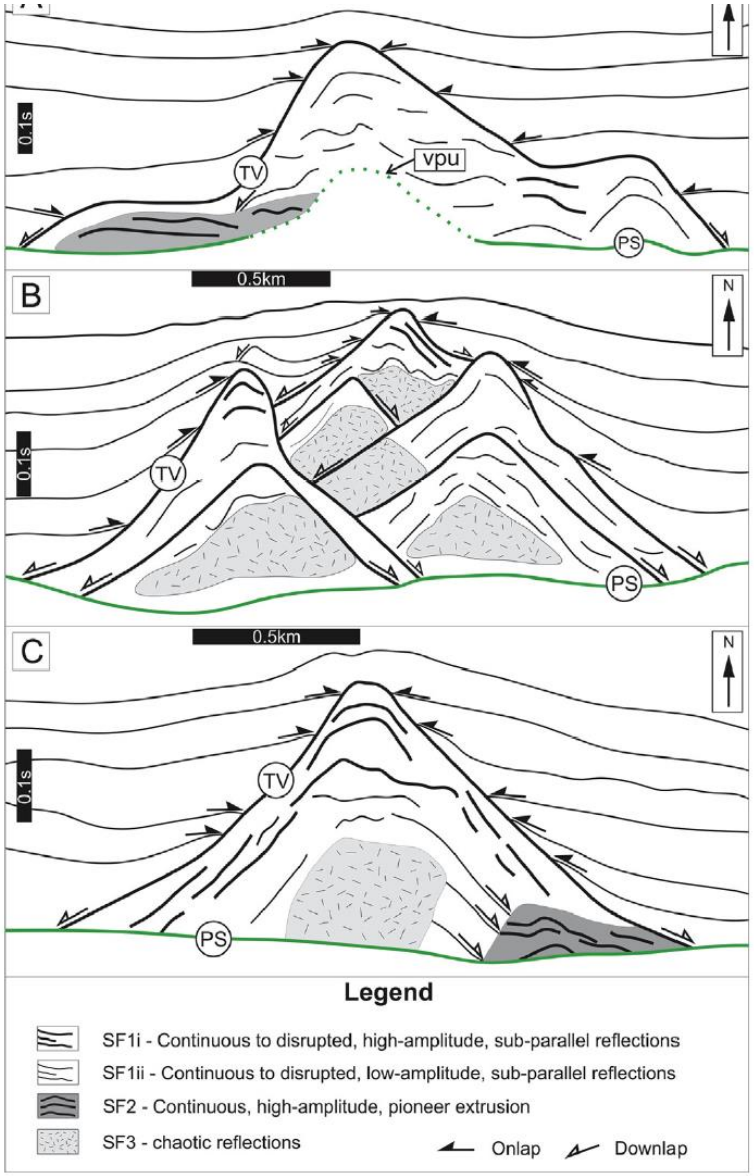

Fig. 9. Schematic of the three groups of strata that form the volcanic structures, based on the seismic facies interpretation. A) Schematic based on the volcano in Fig. 8b, B) schematic based on the interpretation of the structure in Fig. 7d, and C) schematic based on the interpretation of the structure in Figs. 7d and 8d.

Австралия

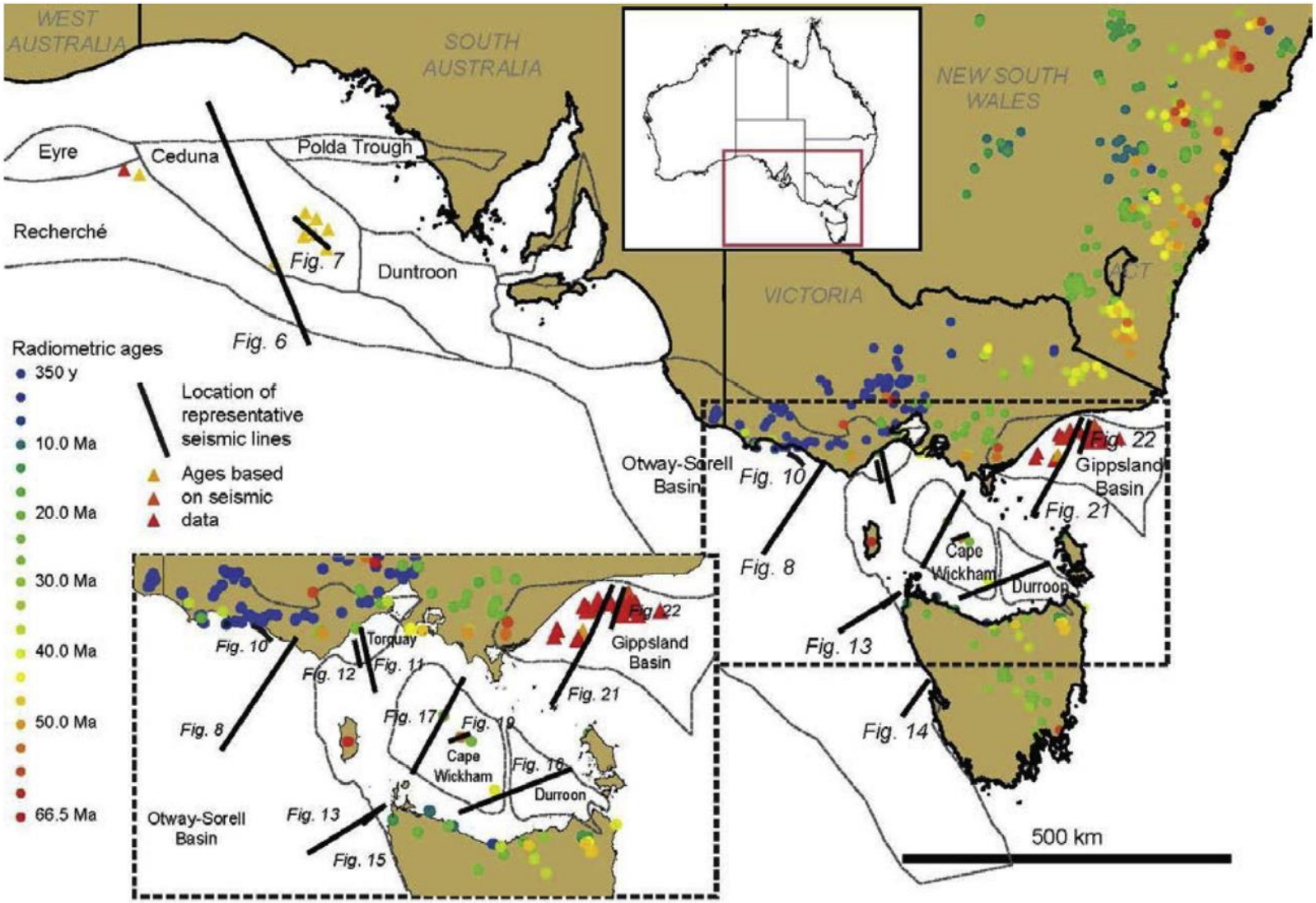

Fig. 5. Distribution of Cenozoic volcanic rocks along the Australian southern margin with locations of colour-coded age-dated samples (compiled from Vasconcelos et al. (2008), Gibson (2007), O'Brien et al. (2008)) and location of representative seismic lines discussed further in the text.

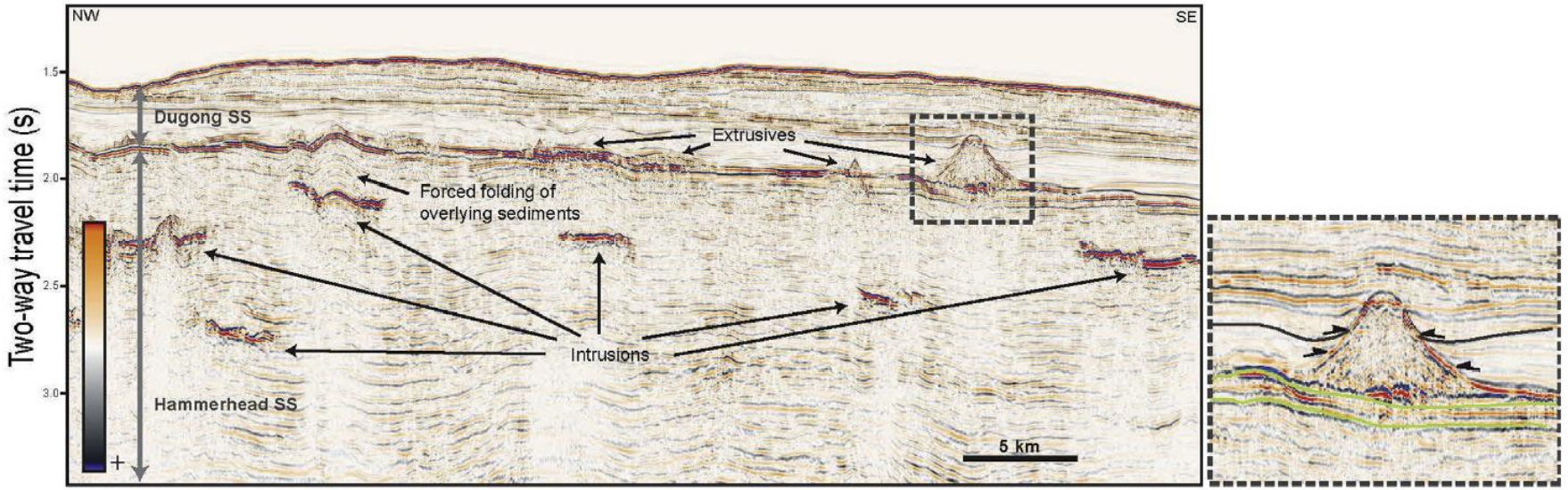

Fig. 7. Part of seismic line w00fdw0087 (reverse SEG polarity). Examples of magmatic features in the Ceduna sub-basin of the Bight Basin. Location of seismic line is shown in Fig. 5.

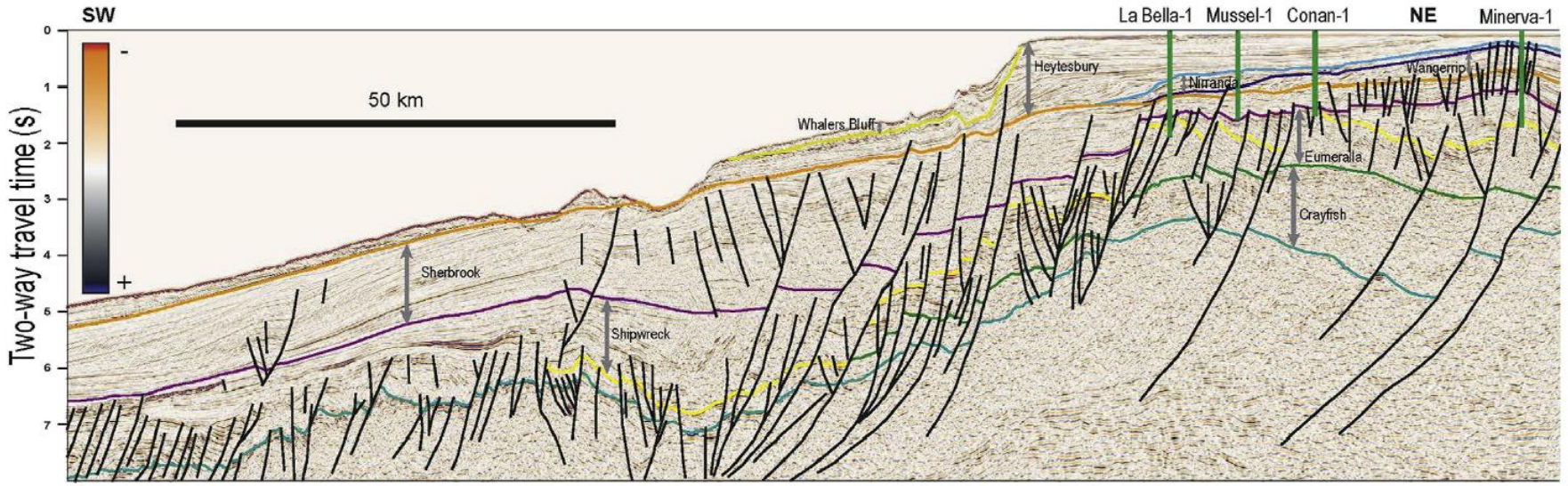

Fig. 8. Seismic line 137-09 (reverse SEG polarity). Eastern Otway regional cross-section, interpretation modified from Krassay et al. (2004). Location of seismic line is shown in Fig. 5.

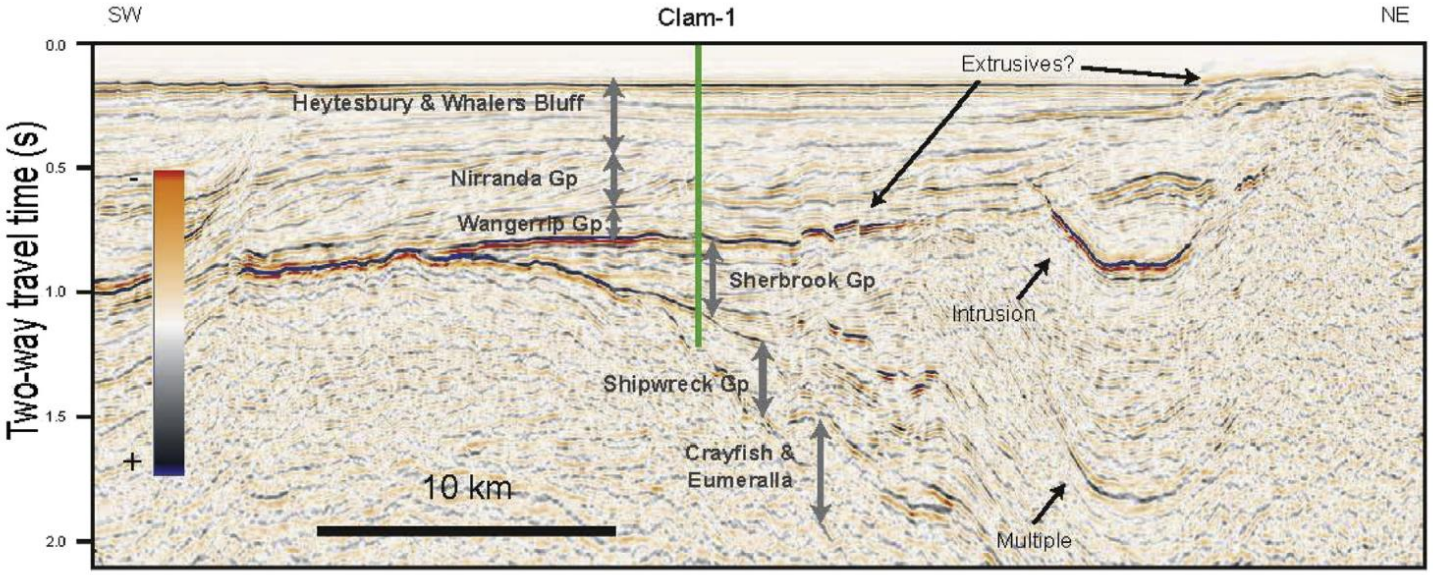

Fig. 15. Part of seismic line 078-05 (reverse SEG polarity). Examples of magmatic features in the Sorell Basin. Location of seismic line is shown in Fig. 5.

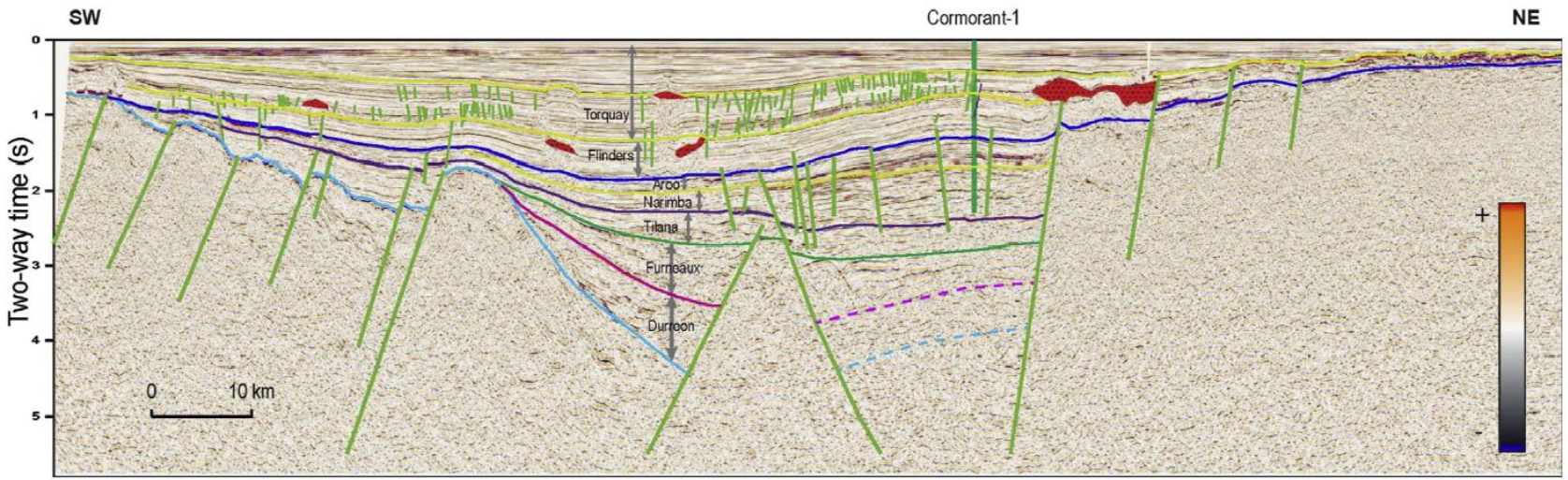

Fig. 17. Seismic line 90-27 (normal SEG polarity). Bass Basin – Cape Wickham sub-basin regional cross-section, with igneous features indicated in red. Interpretation modified from Blevin et al. (2005). Location of seismic line is shown in Fig. 5.

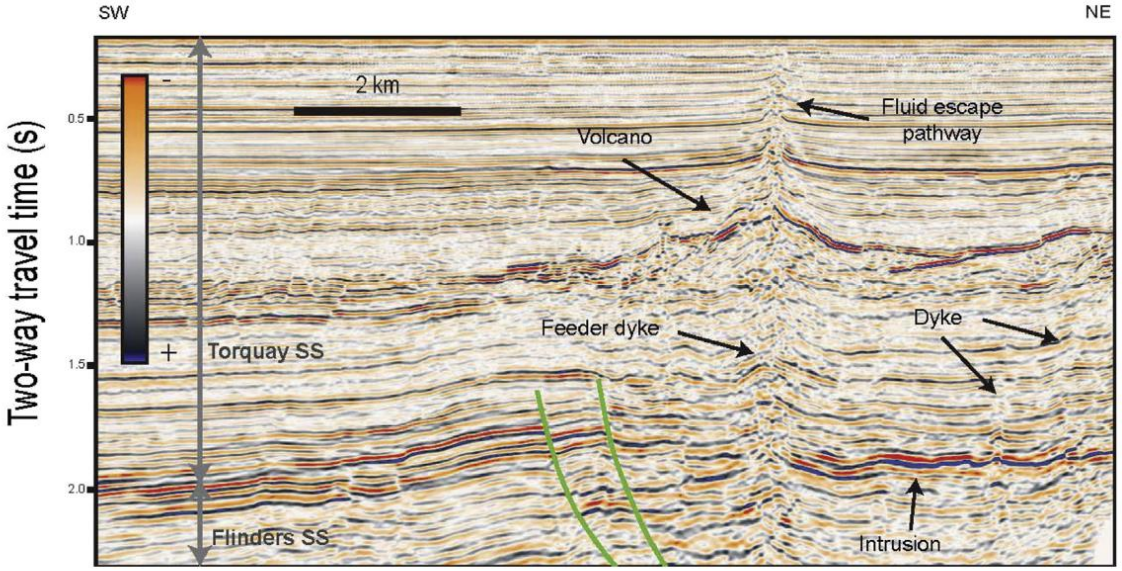

Fig. 19. Example of magmatic features in the Bass Basin near the Yolla Field. Location of seismic line from Yolla 3D survey (reverse SEG polarity) is shown in Fig. 5.

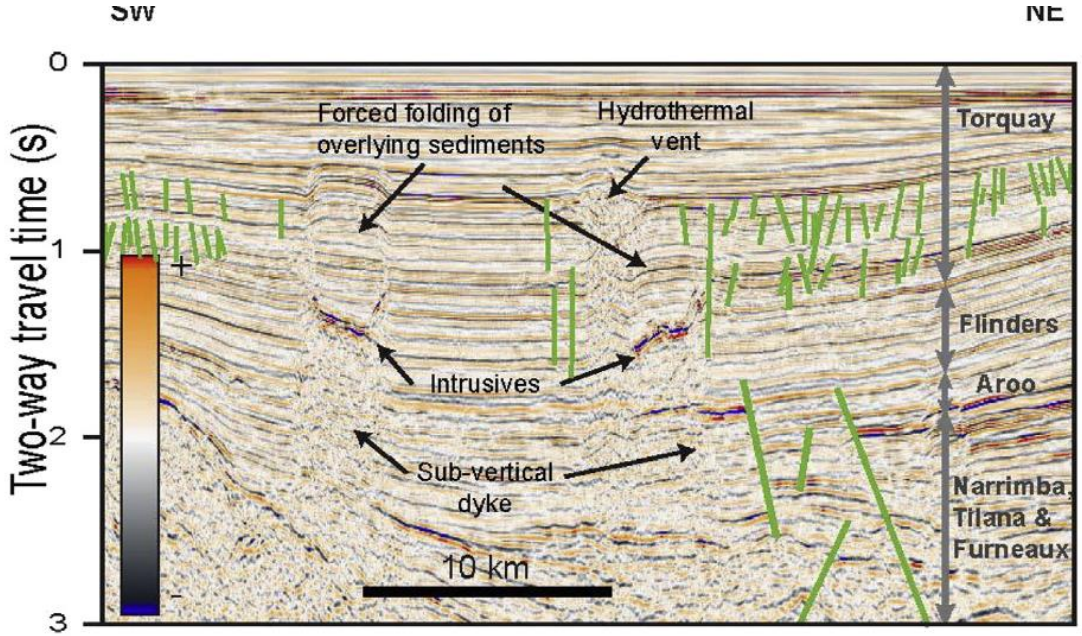

Fig. 18. Example of magmatic features in the Bass Basin, Cape Wickham Sub-basin, close-up from regional cross-section (seismic line 90-27, normal SEG polarity).

Please cite this article as: Mark, N.J., Schofield, N., Pugliese, S., Watson, D., Holford, S., Muirhead, D., Brown, R., Healy, D., Igneous intrusions in the Faroe Shetland basin and their implications for hydrocarbon exploration; new insights from well and seismic data, *Marine and Petroleum Geology* (2018), doi: 10.1016/j.marpetgeo.2017.12.005.

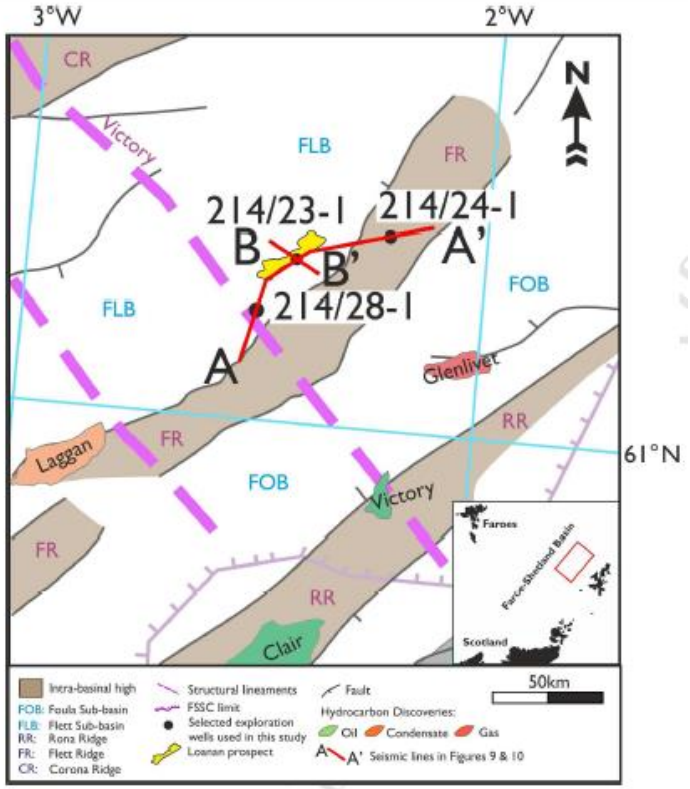

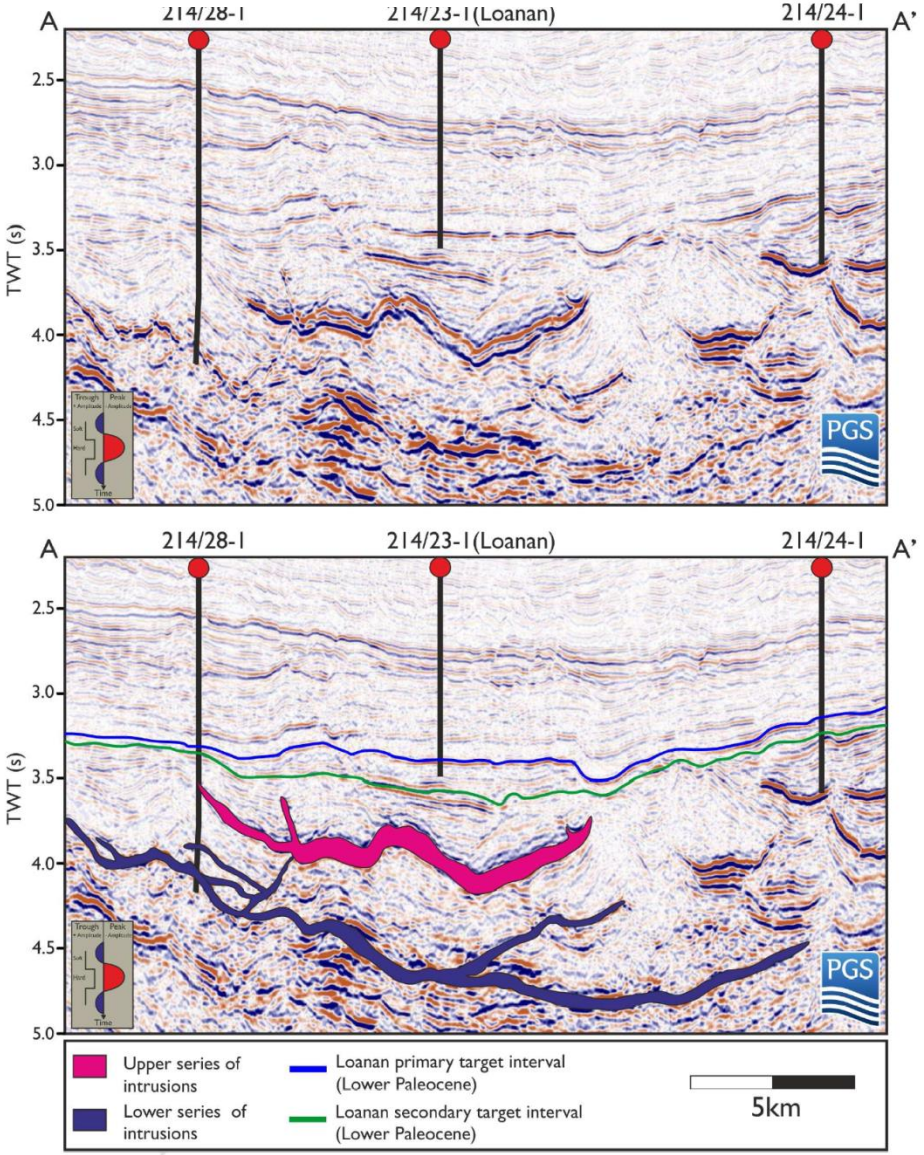

Figure 2: Seismic line from the FSB showing the typical seismic response of mafic intrusions. Mafic intrusions form prominent laterally discontinuous hard kicks. Seismic data courtesy of PGS (FSB MegaSurvey Plus).

Please cite this article as: Mark, N.J., Schofield, N., Pugliese, S., Watson, D., Holford, S., Muirhead, D., Brown, R., Healy, D., Igneous intrusions in the Faroe Shetland basin and their implications for hydrocarbon exploration; new insights from well and seismic data, *Marine and Petroleum Geology* (2018), doi: 10.1016/j.marpetgeo.2017.12.005.

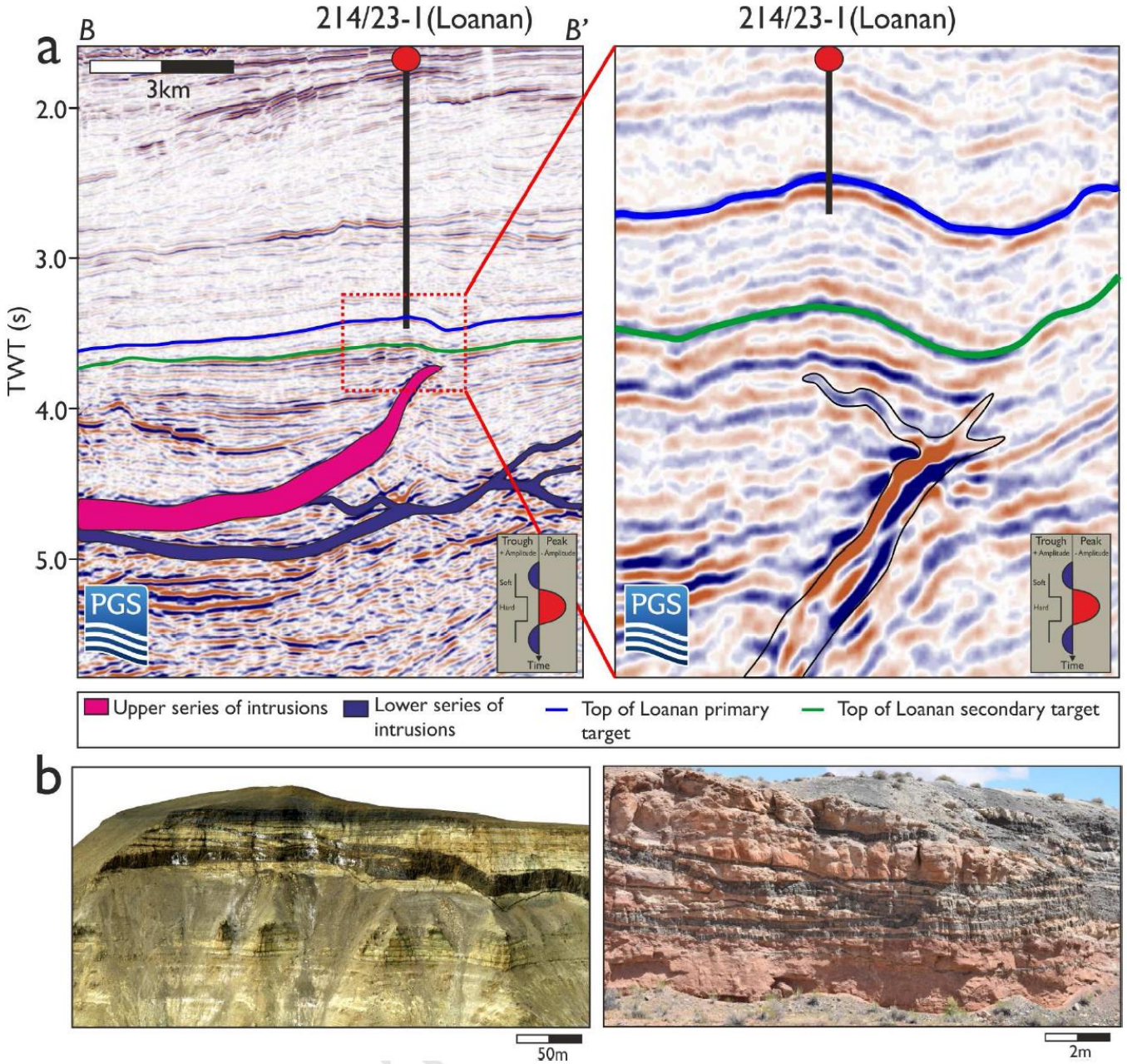

Please cite this article as: Mark, N.J., Schofield, N., Pugliese, S., Watson, D., Holford, S., Muirhead, D., Brown, R., Healy, D., Igneous intrusions in the Faroe Shetland basin and their implications for hydrocarbon exploration; new insights from well and seismic data, *Marine and Petroleum Geology* (2018), doi: 10.1016/j.marpetgeo.2017.12.005.

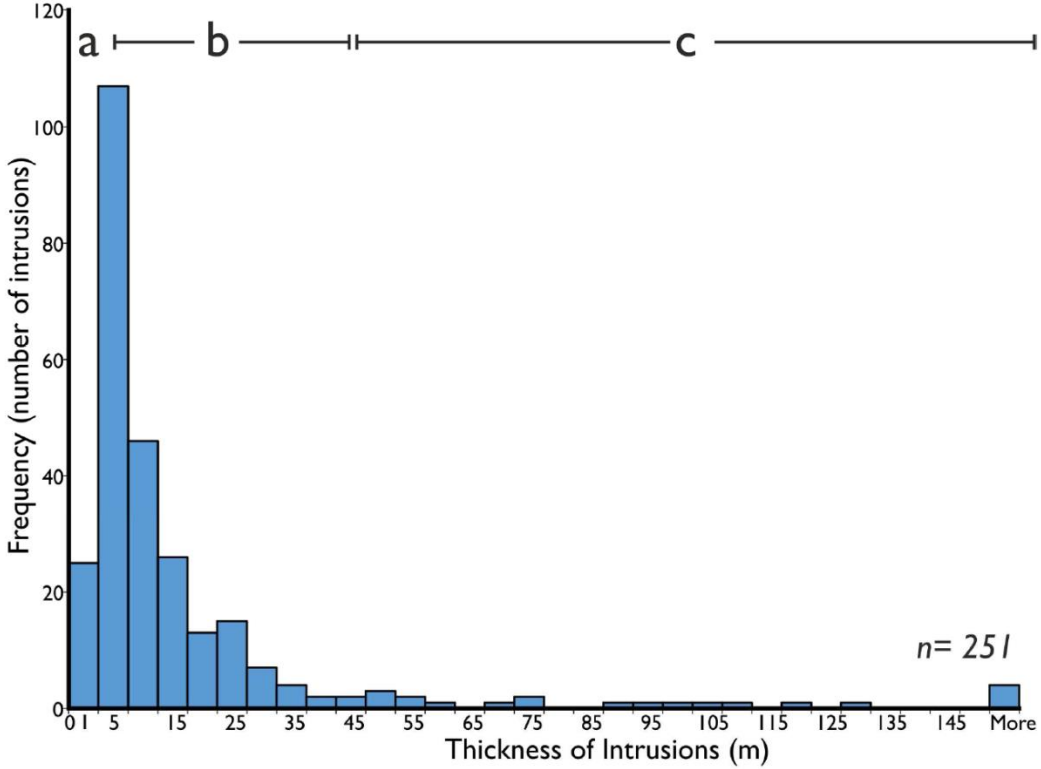

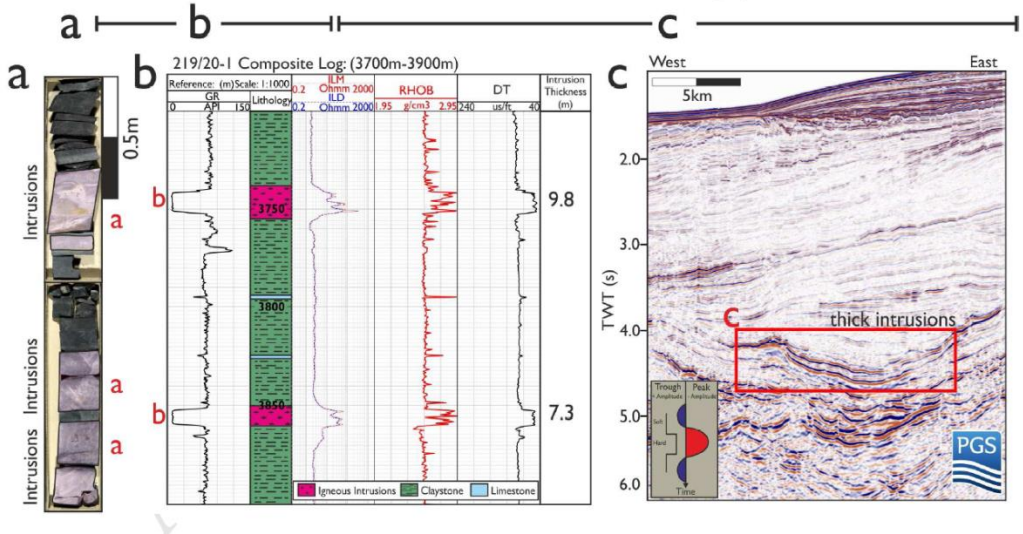

Please cite this article as: Mark, N.J., Schofield, N., Pugliese, S., Watson, D., Holford, S., Muirhead, D., Brown, R., Healy, D., Igneous intrusions in the Faroe Shetland basin and their implications for hydrocarbon exploration; new insights from well and seismic data, *Marine and Petroleum Geology* (2018), doi: 10.1016/j.marpetgeo.2017.12.005.

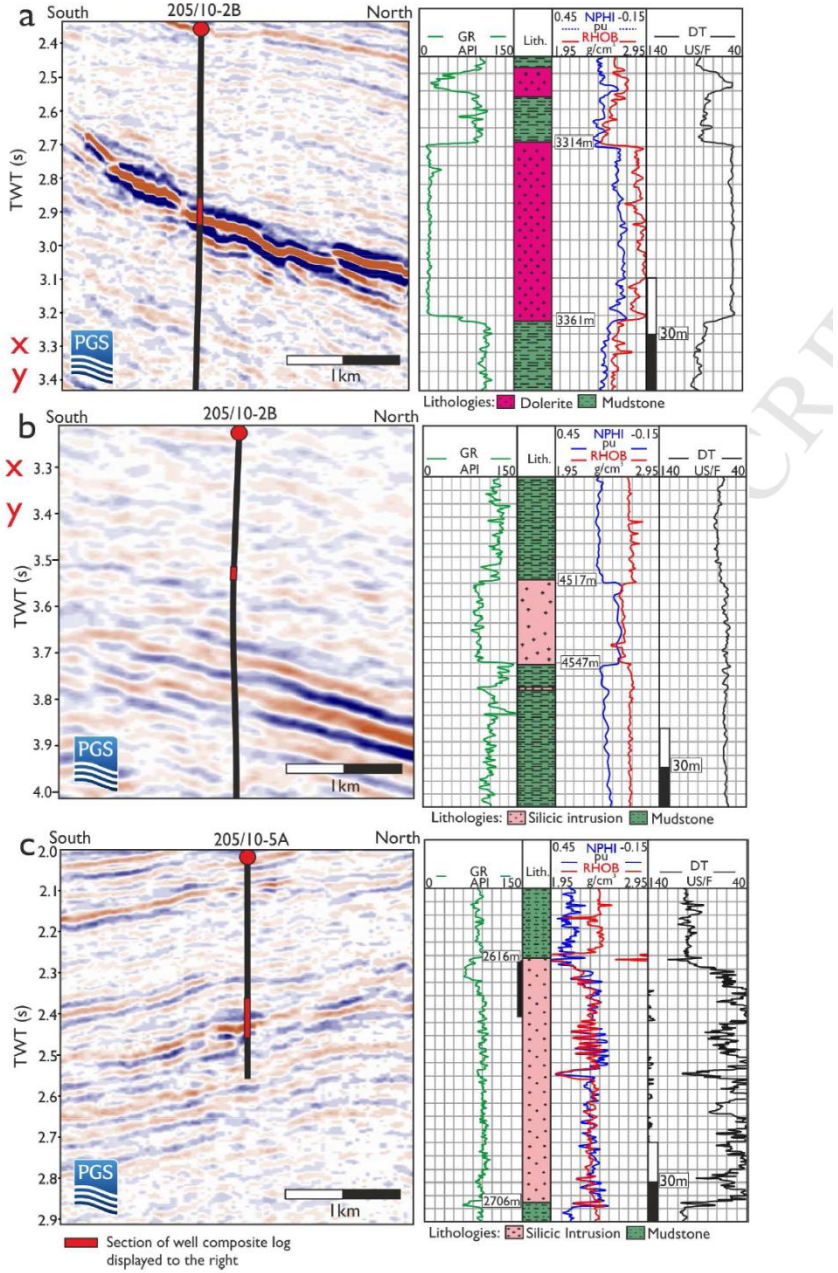

Моделирование интрузий

Разрезы через бассейн Кару с интрузиями силлов и даек

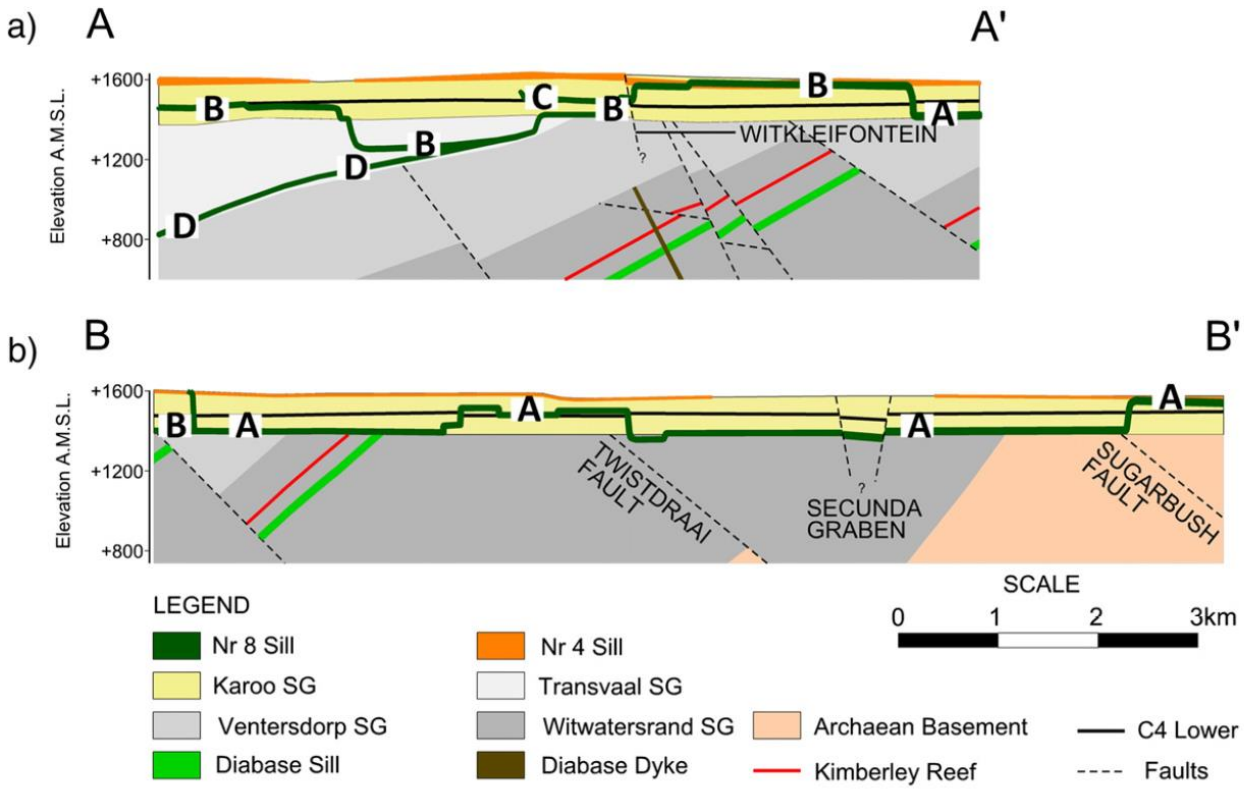

Fig. 6. Geological cross-sections along north-south section lines indicated on Figs. 4 and 6, with a vertical exaggeration factor of 2. a) Cross-section A–A′ showing the relationship of dolerites B–D in both the Karoo and basement stratigraphy. b) Cross-section B–B′ showing the occurrence of dolerite A mainly along the Dwyka–Ecca Group contact forming an isolated intrusive dome structure at its centre. Note that the Dwyka Ecca Group contact is obscured by the scale due to the low thickness of the Dwyka Group. The near vertical inclined sheet of dolerite A in the north forms the boundary (designated in Fig. 7) with dolerite B.

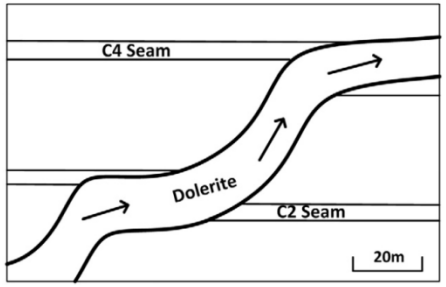

Fig. 9. Cross-sectional view (east-west) of the transgression of the south-western inclined sheet dolerite A consisting of steeper segments that cross-cut the strata alternating with flat, bedding-concordant segments that exploit and displace coal-seam horizons.

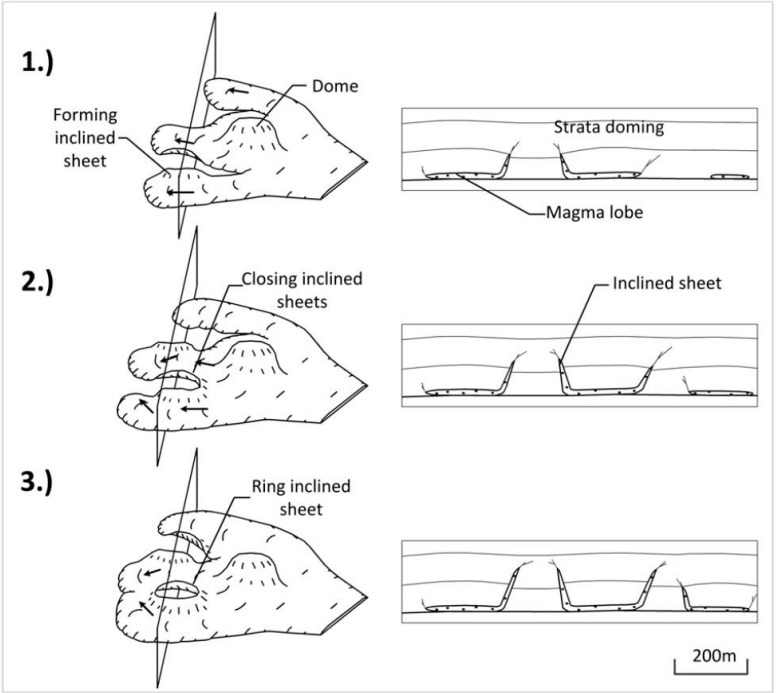

Fig. 13. Diagrammatic sketches illustrating the proposed stages in the development of domes along the inner sills of saucers, such as dolerite A. The arrows indicate magma movement during each stage (nr. 1–2). Cross-sectional views with the section lines are shown for each developmental stage with the magma propagation direction extending into the page. Refer to the text for more information.

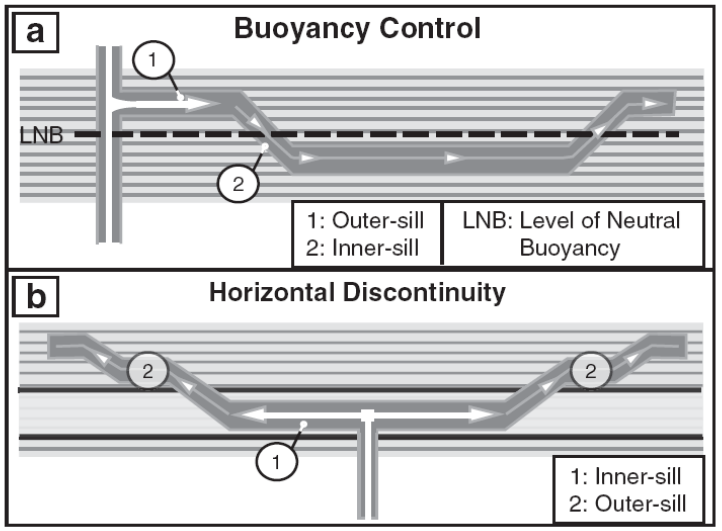

Fig. 1. Existing models of saucer-shaped sill emplacement mechanisms. Numbers (1) and (2) indicate the steps of emplacement. a. Model of emplacement controlled at the level of neutral buoyancy (LNB), Modified from Francis (Bradley, 1965; Francis, 1982 e.g., Barker, 2000). Sills are fed laterally from one part of the outer sills. b. Model of emplacement along horizontal discontinuity, modified after Malthe-Sørenssen et al. (2004). Sills are fed radially from the inner sill. See text for more information.

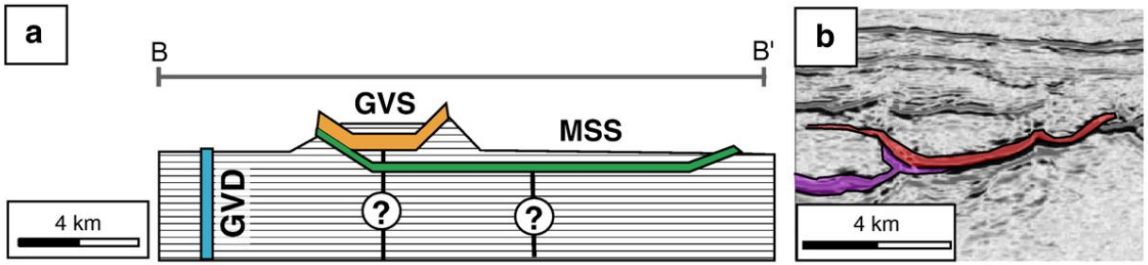

Fig. 8. a. Geological cross section of the southern part of the Golden Valley Sill and the underlying Morning Sun Sill (along B–B1 in Fig. 3). Although there is a physical contact between the two sills, their different geochemistry shows that the MSS was not the feeder of the GVS. b. Example of seismic image showing contact between two saucer-shaped sills, interpreted as feeding relationship (modified after Hansen et al., 2004). The comparison between this image and the geological cross section of the GVSC show remarkable similarities. Because our study shows that contacts between sills are not obviously feeding relationships, we propose another interpretation where each sill (highlighted in red and purple) may represent a distinct batch of magma. Thus, in order to infer the nature of these contacts on seismic images, more criteria are needed.

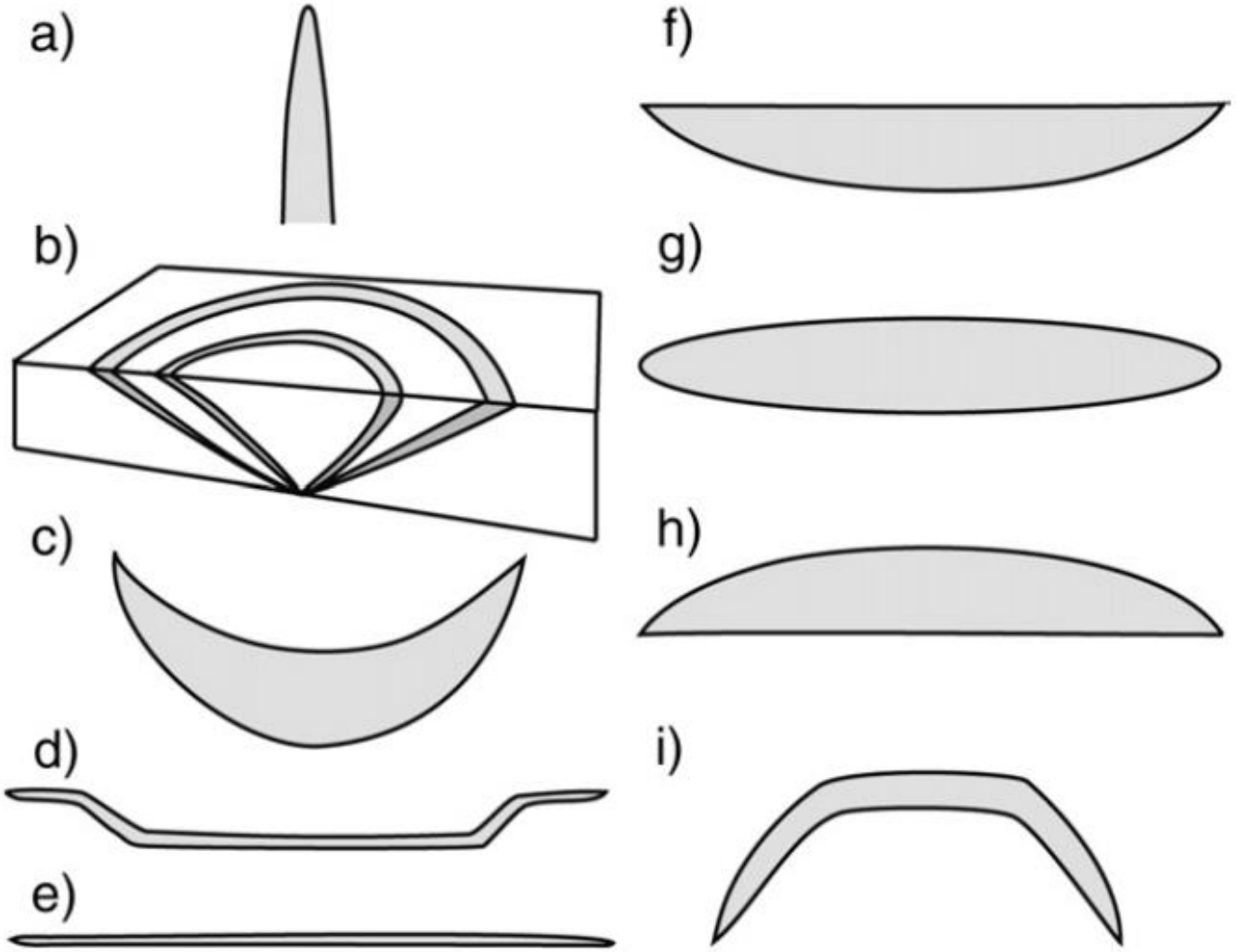

Fig. 1. The shape classification of magmatic intrusions: (a) dyke (b) cone-sheet (c) cup-shaped intrusion (d) saucer-shaped intrusion (e) sill (f) lopolith (g) pluton (h) laccolith (i) ring dyke.

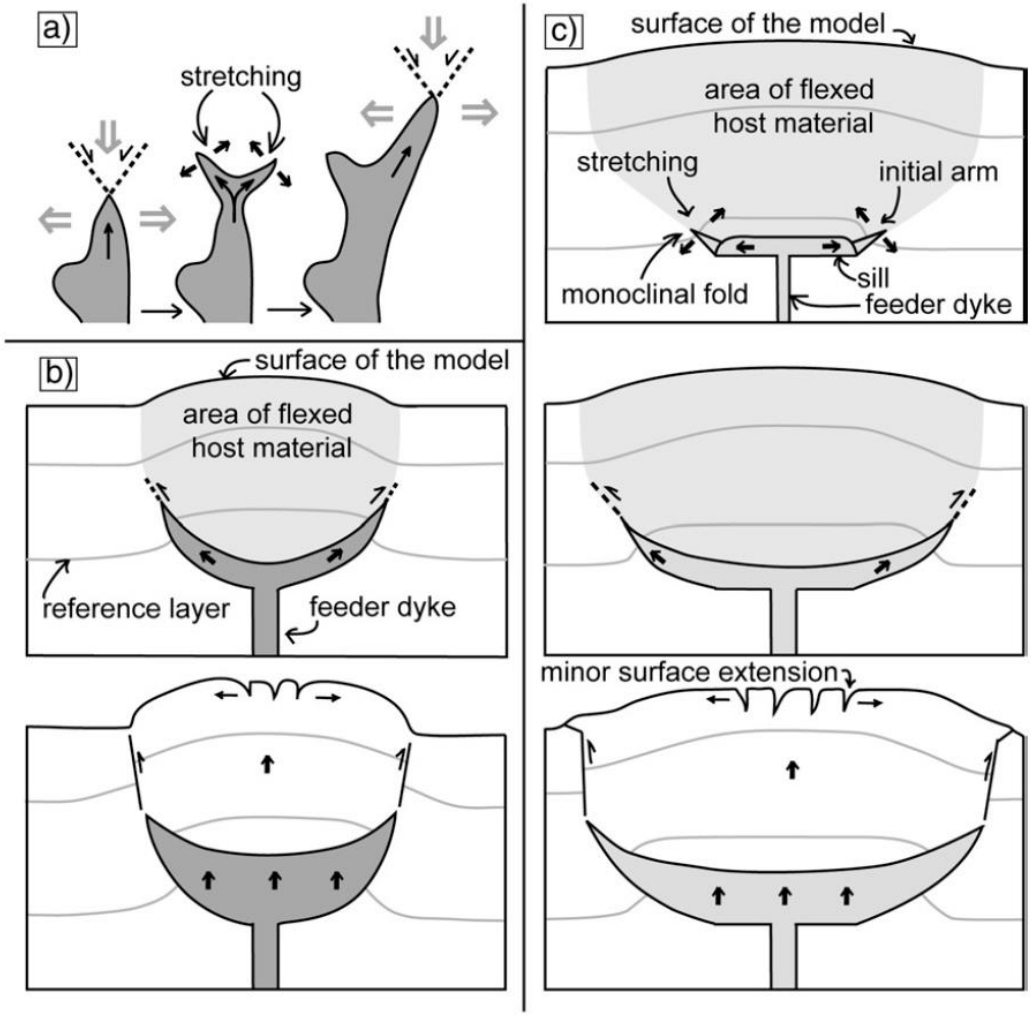

Fig. 7. Mechanisms for intrusion propagation and cup-shaped intrusion growth: (a) dyke propagates by infiltrating normal faults by repetitive branching, (b) for low viscosity intrusive liquids, a small inverted cone-like structure forms initially. Then a inverted a cup-shaped structure develops, forming a dome at the surface of the model. Ultimately, the central thickness of the intrusion increases and thrusts form above of the cup-shaped intrusion, (c) for high viscosity intrusive liquids, a sill forms, this folds the surrounding rock. The intrusion then grows up shear faults created at the fold hinge.

Влияние интрузий на термальную историю осадочного бассейна

Please cite this article as: Sydnes, M., Fjeldskaar, W., Løtveit, I.F., Grunnaleite, I., Cardozo, N., The importance of sill thickness and timing of sill emplacement on hydrocarbon maturation, *Marine and Petroleum Geology* (2017), doi: 10.1016/j.marpetgeo.2017.10.017.

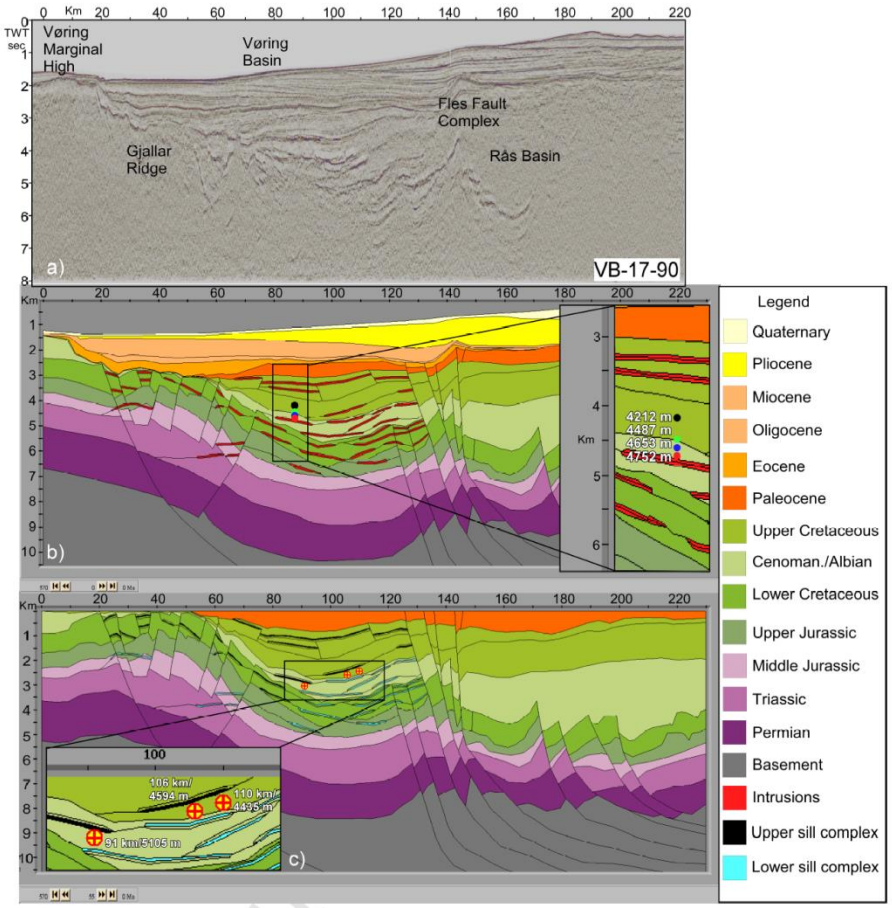

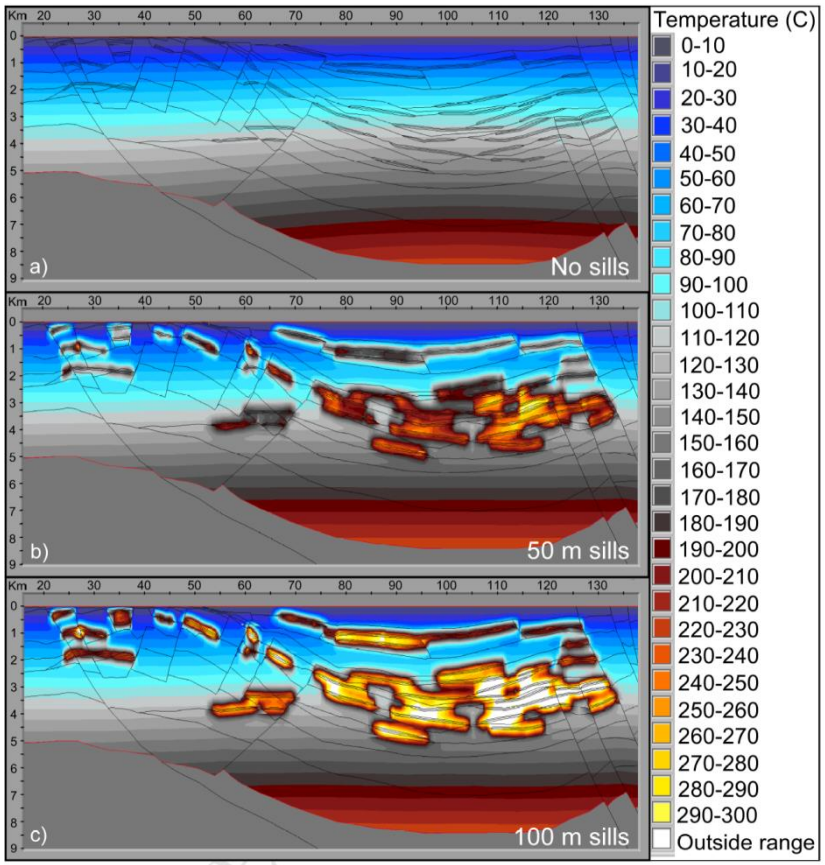

Fig. 6: Temperature and transformation ratio for the four points in the central part of the basin shown in Fig. 3b. The first column corresponds to the scenario with no sills, second column to 50 m sills, and third column to 100 m sills. In all plots the four lines correspond to the four points and have increasing depth (black, green, blue, red) and decreasing distance to intruded sill. Intrusion temperature is 1000 °C.

Дайковые пояса района Вилюйского бассейна (для сравнения)

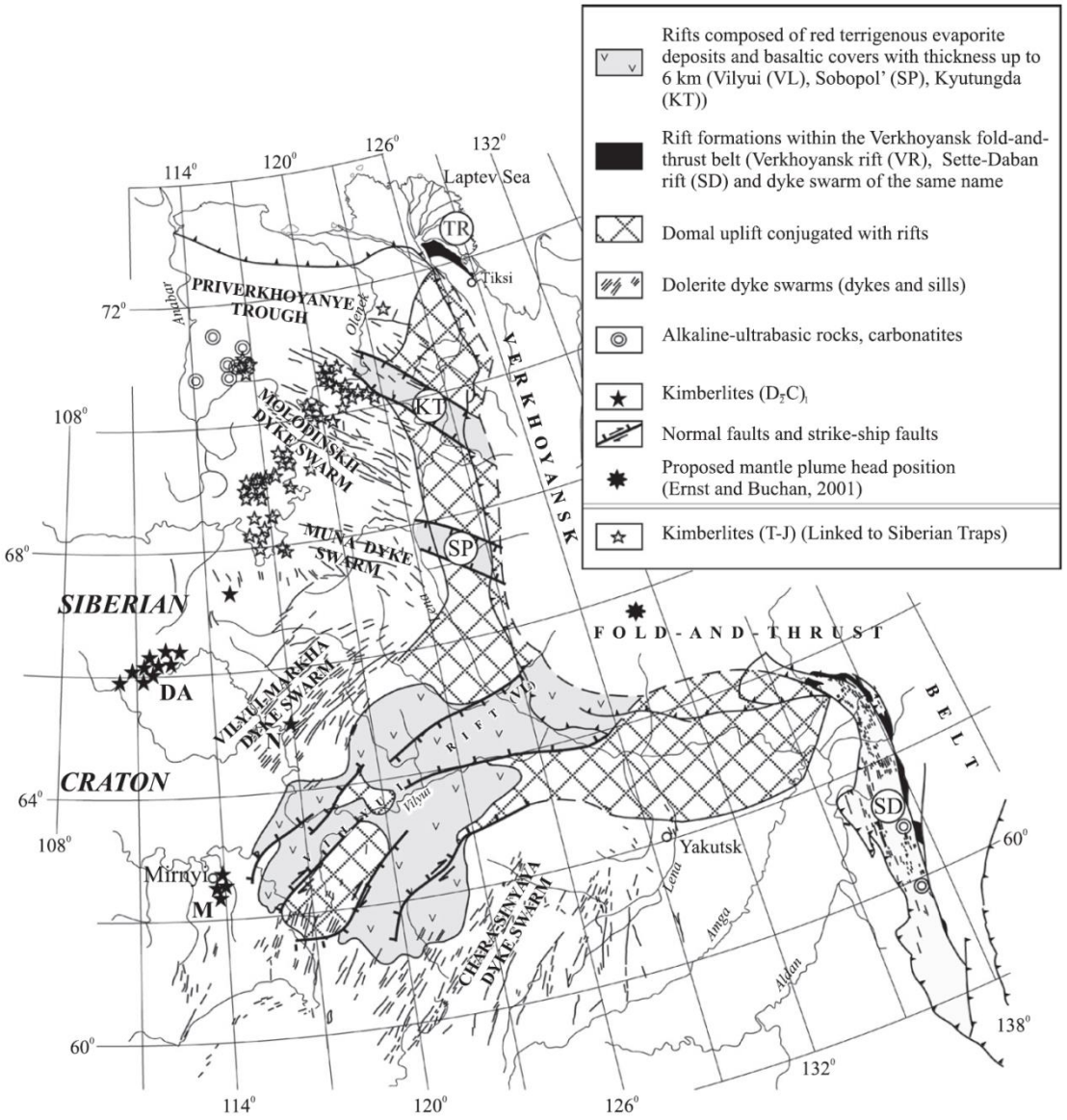

Fig. 1. The Middle Paleozoic basic dyke swarms, kimberlite fields and rifts in the eastern part of the Siberian Craton (modified from Parfenov and Kuz'min, 2001). Middle Paleozoic kimberlite fields: M = Mirnyi, N = Nakyn, DA = Daldyn-Alakit. Kempendyai (K) and Ygiatta (Y) basins are separated by Suntar uplift.

Дайковые пояса Патомского района Восточной Сибири (для сравнения)

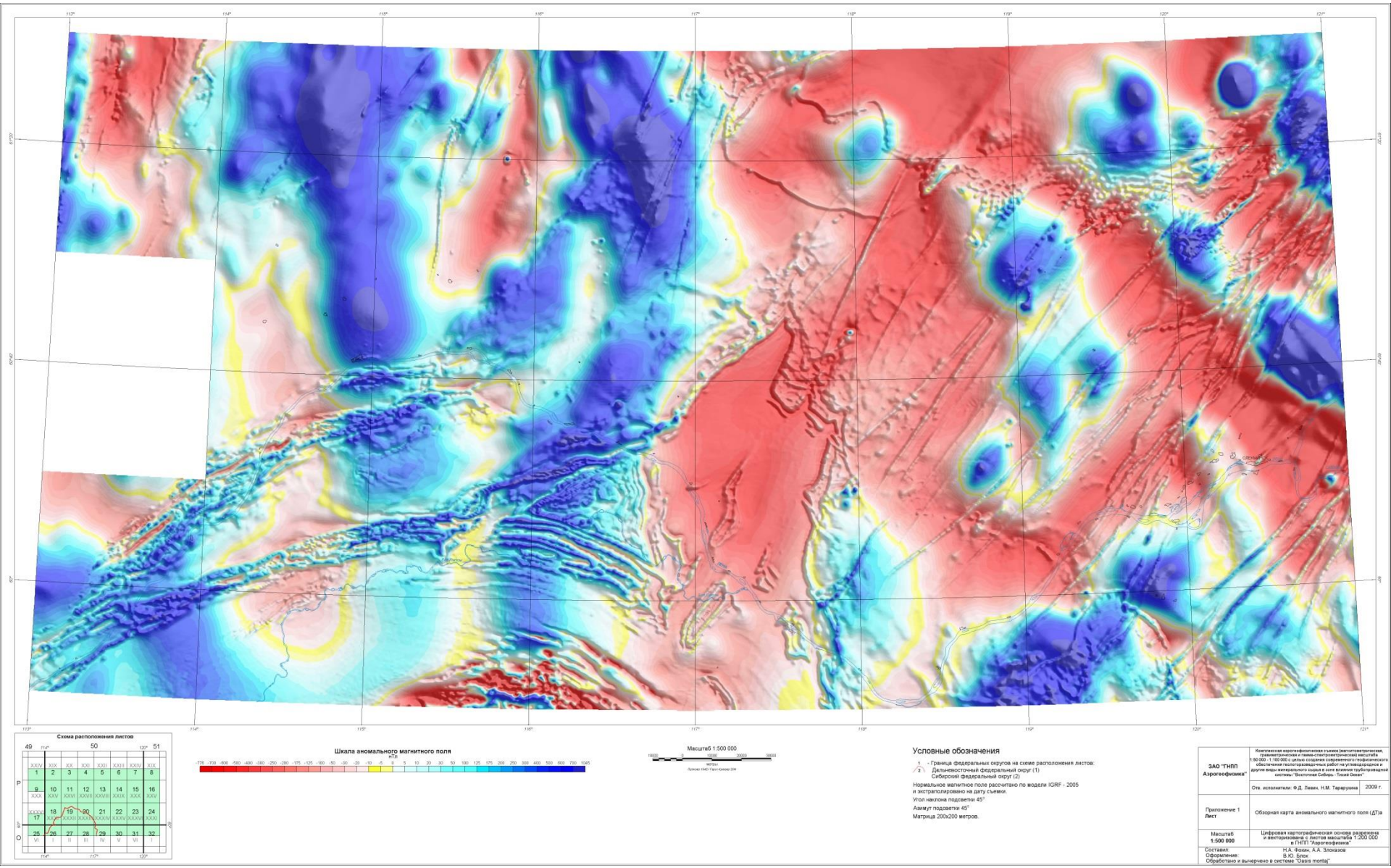

Схематическая модель магматизма на границе баррема и апта.
Магматизму предшествовала фаза малоамплитудного воздымания